NUMERICAL MODELLING OF NANOPARTICLE DIFFUSION AND MICROSTRUCTURE FORMATION DURING SELECTIVE LASER MELTING PROCESS

by

Taosif Alam

A thesis submitted in partial fulfillment
of the requirements for the degree

of

Master of Science

in

Mechanical Engineering

MONTANA STATE UNIVERSITY
Bozeman, Montana

May 2022

©COPYRIGHT

by

Taosif Alam

2022

All Rights Reserved

ACKNOWLEDGEMENTS

I would like to express my deepest gratitude to Dr. M. Ruhul Amin for his constant guidance and support throughout this research and thesis work. It was Dr. Amin's high spirit, patience, and thoughtful advice that kept me motivated and determined during difficult times in the course of my graduate study. I am very fortunate to be able to closely learn from a professor who has great love, devotion, and a keen eye in the fields of academia and engineering.

I would also like to acknowledge Dr. Erick Johnson and Dr. Yaofa Li for their excellent support as committee members. I would like to thank them for their valuable time and feedback on this research work. I am grateful to the Department of Mechanical and Industrial Engineering for providing me with the financial support and resources that helped me to pursue my dream. My appreciation goes to all the course instructors that I have worked with and the staff of the Department of Mechanical and Industrial Engineering, and my fellow graduate students for their continued support.

My wholehearted gratitude goes to my wife, who has constantly supported me during my long-distance stay in pursuing my degree. I truly appreciate your company, patience, and guidance that motivated me to better myself in my graduate and personal life. My parents and my brother were always my biggest inspiration for whom I was able to reach this far, and I will always be grateful for them. My special thanks go to Razin Sazzad for his motivation, thoughtful discussions, and helping hand throughout my graduate life. Finally, my heartfelt gratitude to all my friends in Bozeman and different parts of the world who have helped me through thick and thin.

TABLE OF CONTENTS

1. INTRODUCTION 1

Motivation 3
Literature Review 4

2. PROBLEM FORMULATION 18

Concept 18
CFD modeling of the SLM process 21
Assumptions 21
Governing Equations 22
Conservation of Mass 22
Conservation of Momentum 22
Energy Equation 23
Initial and Boundary Conditions 23
Thermophysical Properties of Material 25
Marangoni Convection and Natural Convection 28
Enthalpy Porosity Technique 30
Euler Lagrangian Approach 32
Particle Motion Equations 32
Equation of Force Balance 32
Drag Force 33
Virtual Mass and Pressure Gradient Force 34
Saffman's Lift Force 35
Brownian Motion 35
Solidification Morphology of Melt Pool 36
Nucleation and Grain Growth in SLM 37

3. NUMERICAL METHOD OF CFD MODEL 40

Introduction 40
Discretization 42
Discretization of Transient Terms 42
Discretization of Advection and Diffusion Terms 42
Discretization of Continuity and Momentum Equations 44
Pressure Based Segregated Algorithm 46
Grid Independence Test 49
Code Validation 52
Validation of the Melt Pool Geometry 52
Validation of Particle Tracking Model 57

TABLE OF CONTENTS CONTINUED

4. CELLULAR AUTOMATA SOLIDIFICATION MODEL....58

Introduction....58
Cell Transition Rules....59
Nucleation Modeling....61
Grain Growth Modeling....62
Cell Capture Mechanism....67
Coupling with CFD Model....69
Simulation Parameters....73
Validation of Cellular Automata Model....75
Validation of Competitive Grain Growth Algorithm....76
Validation of Average Grain Size....77

5. RESULTS AND DISCUSSIONS....82

Introduction....82
Modeling of Process Parameters....83
Computational Matrix....85
Temperature Characteristics in Selective Laser Melting....88
Velocity Distribution in Molten Pool....95
Nanoparticle Distribution at Transverse Planes....102
Solidification Parameters and Microstructure Evolution in Transverse Plane....113
Calculation of solidification parameters....114
Microstructure evolution by the Cellular Automata model....116
Effect of Laser Scan speed....126
Temperature and Velocity Distribution....126
Nanoparticle Distribution at Transverse plane....131
Microstructure evolution....135
Effect of Laser Power....142
Temperature and Velocity Distribution....142
Nanoparticle Distribution at Transverse plane....146
Microstructure evolution....148
Effect of Preheating temperature....153
Temperature and Velocity Distribution....153
Nanoparticle Distribution at Transverse plane....157
Microstructure evolution....159

6. CONCLUSION AND RECOMMENDATIONS....163

REFERENCES CITED....170

LIST OF TABLES

Table Page

2.1. Thermophysical properties of AlSi10Mg 27

2.2. Thermophysical properties of TiB2 28

4.1. Transition rules for melting and solidification....60

4.2 Gaussian distribution parameter for AlSi10Mg....62

4.3 Grain size measurement by linear intercept method and comparison of average grain diameter at a cross-section with experimental data....81

5.1. Process parameters used in the present numerical model....85

5.2. Computational matrix for the study of process parameters 85

5.3 Molten pool dimensions....93

5.4. Average grain diameter comparison for 150 W laser power, 500 mm/s scanning speed, preheated at 100°C....123

5.5. Average grain diameter comparison for varying laser scan speed 141

5.6. Average grain diameter comparison for varying laser power....152

5.7. Average grain diameter comparison for varying preheating temperatures....162

LIST OF FIGURES

Figure Page

1.1. Typical selective laser melting process....2

2.1. Schematic illustration of the CFD computational domain....19

2.2. Schematic diagram of Marangoni convection creating a radial outward flow from the center of the molten pool 28

2.3. Effect of thermal gradient (G) and solidification rate (R) on solidification morphology....36

2.4. Illustration of various solidification phenomena, i.e., epitaxial growth, competitive growth, and nucleation....37

2.5. Grain formed for a cubic metal in non-uniform temperature conditions....38

3.1. Illustration of control volume discretizing....41

3.2. Schematic of control volume discretization for quadrilateral or hexahedral meshes....43

3.3. Overview of the pressure-based segregated algorithm....48

3.4. Grid independence test of the numerical model....50

3.5. Computational mesh at: (a) entire domain, (b) transverse plane at x = 650 μm....51

3.6. Illustration of forming melted zone at transverse (y-z) plane at x = 650 μm for 180W laser power and 300 mm/s scanning speed: (a) Maximum temperature profile (b) Final melted zone 54

3.7. Comparison of the geometry of the molten substrate with published experimental data [4] for 180 W laser power and 300 mm/s laser scanning speed....55

3.8. Comparison of numerical and experimental results [4]: (a) for varying laser power from 100 W to 195 W at a laser scan speed of 300 mm/s, (b) for varying laser scan speed keeping laser power constant at 180 W 56

3.9. Comparison of numerically obtained particle distribution results: (a1) showing numerical results from Bagheri et al. [74] and (a2) showing results from the current numerical model....57

LIST OF FIGURES CONTINUED

Figure Page

4.1. Schematic representation of a 2D CA domain with Moore neighborhood.....59

4.2. Schematic illustration of the modified decentered square and modified decentered polygon algorithm 64

4.3. Schematic illustration of dendritic growth of a cubic metal represented in 2D CA domain.....65

4.4. Schematic diagram of grain capture method by modified decentered polygon method.....68

4.5. Schematic illustration of CA computational domain and its relation with the transverse plane of the CFD simulation domain.....71

4.6. Diagram showing the workflow of CA grain growth model coupled with a CFD model 72

4.7. Initial grain structure for CA grain growth model.....75

4.8. Comparison of competitive grain growth algorithm between (a1) numerical results computed by Rai et al. [82] and (a2) results from the current CA model.....77

4.9. Comparison of microstructures for the solidified layer of 316 Stainless steel at a cross-section between (a) results from the present Cellular Automata grain growth model and (b) experimental results published by Baumard et al. [83] 78

4.10. Grain size measurement by intercept length method for (a) 0° orientation, (b) 90° orientation, (c) 45° orientation, (d) 135° orientation for the predicted microstructure by the current CA model 80

5.1. Initial distribution of the nanoparticles; (a) in entire domain, (b) at a transverse (y-z) plane at x = 550 μm 87

5.2. Temperature distribution at time 1050 μs, during selective laser melting at 150 W laser power and 500 mm/s scanning speed with 100° C preheated temperature: (a) full isometric view of the computational domain, (b) zoomed view of the selected box.....89

LIST OF FIGURES CONTINUED

Figure Page

5.3. Difference in thermal conductivity in the powder bed, molten pool, and substrate region during selective laser melting: (a) full isometric view of the computational domain, (b) zoomed view of the selected box 90

5.4. Temperature and thermal gradient distribution at time 1050 μs during selective laser melting at 150 W laser power, 500 mm/s scanning speed, and 100° C preheated temperature: (a) full isometric view of the computational domain, (b) zoomed view of the selected box 91

5.5. Melt pool dimensions in (a) symmetric plane (b) transverse plane 93

5.6. Temperature histories of the maximum temperature and representative points P1 and P2; (a) temperature history plot, (b) Coordinates of points P1 and P2 94

5.7. Temperature distribution due to moving laser for 150 W, 500 mms/s scanning speed at (a) time 100 μs, (b) 600 μs, (c) 1050 μs, (d) 1600 μs 95

5.8. Temperature and velocity distribution for at time 1050 μs during selective laser melting for 150 W laser moving at 500 mm/s scanning speed, and 100° C preheated temperature: (a) full isometric view of the computational domain, (b) zoomed view of the selected box 96

5.9. Selected x-y planes from the isometric view 98

5.10. Temperature and the tangential velocity field at the selected x-y planes depicted in Fig. 5.9: (a1,b1, and c1) full view of the selected planes, (a2,b2, and c2) zoomed view of the selected boxes. 99

5.11. Selected y-z planes along the melt pool from the isometric view 100

5.12. Temperature and the tangential velocity field at the selected y-z planes depicted in Fig. 5.11: (a1-a2) Transverse plane at 650 μm, (b1-b2) Transverse plane at 575 μm, and (c1-c2) Transverse plane at 500 μm.....101

5.13. Dynamics of nanoparticle transport at a 2D transverse plane: (a1-a12) temperature and velocity in the whole computational domain, (b1-b12) 3D velocity field acting on the transverse plane, (c1-c12) nanoparticle distribution in the transverse plane with the 2D tangential velocity vector of the flow field 103

5.14. Final nanoparticle distribution in the transverse planes: (a1-a2) x = 650 μm, (b1-b2) x = 550 μm for 150 W laser power moving at 500 mm/s scanning speed.....113

LIST OF FIGURES CONTINUED

Figure Page

5.15. (a) Plot of the thermal gradient and cooling rate along the respective probing points of the molten pool at a transverse plane, and (b) representative data probing points from the front view of the transverse plane 116

5.16. Simulation of melting process by the current Cellular Automata model: (a) initial microstructure, (b) melting of microstructures at1000 μs, and (c) melting of microstructures at 1100 μs 118

5.17. Microstructure evolution by 2D Cellular automata model at specific time steps: (a1-a4) without considering nanoparticles, (b1-b4) considering nanoparticles in the CA domain.....120

5.18. Microstructures simulated by the current CA model at two different planes: (a1-a2) simulated microstructures at transverse plane x = 550 μm and (b1-b2) simulated microstructures at transverse plane x = 650 μm 125

5.19. Variation of temperature histories of the maximum temperature and representative P1 and P2 points on the top surface: (a) 300 mm/s laser scanning speed, (b) 400 mm/s laser scanning speed, (c) 500 mm/s laser scanning speed, (d) 600 mm/s laser scanning speed, (e) location of representative points P1 and P2 126

5.20. Temperature and velocity distribution due to variation of laser scanning speed: (a) 300 mm/s laser scanning speed, (b) 400 mm/s laser scanning speed, (c) 500 mm/s laser scanning speed, (d) 600 mm/s laser scanning speed 128

5.21. Variation of Marangoni number with the change of laser scanning speed.....130

5.22. Variation of molten pool dimensions with the change of laser scanning speed 131

5.23. Final nanoparticle distribution in solidified region due variation of laser scanning speed: (a1-a2) 300 mm/s laser scanning speed, (b1-b2) 400 mm/s laser scanning speed, (c1-c2) 500 mm/s laser scanning speed, (d1-d2) 600 mm/s laser scanning speed 134

5.24. Variation of simulated microstructure without considering final nanoparticle distribution with the change in laser scanning speed: (a) laser scanning speed 300 mm/s, (b) laser scanning speed 400 mm/s, (c) laser scanning speed 500 mm/s, (d) laser scanning speed 600 mm/s.....138

LIST OF FIGURES CONTINUED

Figure Page

5.25. Variation of simulated microstructure considering final nanoparticle distribution with the change in laser scanning speed: (a) laser scanning speed 300 mm/s, (b) laser scanning speed 400 mm/s, (c) laser scanning speed 500 mm/s, (d) laser scanning speed 600 mm/s 140

5.26. Variation of temperature histories of the maximum temperature and representative P1 and P2 points on the top surface: (a) laser power of 125 W, (b) laser power of 150 W, (c) laser power of 175 W, (d) laser power of 200 W and (e) representative points P1 and P2.....143

5.27. Temperature and velocity distribution due to variation of laser power: (a) laser power of 125 W, (b) laser power of 150 W, (c) laser power of 175 W, and (d) laser power of 200 W 144

5.28. Variation of Marangoni number with the change of laser power 145

5.29. Variation of molten pool dimensions with the change in laser power.....146

5.30. Final nanoparticle distribution in solidified region due to variation of laser power: (a1-a2) laser power of 125W, (b1-b2) laser power of 150W: (c1-c2) laser power of 175 W, (d1-d2) laser power of 200W 147

5.31. Variation of simulated microstructures without considering final nanoparticle distribution with change in laser power: (a) laser power of 125W, (b) laser power of 150W, (c) laser power of 175 W, (d) laser power of 200W 149

5.32. Variation of simulated microstructures considering final nanoparticle distribution with change in laser power: (a) laser power of 125W, (b) laser power of 150W, (c) laser power of 175 W, (d) laser power of 200W.....151

5.33. Variation of temperature histories of the maximum temperature and representative P1 and P2 points on the top surface: (a) preheating temperature of 300 K, (b) preheating temperature of 373 K, (c) preheating temperature of 473 K, (d) representative points P1 and P2 153

5.34. Temperature and velocity distribution at time 1050 μs due to variation of preheating temperature: (a1-a2) preheating temperature of 300 K, (b1-b2) preheating temperature of 373 K, (c1-c2) preheating temperature of 473 K 155

5.35. Variation of molten pool dimensions due to change in preheating temperature 156

LIST OF FIGURES CONTINUED

Figure Page

5.36. Variation in Marangoni number due to change in preheating temperature 156

5.37. Final nanoparticle distribution in the solidified region due to variation of preheating temperature: (a1-a2) 300 K preheating temperature, (b1-b2) 373 K preheating temperature, and (c1-c2) 473 K preheating temperature 158

5.38. Variation of simulated microstructure without considering nanoparticles due to change in preheating temperature: (a) 300 K preheating temperature, (b) 373 K preheating temperature and (c) 473 K preheating temperature 160

5.39. Variation of simulated microstructure considering nanoparticles with the change in preheating temperature: (a) 300 K preheating temperature, (b) 373 K preheating temperature and (c) 473 K preheating temperature 161

NOMENCLATURE

Symbol	Description
A	Area
a	Linearized coefficient of the scalar quantity
A_{mushy}	Mushy zone constant
b	Net flow rate into the cell
C	Cell center
C_c	Cunningham slip correction
C_P	Specific heat capacity
D_p	Diameter of the powder
d_p	Diameter of the nanoparticle
F	Force
f	Face centroid
F_B	Brownian force
F_D	Drag force
F_P	Pressure gradient force
F_S	Saffman's lift force
F_V	Virtual mass force
F_{view}	Internal radiation factor
G	Temperature gradient

NOMENCLATURE CONTINUED

g	Gravitational constant
h_c	Convection heat transfer coefficient
h_s	Sensible enthalpy
H_E	Enthalpy of the metal
I	Identity matrix
J_f	Mass flux rate
J_v	Evaporated mass
k	Thermal conductivity
k_B	Boltzmann constant
k_r	Thermal conductivity due to internal radiation
L	Length of the half diagonal
L_H	Latent heat of fusion
L_V	Latent heat of vaporization
M	Molecular mass of the metal
m	Atomic mass of the metal
m_p	Mass of the nanoparticle
Ma	Marangoni Number
N	Nucleation density
N_{max}	Maximum nucleation density

NOMENCLATURE CONTINUED

n	Number of time step
O	Orientation variable
P	Laser power
p	Pressure of the fluid
P_a	Ambient pressure
P_v	Vaporization pressure
Q_v	Vaporization heat loss
q	Heat source
R	Solidification rate
r	Position vector
R_g	Universal gas constant Position vector
r_b	Diameter of the laser heat source
S	State variable of the cell
S_0	Spectral intensity of the Brownian force
S_L	Optical penetration depth of the laser
S_ϕ	Source term
T	Temperature
T_L	Liquidus temperature
T_S	Solidus temperature
t	time
T_0	Initial Temperature

NOMENCLATURE CONTINUED

T_∞	Ambient temperature
T_b	Boiling temperature
$\dot{T}$	Cooling rate
u	Fluid velocity
u_p	Velocity of the nanoparticle
u_x	Velocity component in x-direction
u_z	Velocity component in z-direction
V	Control volume
v	Grain growth velocity
V_L	Laser scanning speed
v_s	Solidification front velocity
w	Width of the molten pool
x,y,z	Spatial coordinates

Greek symbol

α	Heat absorptivity
α_t	Thermal diffusivity
β	Coefficient of thermal expansion
β_L	Liquid fraction
β_r	Resistivity of the metals
Γ_ϕ	Coefficient of diffusion

NOMENCLATURE CONTINUED

Δ	Mathematical operator for difference
δ	Powder bed thickness
δ_k	Anisotropic coefficient
ε	Emissivity
ζ_i	Independent Gaussian random number
θ	Grain orientation angle
θ_t	Angle between the thermal gradient and y-axis
λ	Wavelength of the laser source
λ_f	Mean free path of the fluid
μ	Dynamic viscosity
ν	Kinematic viscosity
ρ	Density
σ	Surface tension of the fluid
σ_S	Stefan-Boltzmann constant
τ	Stress
$\emptyset$	Porosity of the powder bed
ϕ	Scalar quantity

NOMENCLATURE CONTINUED

Subscripts and Superscripts

*	Guessed value in the cell
′	Corrected value in the cell
i	Cell index
j	Index of the half diagonal
C	Cell value
f	Unit face of the control volume
m	Metal state
n	Normal of the vector quantity
nb	Neigbouring cell
np	Nanoparticle
p	Powder state
ref	Reference value
x	Component of the vector in x-direction
y	Component of the vector in y-direction
z	Component of the vector in z-direction

ABSTRACT

Selective laser melting (SLM) is a popular metal additive manufacturing technique that has a wide range of industrial applications lately. This additive process allows the development of new metal matrix nanocomposites by fusing metallic powders with nanoparticles. However, the molten pool flow generated by a moving laser heat source has complex fluid dynamics which redistribute the nanoparticles. Consequently, the microstructures of the solidified molten pool are affected by the local distribution of nanoparticles, which is reflected in their mechanical properties. Smaller grains can increase the strength and isotropic behavior of the solid layers. Therefore, the current research aims to numerically investigate the relationships among the SLM process parameters, nanoparticle transport, and microstructure evolution to explore the formation of nanocomposites.

The current study formulated a three-dimensional computational fluid dynamics (CFD) model of the SLM process in a commercial software package, ANSYS FLUENT. A volumetric laser heat source model melted the aluminum alloy powders and the underlying solid substrate. The difference between the powder and the solid or liquid state of the metal alloy was defined using an effective thermal conductivity model. Lagrangian particle transport calculation was performed to track TiB_2 nanoparticles in the molten pool. This model was coupled with a 2D Cellular Automata (CA) model to simulate the solidified microstructure using MATLAB. Finally, a detailed parametric analysis was conducted to study the effects of varying laser power, scanning speed, and preheating temperature.

The numerical results showed that the maximum temperature and Marangoni convection in the molten pool increased at higher laser powers, higher preheating temperatures, and lower scanning speeds. The particle-voided region was significantly large with high Marangoni convection but decreased with weaker Marangoni convection. The simulated microstructure was dominated by large columnar grains when nanoparticles were not considered. The introduction of nanoparticles disrupted the columnar grain growth by promoting small, randomly oriented, equiaxed grains. A decrease of 30%-40% in average grain diameter was measured at the cross-section of the solidified layer when nanoparticles were present. The qualitative comparison of the microstructures showed that the grains were smaller in the uniformly distributed particle region compared to the particle-voided region.

CHAPTER ONE

INTRODUCTION

Thermo-fluidic transport phenomena and the diffusion of solid particles in liquid metal are of prime interest in the metal additive manufacturing process for its rise in numerous engineering applications. These phenomena play an essential role in shaping microstructural features and controlling the mechanical properties such as tensile strength, ductility, hardness, wear resistance, etc., of the manufactured part. Metal additive manufacturing can be used to fabricate parts with complicated designs by adding materials by layer. This process significantly reduces post-processing time than conventional material processing methods such as casting molds and tooling. Hence, it has gained huge demand in aerospace, automotive, power generation, food, and biomedical industries to fabricate functional prototypes and high-performance products [1–3]. Selective Laser Melting (SLM) process is considered one of the most popular additive manufacturing techniques for metal alloys and their matrix composites. This process is also known as Laser Powder Bed Fusion (LPBF) and Direct Metal Laser Melting (DMLM). In this process, a high power-density laser scans over the pre-placed metal powders to melt and fuse with the underlying material. This process is repeated to form one layer after another until the whole part is manufactured.

Nanoparticles are added with the metal powders to form metal matrix nanocomposite, enhancing the mechanical properties of the produced part [4–7]. The SLM process involves several interconnected thermal and physical aspects that affect rapid melting and solidification. As the incident laser energy source interacts with the surface of the powder particles, it creates a liquid melt pool region with solid nanoparticles inside it. The liquid metal inside the melt pool is driven

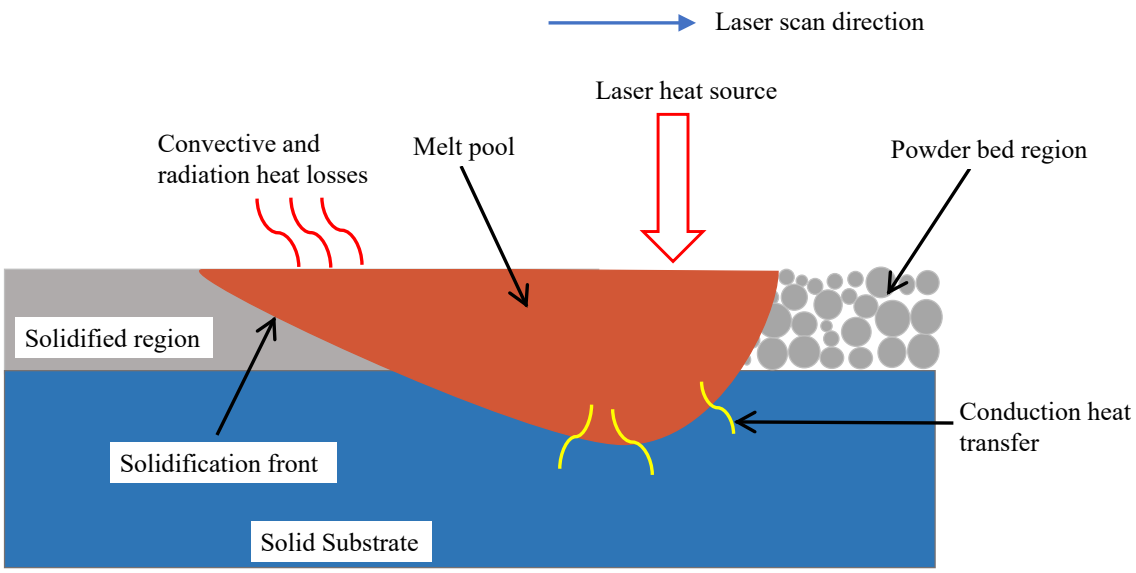


Figure 1.1. Typical selective laser melting process.

by Marangoni force and buoyancy and redistributes the solid nanoparticles. As the laser heat source moves away from the melt pool region, heat is diffused by conduction, convection, and radiation from the melt pool to the surrounding metallic material and the ambient atmosphere, solidifying the region. The process parameters of SLM and the material properties of both metal powders and nanoparticles control these various phenomena. They subsequently affect the microstructure formation and mechanical properties of the final product. Some of the critical process parameters of SLM are laser power, laser scanning speed, powder layer thickness, laser preheating temperature, and nanoparticle weight fraction. The manufactured part can obtain desired microstructure and mechanical properties by optimizing these process parameters. However, the literature is scarce about the effect of process parameters on SLM-produced metal matrix nanocomposites.

Motivation

Despite the massive potential of the SLM-built nanocomposites, how different physical aspects influence the nanoparticle diffusion, microstructure, and mechanical properties of the produced part is not fully understood yet. Proper understanding of these interconnected phenomena is of prime importance to optimize and control the SLM process parameters. During this process, the laser-powder interaction time is in the range of a few microseconds. The resulting rapid melting and solidification generate melt pool dimensions in the order of tens to a few hundreds of micrometers [8]. As a result, finding accurate temperature profiles, melt pool dynamics, and instantaneous nanoparticle diffusion through experimental measurement is extremely difficult. In addition to that, it is very challenging to experimentally observe the microstructure morphology because of the high temperature and rapid solidification rate. Optimizing process control parameters by experimental measures requires numerous trials and errors, adding material cost. Therefore, numerical models of the SLM process have received considerable attention, complemented by the fact that it can cover a wide range of spatial-scale and is less expensive than experimental investigation.

Furthermore, with the advancement of computational fluid dynamics (CFD) software, the SLM process can be simulated to quantify thermo-fluidic characteristics with reasonable accuracy and efficiency. Afterward, a microstructure model such as Cellular automata [9–15] can simulate the grain growth during solidification from the computed temperature history. Grain size and orientation can be measured from the predicted microstructure, which is directly related to the mechanical properties of the built part. A significant amount of literature is available on numerical modeling of the SLM process for metal alloys [11,16–23]. Details regarding temperature

distribution, melt pool shape, grain size, and texture can be found in these numerical studies. These studies were conducted for different laser process parameters. However, very little information is available on nanoparticle diffusion and its influence on the microstructure of the nanocomposites for this process. Therefore, it is vital to understand these physical phenomena both quantitatively and qualitatively to impart enhanced mechanical properties to the manufactured part.

Literature Review

Numerous numerical and experimental studies have investigated the SLM process for common structural metals such as steel, aluminum, and titanium alloys. The application of SLM to fabricate parts with various aluminum alloys is very attractive to researchers for its wide application in industrial production. Aluminum alloys are lightweight, possess a higher strength-to-weight ratio, and have excellent corrosion resistance. Conversely, they also exhibit lower strength, stiffness, and wear resistance than other alloys. However, SLM-built aluminum alloys demonstrated better mechanical properties than alloys manufactured by the conventional fabrication method such as die-casting, stir casting, vacuum casting, and squeeze casting [24,25]. During the SLM process, aluminum alloys with the presence of silicon (Si) also exhibited better mechanical properties than the base aluminum metal. Since silicone (Si) improves the fluidity of molten aluminum, thermal distortion during solidification is reduced [4]. Read et al. [25] fabricated AlSi10Mg alloy specimens by SLM and reported that desired mechanical properties could be achieved by optimizing SLM process parameters. They accounted that those samples have better strength, elongation, and creep properties than die-cast aluminum alloys. Nonetheless, they have some downsides while being used in SLM because of their thermo-physical properties [25–27]. The low thermal absorptivity of aluminum alloys prevents them from extracting heat from the laser

radiation efficiently. In addition, their high thermal conductivity diffuses the heat away from the laser source very quickly rather than concentrating the thermal energy to melt the powder bed. Furthermore, SLM fabricated aluminum alloys form vertically oriented coarse columnar grains. For these reasons, defects such as insufficient fusion, thermal distortion, and anisotropy in mechanical behavior are shown in the final built part.

Ceramic microparticles have been reinforced in the aluminum matrix to overcome the limitations of aluminum alloys fabricated by SLM process [4,28]. The reinforcement selection should be such that the aluminum metal matrix composite (AMC) can demonstrate i) higher heat absorptivity and ii) lower heat conductivity. In addition, reinforcements should have a higher melting point than the aluminum alloy and create a stable interface with the aluminum alloy matrix. Based on these criteria, TiB_2 [7,28] and TiC [6,29] are considered ideal reinforcements for aluminum alloy matrix. In their experimental work, Xi et al. [28] reinforced TiB_2 microparticles with AlSi10Mg alloy, varying weight content from 1% to 5%. This work indicated that the weight fraction is crucial for finding desired mechanical behaviors, and aluminum matrix composites have refined grain size, higher tensile strength, and better wear resistance than unreinforced aluminum alloys. However, they had not found any improvement in ductility. Montero Sistiaga et al. [30] investigated a similar process. They concluded that SLM-built AMC tends to fail prematurely because of the presence of micropores in the built part, acting as a source of crack propagation. Gu et al. [29] found that the mechanical properties of the aluminum metal matrix composites can be improved if nanoparticles are reinforced instead of microparticles. The authors created AlSi10mg samples with SLM, reinforced with TiC nanoparticles to produce aluminum metal matrix nanocomposite (AMNC). The authors observed an increase in tensile strength without

significant loss of ductility in these nanocomposites. They described that the contributing factors for this phenomenon were grain refinement and grain boundary strengthening caused by the formation of novel ring structures by TiC nanoparticles. The evolution of this novel ring structure is attributed to the presence of the recirculation zone in the melt pool driven by Marangoni and buoyancy flow. They added that the novel ring structure of nanoparticles around the aluminum alloy matrix increased interconnection and interface bonding, enhancing load transfer between the matrix and the reinforcements. In addition, the uniform distribution of ring structures at the grain boundaries constrained crack propagation. As a combined effect, tensile strength increased without significant loss in ductility. Likewise, Xiao et al. [7] introduced 5.6 wt% nano-TiB_2 with AlSi10mg alloy powder and noted that SLM-produced samples exhibited improved tensile strength and ductility. They examined the microstructure and texture evolution and found fine equiaxed grains in their produced samples. It was described that nano-TiB_2 acted as heterogeneous nucleation sites to inhibit columnar grain growth and reduce anisotropy in grain orientation.

The thermal and fluid dynamic behaviors of the SLM process can be quantified with a CFD model, governed by mass, momentum, and energy conservation equations. Finite volume and finite element methods are commonly used to solve any CFD problem. CFD model for SLM process integrates modeling of various physical phenomena such as: moving laser heat source, temperature-dependent material properties, phase transition from powder to bulk material, melting and solidification, Marangoni convection, and deformation of the solidified region. Two different approaches are used to model the powder bed region: the powder-scale and the continuum-scale models. With the powder-scale model, the powder bed region considers the geometry, size, and distribution of the powder particles. Whereas, on the continuum scale, the powder bed region is

assumed to have effective thermophysical properties, calculated from the porosity of the powder bed and the size of particles. The powder scale model offers higher accuracy in the micro-scale and can effectively predict different defects such as balling phenomena, spattering, denudation, and porosity [11,21], but is extremely computationally expensive. Therefore, with relatively lower computational cost, the continuum scale model is a practical modeling approach to provide reliable results.

Finite element-based thermal conduction models are implemented in several studies to calculate temperature field, melt pool size, and solidification parameters. Karayagiz et al. [18] presented a heat conduction-based FE model to predict the thermal history and melt pool size for Ti alloy, validated with experimental measurement. Foroozmehr et al. [20] also developed a similar thermal FE model for single track simulation, considering a volumetric 3D Gaussian heat source to predict temperature profile. Optical penetration depth of the laser beam into the powder bed was considered in their study to account for laser reflection and scattering within the powder particles. The simulated results showed good agreement with the experimental remelted zone in the substrate. Liu et al. [23] followed this approach to predict the microstructure composition of AlSi10mg alloy using the calculated thermal variables. Their prediction was in reasonable agreement with the experimental microstructures. Nevertheless, as Marangoni convection on the interface of air and liquid metal is the primary mechanism of the convective flow of the melt pool, neglecting this effect makes the calculated temperature distribution and solidification parameters incorrect and misleading [31].

A number of researchers adopted the continuum scale approach to investigate thermo-fluidic phenomena. Mukherjee et al. [16] developed a three-dimensional, transient heat transfer

and fluid flow model for laser powder-based fusion process with traveling fine grid-system to compute temperature and velocity field. A 3D Gaussian distributed moving heat source was used to model the absorption of laser radiation. Temperature-dependent alloy and powder properties were considered in their proposed model, which was critical for accurate results. The model was validated with experimental melt pool shapes for 316 Stainless steel and Ti-6Al-4V alloy. This same modeling framework was employed in their subsequent work [19]. The model calculated temperature and velocity fields for commonly used alloys. Melting and solidification of the alloys were simulated for multiple laser scan tracks and multiple build layers. This study further investigated the influence of various SLM process parameters such as laser power, laser scanning speed, laser spot radius, layer thickness, and hatch spacing on the shape of the fusion zone, solidification morphology, mechanical properties, and various defects.

Though the SLM part is built in several layers, and each layer comprises different scan patterns, the quality of the part depends on the quality of each single scan track. Understanding these aspects in a single scan tack is particularly important to improve the SLM technique. Mishra et al. [22] presented a three-dimensional CFD model for single scan track selective laser melting of Ti-6Al-4V alloy using a volumetric heat source. Due to the symmetric nature of the problem, simulation was done in a half domain, considering the midplane parallel to the laser scanning path as the plane of symmetry. The model predicted melt pool size with reasonable accuracy for low to medium laser energy densities. The model also calculated porosity and solidification parameters with varying laser power and laser scan speed. Based on the simulated results, the model calculated the optimum laser energy density of 50-70 J/mm^3 for Ti-6Al-4V alloy. Calculated solidification parameters such as thermal gradient and cooling rate indicated the formation of columnar grains

in the resolidified region. Jamshidinia et al. [17] investigated single scan track temperature distribution and melt pool dynamics during electron beam melting of titanium alloy using ANSYS Fluent. Electron beam melting is a similar metal additive manufacturing technique as SLM, where an electron beam is used as a heat source. The study assumed the same temperature-dependent density of powder bed and solid substrate to simplify the calculation of the conservation equations. The effect of porosity was taken into account for quantifying the equivalent thermal conductivity of the powder bed. Simulated melt pool dimensions were validated with experimental measurements. Melt pool dimensions were compared between the thermal conduction-based [18,20] and coupled thermo-fluid models. The thermo-fluid model considering molten metal convection, generated wider and shallower melt pools than the conduction-based model.

Yuan et al. [6] followed a similar approach to simulate thermo-fluidic behavior for TiC/AlSi10Mg nanocomposite during SLM process. The weight fraction of the reinforcement was taken into account to find equivalent thermal properties for both powder and bulk material. Laser heat absorption increased while the thermal conductivity of metal matrix composite decreased with the inclusion of TiC nanoparticles. The study also investigated the surface and the cross-sections of the experimentally built samples to examine the defects and the quality of the fabricated part. Their study indicated that dense and defect-free samples could be obtained at optimum laser processing parameters. Otherwise, defects such as balling phenomena and micropores took place. Balling phenomena occurred at lower laser energy density when the melted liquid metal could not spread over the powder particles because of the instability in thermo-capillary forces acting on them [32,33]. As a result, liquid metals solidified as balls near the unmelted powder particles. Gu et al. [8] studied the temperature and velocity distribution varying the nanoparticle's weight

fraction in their subsequent work. The study concluded that heat accumulation and Marangoni convection intensified, while the viscosity of the liquid melt decreased with the increase of nanoparticle content. Another purpose of this study was to numerically investigate the formation mechanism of the novel ring structure of TiC nanoparticles. This phenomenon was observed in their experimental work in the microstructures of the fabricated samples [28]. The velocity field obtained from the simulation was used to discuss the nanoparticle's migration behavior within the melt pool. Nanoparticle movement strongly followed the circular motion caused by Marangoni convection. The low viscosity at higher nanoparticle content generated less viscous drag on the nanoparticle, favoring the circular motion of the nanoparticle. The centrifugal force pushed the nanoparticles away from the center of the circular path to the periphery. As a result, nanoparticles formed a ring structure when their weight fraction was relatively higher. However, no definite ring structure was observed at lower nanoparticle content.

AlMangour et al. [5] further corroborated that the arrangement of nanoparticles and dispersion state is considerably influenced by Marangoni convection and melt pool viscosity. This work studied the impact of laser energy density on the distribution of nanoparticles, and grain size of SLM produced TiC/316L stainless steel nanocomposites. The nanoparticle dispersion mechanism was explored based on a thermal multi-layer simulation of the SLM process. From the microstructure images, they observed that nanoparticles tend to aggregate into clusters at low laser energy density, while at high laser energy density, nanoparticles formed continuous uniform ring structures. Furthermore, as the melting point of TiC nanoparticles are higher than steel, unmelted TiC nanoparticles can act as nucleation sites for molten stainless steel. Increase of nucleation sites promoted heterogeneous nucleation during solidification, causing refinement of grains.

Some of the studies mentioned above provided qualitative information regarding the dispersion of nanoparticles. However, only a few studies can be found in the literature that incorporated tracking of reinforcement particles for additive manufacturing process. These studies are done in commercial CFD software, ANSYS FLUENT using its discrete phase modeling framework. Dai et al. [34] proposed a three-dimensional model for selective laser melting of AIN/AlSi10Mg considering the diffusion of reinforced microparticles in the molten pool. The dispersion state of the reinforced particles was compared for varying laser energy density. As the laser energy density decreased, the final distribution state of reinforced particles changed from the formation of local clusters to homogenous distribution in the solidified region. The simulated distribution of nanoparticles closely matched with the observation from microstructure images of the experimentally built samples. Rahman et al. [35] developed a two-dimensional CFD model incorporating nanoparticle tracking, Marangoni and buoyancy convection, and solidification phenomena to simulate the laser cladding process. In this model, SiC nanoparticles were initially uniformly distributed in liquid titanium, leading to solidification by natural convection at the top surface. Marangoni convection and convective heat loss were selected as boundary conditions at the top wall. Because of Marangoni and buoyancy convection, a quasi-equilibrium recirculation zone formed within liquid titanium. Nanoparticles were trapped in the recirculation zone until the solidification front captured the nanoparticles. The study investigated the influence of Marangoni number and convective heat transfer coefficient on the dispersion of nanoparticles. The results indicated that local nanoparticle-clusters and nanoparticle voided zones formed in different parts of the geometry at an increased Marangoni number. It was further reported that the diffusion of nanoparticles depended on the solidification rate of the top wall.

SLM process parameters not only affect the thermo-fluidic behavior but also play a key role in the formation of microstructure during solidification. Furthermore, the mechanical properties of the final product are affected by the microstructure. Therefore, predicting microstructural grain size and orientation can provide insights to optimize the process parameters to build a product with the desired mechanical properties. Several research investigations employed microstructure modeling tools to understand the fundamentals of microstructure evolution during rapid solidification inherent in the SLM process. Most commonly, three types of microstructure modeling methods are reported in the literature: i) Phase Field (PF) modeling [36], ii) Cellular Automata (CA) modeling [37], and iii) Kinetic Monte Carlo (KMC) modeling [38]. Tan et al. [39] compared these microstructure models considering different features. They accounted that the Phase field modeling offered the highest accuracy and details in microstructural features of those three. The shape of primary and secondary dendrites, solute concentration, and precipitates could be simulated using the Phase-field modeling. The drawback of PF simulation was that it used very high computational resources and was limited to small length scales compared to other methods [36]. The CA method provided a good balance between accuracy and computational cost, while the accuracy in the KMC model was not satisfactory. An entirely probabilistic method was used in the KMC model. In addition, it could predict the grain sizes and shapes but could not predict the shape of the primary dendrites [38]. The CA model used more computational resources than the KMC model. However, the Cellular Automata (CA) model predicted the shapes and orientations of the primary dendrites with better accuracy than the KMC model using a combination of probabilistic and deterministic methods [37]. The primary dendrites are the most important microstructural feature in microstructure modeling [39]. Thereby, it was

regarded as an effective approach to predict grain size and orientation during the solidification of metallic materials using the CA microstructure model. This method was first introduced by Rappaz et al. [40] to simulate grain structure formation during solidification under uniform temperature conditions. The proposed two-dimensional model was applied for cubic metals, having preferential growth in the ⟨100⟩ direction along their crystallographic orientation. The preferential growth mechanism of cubic crystals is described in chapter 2. Nucleation of grains was taken into account from the mold-liquid interface and in the bulk of the liquid. Nucleation sites were randomly selected in the computational domain, as well as the grain orientation of the nucleated grains, among a certain number of orientation classes. The texture of the simulated grain was qualitatively compared with experimental results and provided a reasonable prediction of grain structures. Afterward, the same research group coupled finite element temperature distribution to propose a two-dimensional [9] and three-dimensional [10] cellular automata finite element (CAFE) model. The models simulated dendritic grain formation under non-uniform temperature conditions. The temperature field calculated from the finite element model was interpolated into the CA domain at each time step to calculate nucleation and grain growth. A 2D "decentred square" and 3D "decentred octahedron" CA growth algorithm was applied to track the dendritic tip velocity. These models closely matched with experimental data and provided useful information regarding grain structures, i.e., epitaxial nucleation from melt pool boundary, competitive grain growth, and columnar-to-equiaxed transition (CET).

The CA modeling algorithm introduced by this research group [9,10] was implemented in numerous studies by other researchers for commonly used alloys in the SLM process. Gerstgrasser et al. [13] developed a two-dimensional coupled CAFE microstructure model for a single track

SLM process. The authors studied the microstructure formation of 316 Stainless steel and nickel base alloy CM247LC, incorporating solute diffusion of alloy elements and neglecting bulk nucleation. Heat flow calculation was executed on a 3D model, considering a moving volumetric heat source. CA domain was selected on a transverse plane perpendicular to the direction of the moving laser. The temperature field of the selected transverse plane was interpolated into the CA domain. Microstructure evolution was investigated for two different scanning speeds, i.e., 1000 mm/s and 1600 mm/s, and was quantitively and qualitatively compared with experimental results. The grain size, measured with Heyn lineal intercept method [41], was in good agreement with experimental data. The model predicted that columnar grains were prevalent in the solidified region and oriented along the direction of the local temperature gradient. The study further reported that grain size was smaller for higher scan speed caused by the increase in cooling rate. Similar approaches were undertaken by Ao et al. [12] for aluminum alloy, Akram et al. [15] for 316 Stainless steel, and Ansari Dezfoli et al. [14] for nickel alloy for 2D microstructure simulation coupled with 3D FE models for SLM process. These studies reported that columnar grain was predominant in the simulated grain structure, along with fine equiaxed grains developed at the top of the melt pool. These observations showed that high temperature gradient and cooling rate associated with the SLM process promoted the growth of columnar grains.

3D CAFE microstructure modeling was also employed in a few studies for investigating underlying grain growth features overlooked in 2D models. Mohebbi et al. [37] and Zinovieva et al. [42] investigated microstructure formation in 3D under different laser process parameters. Zhang et al. [11] introduced a modified decentered algorithm for the 3D CA microstructure model coupled with CFD to predict the microstructure evolution of 316 Stainless steel during the SLM

process. These models indicated that the grains had a 3D orientation along the direction of the local thermal gradient. To rectify the grain growth algorithms in 2D CA models, Ao et al. [12] and Akram et al. [15] introduced an anisotropic coefficient for grain growth considering the angle between grain orientation and the projected 2D direction of the local thermal gradient at the solidification front. This angle was defined as the misorientation angle. The grains that had the smaller misorientation angles were favored to grow over the grains with larger misorientation angles. Likewise, Paul et al. [43] included this phenomenon in their proposed discrete dynamics model to simulate epitaxial columnar grain growth. This model was analogous to the CA modeling framework and was more efficient than that.

Both bulk and epitaxial nucleation mechanisms during solidification are critical solidification phenomena during selective laser melting of metal alloys. However, many researchers have disregarded bulk nucleation mechanisms for simplification. As a result, these models cannot predict the CET transition, imparting erroneous grain size information. Unlike other common alloys, AlSi10Mg exhibits a unique feature in microstructure formed during selective laser melting. Observing Electron Backscatter Diffraction (EBSD) images, Thijs et al. [44] reported that equiaxed grains formed at the melt pool boundary at the SLM-built samples. Mohebbi et al. [37] described this aspect as fusion boundary nucleation and integrated it into their 3D CAFE model. They discussed that precipitated Si particles located at the melt pool boundary could act as nucleation sites, promoting the growth of equiaxed grains. However, Liu et al. [23] had not observed fusion boundary nucleation in the microstructure of a single scan track. Based on this fact, Ao et al. [12] ignored fusion boundary nucleation for single-layer 2D CA microstructure modeling of AlSi10Mg alloy for SLM. In this study, the authors presented a dendritic growth

model taking competitive growth and bulk nucleation mechanisms into account. A combination of thermodynamic, composition, and curvature undercooling were considered the driving forces for grain growth. These modeling aspects of grain growth are described in the following chapter. Ao et al. [12] also examined the effects of laser scanning speed, scan spacing, and preheating temperature on the dendritic grain structure. The results showed that the size of equiaxed grains increased with either increasing the preheating temperature or reducing the scanning speed. Moreover, epitaxial columnar grains became longer and narrower with increased scan spacing for multi-track simulation.

As stated earlier, adding reinforcement particles in the metal matrix can refine the grain sizes and improve mechanical properties. A significant amount of research was focused on the experimental analysis of the microstructures of SLM fabricated metal matrix composites (MMC) and metal matrix nanocomposites (MMNC). However, only a few studies were found for microstructure modeling for these metal composites. Yang et al. [45] first introduced reinforced nanoparticles in a Phase-field microstructure model to analyze the grain refinement process. The model considered uniform distribution of TiB_2 nanoparticles in the metal matrix, acting as heterogeneous nucleation sites. However, the restriction of grain boundary movement by nanoparticles, defined as the Zener pinning effect [46], was neglected here. The simulation results showed that elongated grains are distributed at the melt pool boundary. In contrast, a large number of fine equiaxed grains were located at the interior of the melt pool. The authors reported that the simulated microstructures were qualitatively in good agreement with experimental data. Nonetheless, the grain size measured from the simulated results was slightly larger than the experimental data for ignoring the Zener pinning effect. Their subsequent study established a

comprehensive Phase-field modeling framework, including heterogeneous nucleation and Zener pinning of reinforced particles [47]. The results matched with experimental data both qualitatively and quantitatively. Further investigation on the effects of the weight fraction of TiB_2 microparticles suggested that both columnar and equiaxed grain sizes reduced with the increase of microparticle content.

To date, limited studies have included the migration of reinforced nanoparticles for CFD and microstructure models to simulate the SLM process. Additionally, no information can be found collaborating nanoparticle diffusion and microstructure morphology for selective laser melting of nanocomposites. Moreover, coupling various sophisticated models to simulate various aspects of the SLM process compromises the efficiency of the numerical model. Therefore, a simplified model must be formulated to explore the microstructure evolution and nanoparticle distribution under different process parameters. Hence, a comprehensive three-dimensional CFD model was developed to analyze the SLM process for this study. This model involved heat conduction, thermal energy absorption, Marangoni and buoyancy convection, phase change, and nanoparticle tracking. Furthermore, the calculated temperature history and nanoparticle redistribution were coupled with a 2D CA model to analyze the effects of various parameters on the simulated grain structure. The present study was focused on a single scan track to reduce complexity and computational time. As mentioned earlier, aluminum nanocomposites have a wide range of engineering applications for their excellent mechanical properties [27]. Hence, AlSi10Mg was chosen as the metallic material for the powder bed and substrate region, while TiB_2 was selected as nanoparticles in the present study to explore the formation of aluminum nanocomposites.

CHAPTER TWO

PROBLEM FORMULATION

Concept

As shown in Fig 2.1, selective laser melting (SLM) process, metal powders and nanoparticles are pre-placed on a substrate, defined as the powder bed. Then, a moving laser heat source scans over the powder bed in a pre-defined direction, set in a CAD software [48]. The thermal energy generated by the moving laser melts the metal powder and the underlying substrate along its path, creating a melt pool region. However, the reinforced nanoparticles remain in solid state because of their higher melting temperature than the melting temperature of the metallic material. As a result, nanoparticles disperse through the liquid melt pool region until the melt solidifies. Liquid metal flow caused by Marangoni and buoyancy force impact the distribution of nanoparticles. The homogenous distribution of nanoparticles inhibits the growth of large columnar dendritic grains and forms fine equiaxed grains in the solidified region [49]. The present study dealt with computational fluid dynamics analysis of nanoparticle dispersion in the melt pool during the SLM process. The final distribution of nanoparticles was incorporated in a Cellular Automata microstructure model to investigate the evolution of grains during solidification. The grains sizes were computed from the simulated microstructure and compared for various process parameters.

The computational domain for the three-dimensional CFD model of SLM consists of powder bed and substrate and is shown in Fig. 2.1. A cuboid-shaped domain of dimensions $1000\times300\times350\ \mu m^3$ is selected for numerical analysis. The size of the simulation domain was determined such that the temperature distribution at the boundary of the domain did not affect the

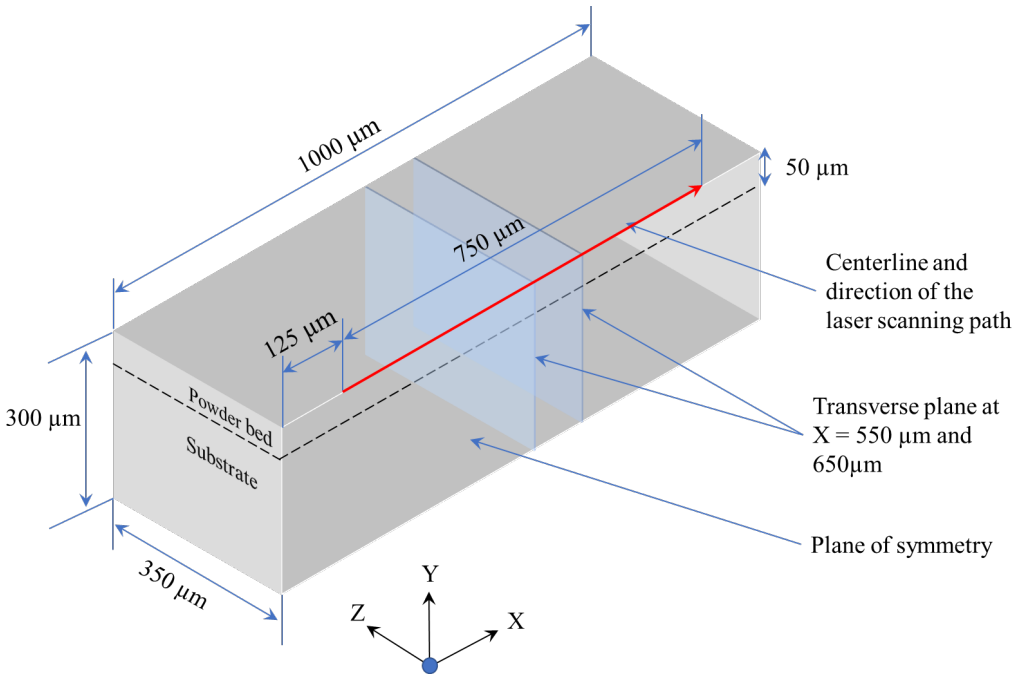


Figure 2.1. Schematic illustration of the CFD computational domain.

melt pool activity along the laser scan path. For simplicity, a single scan track of 750 µm was chosen along the x-axis. The moving laser heat source that drives the melting and solidification is Gaussian in nature [18]. Therefore, it was assumed symmetric along the midplane parallel to its scanning path. The simulations were carried out in a half domain to increase computational efficiency by taking advantage of the symmetry in overall geometry, heat source, fluid dynamics, and boundary conditions. The interaction between the moving laser and the metallic materials was modeled using a volumetric heat source. Additionally, the effects of Marangoni force, buoyancy force, and temperature-dependent material properties were considered. Furthermore, the melting and solidification of the base material were modeled using the enthalpy-porosity technique. The top wall was subjected to convection, radiation, and vaporization heat loss, and the bottom of the substrate was considered insulated. As shown in Fig. 2.1, all other walls except the plane of symmetry had convection and radiation heat losses.

AlSi10Mg alloy was selected as the material for the powder bed and the substrate region. Along with that, titanium diboride (TiB_2) was chosen as the nanoparticles in the present study. 60,000 solid nanoparticles with a constant diameter of 80 nm were uniformly distributed in the powder bed region. The weight fraction of the nanoparticles was very small (0.0009%) compared to the base powder material. Therefore, the Eulerian-Lagrangian approach was considered in this model. The melting and solidification of AlSi10Mg were modeled using the Eulerian method, while nanoparticle tracking was performed in the Lagrangian framework. In this study, the nanoparticles only interacted with the top wall of the computational domain, which was assumed as the interface between ambient air and the liquid melt pool. Nanoparticles have the tendency to accumulate at the gas-liquid interface because of their affinity toward the fluid interfacial region [50]. To model this phenomenon in the current model, the boundary condition for the nanoparticle transport model was set up to be trapped by the top wall. This boundary condition became active once the centroid of the nanoparticle reached the top surface. In addition, the size of the nanoparticles was very small compared to the primary dendrite spacing of the solidification front [51]. Hence, it was assumed that nanoparticles were captured by the solidification front when the front interacted with the nanoparticles.

A 2D Cellular Automata model was coupled with the CFD model to simulate grain structure evolution along the transverse plane (x-z plane) at x = 550 μm and 650 μm. Computed temperature field, thermal gradient, and final nanoparticle positions at those transverse planes were imported into the CA model. The Cellular Automata model and its coupling with the CFD model are described later in Chapter 4. A commercial CFD code ANSYS Fluent, version 2021 R2 [53], with the double precision option, was used to analyze the heat and fluid flow and nanoparticle

transport during the SLM process. Several User Defined Functions (UDF) were developed to include the temperature-dependent material properties, moving heat source, and thermal boundary conditions at the top surface of the computational domain. The simulated results were validated with published experimental data. In addition, the particle transport model of ANSYS Fluent was validated with a published numerical result. The temperature field and nanoparticle locations at two transverse planes of the CFD domain were coupled with a 2D Cellular Automata model to simulate the microstructure formation. The Cellular Automata microstructure model was developed using a MATLAB script. The microstructure model was validated both qualitatively and quantitatively with published data. The numerical analysis was done in Intel Xeon E3-1225 v3 CPU with four processors. The CFD simulation was done parallelly on four processors, while the CA microstructure simulation was run in serial computation using a single processor.

CFD Modeling of the SLM process

Assumptions

The following assumptions were made for the CFD analysis:

1. The fluid was incompressible and Newtonian.
2. Liquid metal flow in the melt pool was assumed to be laminar.
3. A constant density value was applied for the material's powder, liquid, and solid phases[17]. Boussinesq approximation was used to take the buoyancy forces into consideration due to changes in density [16,19].
4. The top surface of the powder bed, molten pool, and the solidified region was assumed to be flat [16,18]. The change in volume during the melting and solidification was not taken into account.

5. The powder bed was assumed to be a homogenous continuum media neglecting the pores in the geometry of the model [16,22].
6. Material loss due to vaporization was considered negligible. Only heat loss due to vaporization was considered at the top surface [54].
7. Nanoparticles were regarded as discrete phases, and their calculation was done in the Lagrangian framework. Both the powder bed and the substrate region were considered continuum media, working in the Eulerian framework [35].

Governing Equations

The heat and fluid flow model was governed by the conservation of mass, momentum, and energy equations. These equations were solved in a three dimensional Cartesian coordinate system. A set of partial differential equations was used to express these conservation laws which was discretized with the finite volume method.

Conservation of Mass

Conservation of mass can be expressed in the continuity equation:

$$\vec{\nabla} \cdot \vec{u} = 0 \tag{2.1}$$

Here, $\vec{u}$ is the velocity vector of the fluid.

Conservation of Momentum

The conservation of momentum conservation equations, which are commonly referred to as Navier-Stokes equations, govern the fluid flow. They are expressed as:

$$\frac{\partial(\rho\vec{u})}{\partial t} + \vec{u} \cdot \nabla(\rho\vec{u}) = -\nabla p + \nabla \cdot \mu \left(\nabla\vec{u} + (\nabla\vec{u})^{T}\right) + \vec{F} \tag{2.2}$$

where, ρ is the density, p is the pressure, and μ is the dynamic viscosity of the fluid. $\vec{F}$ is the additional body force term referring to the buoyancy force and mushy zone flow resistance during liquid-solid phase change. It is given by:

$$\vec{F} = \overrightarrow{F_{Buoyancy}} + \overrightarrow{F_{Mushy}} = \rho\vec{g}\beta(T - T_{ref}) + \frac{(1-\beta_L)^2}{(\beta_L^3 + \varepsilon)} A_{mushy}\vec{u} \tag{2.3}$$

The significance of buoyancy and mushy zone flow resistance has been detailed in the latter part of this chapter.

Energy Equation

The following equation can express the conservation of energy:

$$\frac{\partial(\rho C_p t)}{\partial t} + \vec{u} \cdot \nabla(\rho C_p T) = \nabla \cdot (k\nabla T) + q \tag{2.4}$$

where, C_p is the specific heat capacity, T is the temperature, k is the thermal conductivity, and q is the moving laser heat source. In the present study, a volumetric heat source is used to model the moving laser, which is Gaussian in the horizontal (x-z). Additionally, optical penetration depth and Beer-Lambert's law are considered in the heat source model [22,23].

$$q = \frac{2\alpha P}{\pi r_b^2 S_L} \exp\left(-\frac{2(x - V_L t)^2 + z^2}{r_b^2}\right) \exp\left(-\frac{|y - y_0|}{S_L}\right) \tag{2.5}$$

Here, P is the laser power, α is the thermal absorptivity of the metal, and r_b is the laser spot radius. S_L is the optical penetration depth which accounts for the thermal energy induced at a depth y from the powder layer surface due to the laser radiation.

Initial and Boundary Conditions

In addition to the governing equations, boundary conditions are used to define the problem completely. At the top surface of the simulation domain, heat losses occur through convection and

radiation. Also, vaporization heat loss is taken into account. The thermal boundary condition at the top wall is given by:

$$-k\left(\frac{\partial T}{\partial y}\right)_{y=0} = h_c(T - T_\infty) + \sigma_S \varepsilon(T^4 - T_\infty^4) + Q_v \tag{2.6}$$

where convection heat transfer coefficient and the surrounding temperature are denoted by h_c and T_∞, respectively. In Eq. 2.6, σ_S is the Stefan-Boltzmann constant, and ε is the emissivity. Q_v is the vaporization heat loss which is modeled [11] by the following equations:

$$Q_v = \Delta H_v J_v \tag{2.7}$$

$$J_v = 0.82 P_v / \sqrt{2\pi M R_g T} \tag{2.8}$$

$$P_v = 0.54 P_a \exp\left(\frac{\Delta H_v}{R}\left(\frac{1}{T_b} - \frac{1}{T}\right)\right) \tag{2.9}$$

where, ΔH_v denotes the latent heat of vaporization and J_v is the evaporated mass. Molecular mass and the universal gas constant are denoted by M and R_g, respectively. P_v is the vaporization pressure in Eq. 2.9 where, P_a is the ambient pressure and T_b is the boiling temperature of the liquid metal which is 2743 K.

The thermal boundary condition for the bottom wall of the substrate is considered insulated. Except for the plane of symmetry, the remaining walls have convection and radiation heat losses as the thermal boundary conditions. The heat exchange at the surface of the liquid metal induces a significant temperature gradient within the molten pool. This temperature gradient yields a surface tension gradient that drives the Marangoni convection of the liquid metal. This effect is modeled as the Marangoni shear stress boundary condition at the top wall by the following equations:

$$-\mu\frac{\partial u_x}{\partial y}=\frac{\partial\sigma}{\partial T}\frac{\partial T}{\partial x} \tag{2.10}$$

$$-\mu\frac{\partial u_z}{\partial y}=\frac{\partial\sigma}{\partial T}\frac{\partial T}{\partial z} \tag{2.11}$$

Here, $\frac{\partial\sigma}{\partial T}$ is defined as the surface tension coefficient, u_x and u_z are the components of the tangential velocity on the liquid metal surface.

The initial condition for powder and solid region is setup as follows:

$$T(x,y,z,0)=T_0 \tag{2.12}$$

where, T_0 is the preheating temperature of the SLM process.

Thermophysical Properties

The powder bed in the SLM process comprises alloy powder particles and pores filled with shielding gas. The continuum modeling approach formulates an effective thermal conductivity and absorptivity for the powder bed material. This formulation is based on the size and void fraction of the powder particles shown in Eqs. 2.13 and 2.14. The effective thermal conductivity model is expressed as follows:

$$k=\begin{cases}k_p=(1-\sqrt{1-\emptyset}\,(k_a+\emptyset k_r)+\sqrt{1-\emptyset}\left\{\frac{2}{\frac{1}{k_a}-\frac{1}{k_m}}\left[\frac{1}{1-\frac{k_a}{k_m}}\ln\left(\frac{k_m}{k_a}\right)-1\right]+k_r\right\}; \text{powder state}\\ k_m\ ; \text{liquid or solid state}\end{cases} \tag{2.13}$$

$$k_r=4F_{view}\sigma_s T_p^3 D_p \tag{2.14}$$

Here, k_p, k_m and k_a are thermal conductivities of the powder state, metal state, and shielding gas, respectively and k_r is the internal radiation of the powder bed. In this study, k_m is temperature dependent, and the value for k_a is constant at 26.5 (W/mK). The expression for k_m is given in Table 2.1. F_{view} is defined as the internal radiation factor with a value of $\frac{1}{3}$. Tp and Dp denote

particle temperature and average diameter, respectively, and ∅ is the porosity of the particle bed. Initially, the temperature conductivity of the powder is calculated by k_p and is expressed in Eq. 2.13. Here, the powder bed is heated by a moving laser energy source. When the temperature of the powder particles rises up to the liquidus temperature of the aluminum alloy, T_L, its powder state is changed to liquid by the melting process. Then the material's thermal conductivity is switched to k_m from k_p. After the heat is diffused, the temperature of the molten liquid cools down below the solidus temperature, T_S. Hence the material's liquid state changes to a solid state during solidification. However, in this solidification process, the thermal conductivity still remains k_m. The material in the substrate region experiences a transition from solid to liquid state during melting and solid to the liquid state during solidification. Hence, the thermal conductivity of the substrate region is set to k_m. In the present study, the density and specific heat of the powder materials is assumed to be the same as the solid or the liquid state of the material. This assumption was previously adopted by Jamshidinia et al. [17].

The powder particles have higher heat absorptivity than the metal phase for AlSi10Mg alloy. An experimentally measured value by Aversa et al. [4] is used for the absorptivity of the powder phase. Hagen-Ruben relationship [55] is used to measure absorptivity of the metal phase in the solid or liquid state and is as follows:

$$\alpha = \begin{Bmatrix} 0.6; \text{powder state} \\ 365.15\left(\frac{\beta_r}{\lambda}\right)^{0.5}; \text{ liquid or solid state} \end{Bmatrix} \quad (2.15)$$

where β_r is the resistivity of the metals, and λ is the wavelength of the laser source. β_r can be expressed as:

$$\beta_r = \begin{Bmatrix} (-1 + 0.0125T) \times 10^{-8} \ ; \text{solid state} \\ (10.7 + 0.0145T) \times 10^{-8} \ ; \ \text{liquid state} \end{Bmatrix} \quad (2.16)$$

In the present study, the weight fraction of titanium diboride (TiB_2) nanoparticles is very low (0.0009%). Therefore, its effects on the composite material's property are assumed negligible. Temperature dependent thermo-physical properties for AlSi10Mg alloy are used in this model [56] and shown in Table 2.1. In addition, the thermophysical properties used for titanium diboride [57] are given in table 2.2.

In this model, the dynamic viscosity μ of the liquid metal is calculated by [8]:

$$\mu = \frac{16\sigma}{15}\sqrt{\frac{m}{k_B}} \quad (2.17)$$

where m is the atomic mass, k_B is the Boltzmann constant, and σ is the surface tension of AlSi10Mg alloy. The surface tension for liquid metal can be expressed as:

$$\sigma = [868 - 0.152(T - T_L)] \times 10^{-3}; T \geq T_L \quad (2.18)$$

Table 2.1. Thermophysical properties of AlSi10Mg.

Properties, symbols, and units	Values	Conditions
Solidus temperature, T_S (K)	830.15	
Liquidus temperatutre, T_L (K)	870.15	
Thermal Conductivity, k_m (W m^{-1} K^{-1})	2.29e-7T^3- 4.45e-4T^2 + 0.231T + 128.26	$T \leq T_S$
	−2.08T + 1866.56	$T_S \leq T \leq T_L$
	0.0195T + 44.21	$T \geq T_L$
Heat Capacity C_p (J kg^{-1} K^{-1})	0.459T + 744.75	$T \leq T_S$
	1.6T− 202.24	$T_S \leq T \leq T_L$
	−8.32e-3T + 1196.93	$T \geq T_L$
Density ρ (kg m^{-3})	2670	
Thermal expansion coefficient β (K^{-1})	2.39×10^{-5}	
Temperature coefficient of the surface tension $\frac{\partial\sigma}{\partial T}$ (N m^{-1} K^{-1})	-0.152×10^{-3}	
Emissivity (ε)	0.3	

Table 2.2. Thermophysical properties of TiB_2

Properties, symbols, and units	Values
Density ρ_{np} (kg m^{-3})	4520
Thermal Conductivity k_{np} (W m^{-1} K^{-1})	25
Specific heat $C_{p,np}$ (J kg^{-1} K^{-1})	$976 + 0.21(T-273) - 426\exp(-0.008(T-273))$

Marangoni Convection and Natural Convection

Surface tension force is dependent on the temperature of the gas-liquid interface, also commonly referred to as the free surface. As shown in Fig. 2.2, a localized high temperature region is generated by the laser heat source at the center of the melt pool surface during selective laser melting. Thus a high temperature gradient is created from the center to the edge of the molten pool.

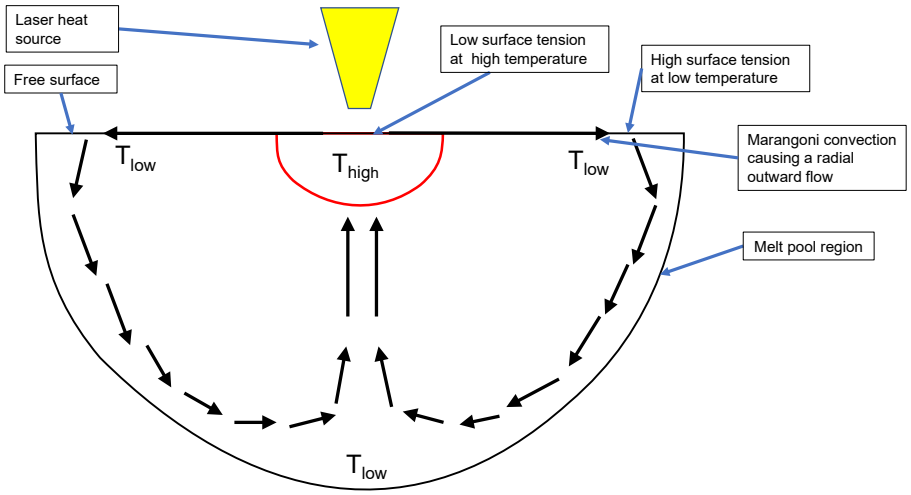


Figure 2.2. Schematic diagram of Marangoni convection creating a radial outward flow from the center of the molten pool.

The temperature gradient creates a gradient surface tension force at the free surface. Molten metal flows from low surface tension to higher surface tension region, yielding convection within the melt pool region. This phenomenon, known as Marangoni convection, drives the liquid metal flow

during the SLM process. The intensity of Marangoni convection can be quantified by dimensionless Marangoni Number [58] and is expressed by the following equation:

$$\mathrm{Ma} = -\frac{\partial\sigma}{\partial \mathrm{T}}\frac{\mathrm{w}\Delta \mathrm{T}}{\mu\alpha_t} \tag{2.19}$$

where, μ is dynamic viscosity, α_t is the thermal diffusivity of the liquid metal. w is the characteristic length of the melt, ΔT is the temperature difference between the maximum temperature and the solidus temperature of the alloy and $\frac{\partial\sigma}{\partial T}$ is the surface tension coefficient of the metal. Pure metal with a negative surface tension coefficient has radially outward flow from the melt pool center, while a positive surface tension coefficient yields radially inward flow from the melt pool edge to the melt pool center [59]. Surface tension is also dependent on the alloy compositions at the free surface. Due to the presence of the compositional gradient, the Marangoni convection pattern takes a complex shape for different alloys [59,60]. For AlSi10Mg alloy, the surface tension coefficient is negative [56]. Hence a radially outward flow from the center of the melt pool is created, which is similar to the flow pattern shown in Fig 2.2. However, the flow pattern can reverse if the surface tension changes due to a compositional gradient. However, no analytical relation of surface tension gradient of AlSi10mg alloy due to compositional gradient was found in the literature [56]. So, the effect of compositional gradient on the surface tension of AlSi10Mg is neglected in the present study.

Moreover, temperature gradient within the melt pool region can generate natural convection of liquid metal. The density is a temperature-dependent property that increases at lower temperatures and decreases at higher temperatures. Fluid with relatively lower density moves upward, while fluid with higher density moves downwards due to buoyancy. High temperature is generated at the top of the molten pool region, while the temperature is relatively low at the melt

pool bottom. For this reason, a radially outward flow is generated from the melt pool center to its edge. For AlSi10Mg, the surface tension coefficient is negative. As a result, both the Marangoni and natural convection induce a similar flow pattern, intensifying liquid metal convection from the melt pool center towards its edge at the solid-liquid interface.

Enthalpy-Porosity Technique

The solidification process has been modeled using the enthalpy-porosity approach. This technique calculates the liquid fraction at each iteration by satisfying the enthalpy balance. The liquid fraction is the percentage of a cell's volume in the liquid state. The phase transition from liquid to solid or solid to liquid for metals differs based on their composition. The phase transition for pure metal occurs instantaneously once the melting or the solidification temperature is reached. However, phase change happens in various temperature bands for metal alloys. Ramachandra et al. [61] and Gadgil et al. [62] concluded that deformed grids with precise heat flow conditions at the solid-liquid interface were required to track the moving liquid-solid interface. Therefore it was extremely difficult to solve this problem computationally using the deformed grid method [62]**.** The enthalpy formation is an alternate and more practical approach, which can be employed in a fixed grid size. The enthalpy-porosity approach represents the solid-liquid phase change interface as a pseudo porous medium. This porous medium is also defined as the mushy state in this method. The porosity of the mushy state begins to decrease when solidification occurs. When a cell reaches complete solidification, the porosity is set to zero, and the fluid movement is restricted. A source term, $\overrightarrow{F_{Mushy}}$, is added to the momentum equation in Eq. 2.2 to account for the flow resistance with the change in porosity. This term is defined as:

$$\overrightarrow{F_{Mushy}} = \frac{(1-\beta_L)^2}{(\beta_L^3+\varepsilon_S)} A_{mushy}\,\vec{u} \tag{2.20}$$

where, β_L is the liquid fraction, ε_S is a small computational constant (0.001) to avoid division by zero, and A_{mushy} is the Mushy zone constant. The term $\frac{(1-\beta_L)^2}{(\beta_L^3+\varepsilon_S)}$, is also known as the porosity function [63]. The mushy zone constant usually ranges from 10^4 to 10^7. Brent et al. [63] and Pal et al. [64] tested the sensitivity of the results between 10^5 to 10^7. The authors did not find any significant differences in the outcomes. In the SLM process, Marangoni convection-driven melt pool flow velocity is very high (2 m/s - 5 m/s) [21]. Thereby, to completely suppress the flow in the solid phase, a mushy zone constant value greater than 10^7 is required [65]. However, very high values can cause the numerical results to oscillate [53]. Therefore, a mushy zone constant value of 10^8 is selected for this study to achieve a satisfactory numerical solution. The sum of sensible enthalpy (h_s) and latent heat content (ΔH) is the material's enthalpy H_E, which is stated as:

$$H_E = h_s + \Delta H \tag{2.21}$$

$$h_s = h_{s,ref} + \int_{T_{ref}}^{T} C_p\, dT \tag{2.22}$$

Here, the reference enthalpy and temperature are $h_{s,ref,}$ and T_{ref}, respectively. The specific heat at constant pressure is denoted by C_p. The latent heat content can alternatively be expressed in terms of liquid fraction and latent heat of fusion. For solid, since the liquid fraction (β_L) is zero, latent heat (ΔH) becomes zero. On the other hand, the latent heat varies for liquids depending on the specific latent heat of fusion (L_H) of material.

$$\Delta H = \beta_L L_H \tag{2.23}$$

The relationship between liquid fraction, solidus, and liquidus temperature [66] is expressed as:

$$\begin{aligned} \beta_L &= 0; \quad \text{if } T < T_S \\ \beta_L &= 1; \quad \text{if } T > T_L \\ \beta_L &= \frac{T - T_S}{T_L - Ts}; \quad \text{if } T_S < T < T_L \end{aligned} \tag{2.24}$$

where T_S and T_L are the solidus and liquids temperature of the material.

Euler-Lagrangian Approach

The Euler-Lagrangian method with one-way coupling is utilized to track the particles. In this study, the weight fraction of the nanoparticles in the liquid metal is very low (0.0009%). As a result, the effects of particle suspension are neglected in the Eulerian framework. In addition, in the Eulerian framework, fluid parameters such as pressure, temperature, and velocity as a function of space and time are solved in a set of fixed coordinates in the flow field. The velocity distribution of the fluid is used to calculate the acceleration of individual particles from the particle motion equation, which is expressed in equation 2.25. Finally, the particle transport model predicted the trajectory, velocity, and location of individual particles in the Lagrangian reference frame by integrating the force balance equation.

Particle Motion Equations

Equation of Force Balance

The concept of Newton's second law of motion is used in the particle force balancing equation, which states that the sum of all forces acting on a particle is proportional to the

acceleration of the particle. The particle force balance equation determines particle motion in a Lagrangian frame. Forces such as drag force, gravitational force, virtual mass force, pressure gradient force, Brownian force, and lift forces have been taken into account in the particle transport model. These forces are summed up for per unit mass of an individual particle to calculate the acceleration of the particle.

$$\frac{du_p}{dt} = F_D(\vec{u} - \overrightarrow{u_p}) + \frac{\vec{g}(\rho_p - \rho)}{\rho_p} + \overrightarrow{F_V} + \overrightarrow{F_P} + \overrightarrow{F_B} + \overrightarrow{F_S} \quad (2.25)$$

where,

$F_D(\vec{u} - \overrightarrow{u_p}) = \text{Drag force}$

$\overrightarrow{F_V} = \text{Virtual mass force}$

$\overrightarrow{F_P} = \text{Pressure gradient force}$

$\overrightarrow{F_B} = \text{ Brownian force}$

$\overrightarrow{F_S} = \text{ Saffman's lift force}$

The forces demonstrated in the equation are incorporated into the computation depending on their function relating to the size and mass of the particles and flow conditions. These forces are explained in the following sections.

Drag Force

Inertia forces are negligible compared to viscous forces operating on them for submicron particles. As a result, Stokes' drag law is used in this work to account for the drag force [67]. Stokes assumed that the fluid present on the surface of individual spherical particles had no relative velocity. Nevertheless, as the size of the submicron particle approached close to the mean free path of the fluid, this assumption became invalid. The average distance traveled by fluid molecules

between collisions is defined as the mean free path of the fluid (λ_f). Cunningham slip correction is incorporated into Stokes' drag law to account for the slip on the particle surface [68]. The drag force on a spherical particle can be represented as:

$$F_D = \frac{18\mu}{d_p^2 \rho_p C_C} \tag{2.26}$$

where, C_C is the Cunningham correction factor and is given by:

$$C_c = 1 + \frac{2\lambda_f}{d_P}\left(1.257 + 0.4e^{-1}\left(\frac{1.1\, d_P}{2\lambda_f}\right)\right) \tag{2.27}$$

Virtual Mass and Pressure Gradient Force

When a particle moves through a fluid, the movement of the surrounding fluid creates additional mass around the particles. The additional force required to accelerate the particle is defined as the virtual mass force. When the particle density is substantially higher than the fluid density ($\rho \ll \rho_P$), the virtual mass force is minimal. The virtual mass flow becomes significant when particle density is much lower than the fluid density ($\rho > \rho_P$) and, therefore, is included in the particle force balance equation. The equation for virtual mass force is as follows:

$$\overrightarrow{F_v} = \frac{1}{2}\frac{\rho}{\rho_p}\frac{d}{dt}\left(\vec{u} - \overrightarrow{u_p}\right) \tag{2.28}$$

Variation of the pressure gradient surrounding the particle creates an additional force, defined as the pressure gradient force. The following equation describes this as:

$$\overrightarrow{F_P} = \frac{\rho}{\rho_p}\overrightarrow{u_p}\frac{\partial \vec{u}}{\partial x} \tag{2.29}$$

Saffman's Lift Force

Because of the presence of the shear field between particles and fluid flow, particles experience a lift force. Saffman's lift force is defined as the force that is perpendicular to the direction of the flow. The equation for Lift force [69] is presented by:

$$\overrightarrow{F_s} = \frac{2Kv^{\frac{1}{4}}\rho d_{ij}}{\rho_P d_P \left(d_{ij} d_{kl}\right)^{\frac{1}{4}} \left(\vec{v} - \overrightarrow{v_p}\right)} \tag{2.30}$$

where d_{ij}, d_{jk}, and d_{kl} are the deformation tensors, and K is a constant value of 2.594.

Brownian Motion

Brownian motion is a significant force acting on the submicron particles submerged in a fluid. The random force experienced by the particles results from the collision with the rapidly moving atoms of the fluid is defined as the Brownian force. Classical mechanics cannot predict the distance a particle travels per unit time due to the massive quantity of collisions it undergoes in a single second. Therefore, it is assumed as a random force. The amplitudes of the Brownian force components acting on a particle [70] are defined as follows:

$$F_{B_i} = m_p \zeta_i \sqrt{\frac{\pi S_0}{\Delta t}} \tag{2.31}$$

Where, ζ_i are independent Gaussian random numbers with zero means and unit variance. Δt is the size of time step in seconds, and S_0 is the spectral intensity which can be defined as

$$S_0 = \frac{216 v k_B T}{\pi^2 \rho d_P^5 \left(\frac{\rho_P}{\rho}\right) C_C} \tag{2.32}$$

where, ν is the kinematic viscosity, k_B is the Boltzmann constant and T is the temperature of the fluid.

Solidification Morphology of Melt Pool

The solidification microstructure of metallic materials is dependent on thermal gradient (G) and solidification rate (R) at the solid-liquid interface [59]. A combination of high thermal gradient and/or low solidification rate leads to planar growth of the solidification front, as presented in Fig. 2.3. Cellular and dendritic grains can form when the solidification rate is very high at a specific thermal gradient. The product of G and R is defined as the cooling rate ($\dot{T}$), which controls the scale of the microstructure of the resolidified region [23,59]. During selective laser melting of metal alloys, the cooling rate of the liquid in the front of the solidification boundary is very high. For this reason, SLM is also called the rapid solidification process [29]. A higher cooling rate generates finer microstructures, whereas a lower cooling rate produces coarse grains, as demonstrated in Fig. 2.3. Generally, the solidification morphology for SLM of metal alloys lies

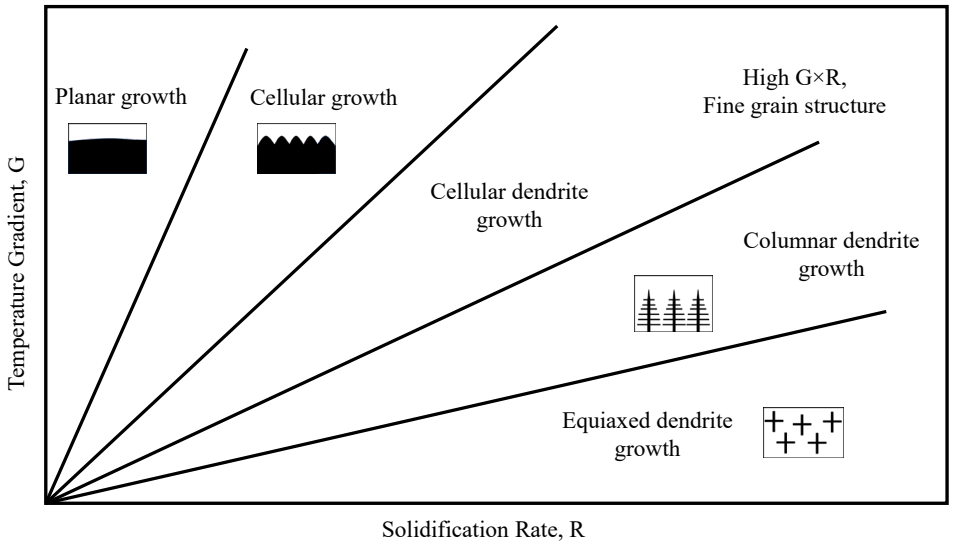


Figure 2.3. Effect of thermal gradient (G) and solidification rate (R) on solidification morphology.

in the dendritic region. A low thermal gradient and high solidification rate generate fine equiaxed dendrites, usually observed at the top of the melt pool region, as shown in Fig. 2.4. However, columnar dendritic grains dominate the solidification morphology at the bottom and interior of the melt pool region because of a higher thermal gradient than the top [37].

Nucleation And Grain Growth In SLM

During selective laser melting of metal alloys, solidification phenomena can be characterized by epitaxial growth, nucleation, and competitive growth. A schematic diagram demonstrating grain nucleation and growth mechanism is shown in Figure 2.4. Partially melted grains can form new grains in the solidified region without changing their crystallographic orientation. This phenomenon is identified as epitaxial growth [14,37]. Nucleation is an important

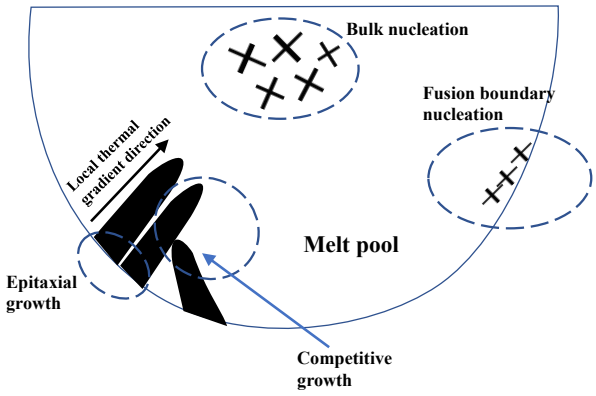


Figure 2.4. Illustration of various solidification phenomena, i.e., epitaxial growth, competitive growth, and nucleation.

aspect during the solidification of the melt pool, which can happen homogeneously or heterogeneously. When the liquid metal temperature falls below the liquidus temperature, it is identified as the undercooled liquid. A new nucleus formed in the undercooled liquid metal can only survive beyond a critical undercooling temperature. Then survived nucleus can form a new

grain provided that a sufficient amount of undercooled liquid surrounds the nucleus. Two types of nucleation can occur during the solidification process:

- Bulk nucleation: If nucleation occurs at the interior of the melt pool region where liquid metals are present in a bulk amount [9,10,12,23].
- Fusion boundary nucleation: If nucleation occurs with the region close to the melt pool boundary [37].

Competitive grain growth shapes the texture of the resolidified grains. From the previous section, it is known that usually, dendritic grains are generated in SLM of metals. Metals that have a cubic unit cell lattice structure (Face Centered Cube (FCC) or Body Centered Cube (BCC) are called cubic metals [43]. For these metals, primary dendrites grow parallel to the ⟨100⟩ directions along its crystallographic orientation [71], as shown in Fig. 2.5. ⟨100⟩ is the miller indices representing the family of three orthogonal axes. During the rapid solidification process, if the

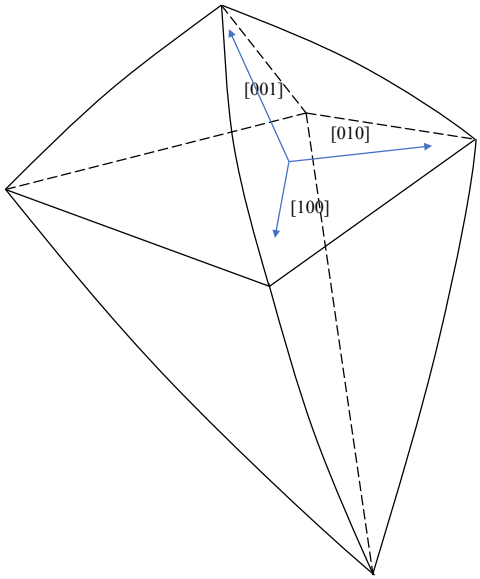


Figure 2.5. Grain formed for a cubic metal in non-uniform temperature conditions.

local thermal gradient is aligned with one of these directions, that becomes the preferential growth direction for cubic metals [43]. The angle between the direction of the local thermal gradient and primary dendrite is defined as the misorientation angle (θ).To keep up with the speed of solidification front v_s, primary dendrite's velocity, v_d should be:

$$v_d = \frac{v_s}{\cos(\theta)} \tag{2.33}$$

Therefore, the dendritic grains with the smallest misorientation angle are favored to grow over grains with a larger misorientation angle if both have the same velocity (v_d). This phenomenon is known as competitive growth. During solidification from the melt pool, a combination of competitive and epitaxial growth and nucleation probability in the interior of the melt pool dictate the texture and formation of grains.

CHAPTER THREE

NUMERICAL METHOD OF THE CFD MODEL

Introduction

In the finite volume method, the computational domain is divided into several grids, and each node is surrounded by a small volume known as the control volume. The fluxes in a control volume are balanced using the conservation law. The summation of fluxes entering the control volume is regarded the same as the summation of fluxes exiting the neighboring volume. Finite volume approach discretizes the partial differential equation into an algebraic equation using the divergence theorem. The volume integral of a partial differential equation with a divergence term is converted to a surface integral, resulting in a discrete equation that states the conservation law on the control volume. At each control volume, the surface integral terms are then evaluated as flux.

The mass, momentum, and energy conservation equations can be rewritten in a more generalized form:

$$\frac{\partial}{\partial x}(\rho\phi) + \nabla \cdot (\rho\phi\vec{v}) = \nabla \cdot \left(\Gamma_\phi \nabla\phi\right) + S_\phi \tag{3.1}$$

where ϕ is a general variable for scalar quantity, Γ_ϕ is the coefficient of diffusion, and S_ϕ is the scalar quantity's source term. The integral form of Equation 3.1 based on control volume (V) can be expressed in terms of transient, advection, diffusion, and source terms:

$$\underbrace{\int_{V} \frac{\partial \rho \phi}{\partial t}}_{Transient} + \underbrace{\oint \rho \phi \vec{v} \cdot d\vec{A}}_{Advection} = \underbrace{\oint \Gamma_{\phi} \overrightarrow{\nabla \phi} \cdot d\vec{A}}_{Diffusion} + \underbrace{\int_{V} S_{\phi}\, dV}_{Source} \tag{3.2}$$

where, diffusion and advection terms are defined as an integral of surface area vector, $\vec{A}$, velocity vector, $\vec{v}$ and scalar variable, ϕ, and its gradient, $\overrightarrow{\nabla \phi}$.

A two-dimensional control volume is depicted in Fig. 3.1 to illustrate the finite volume discretization. There are two cell centers, C_o and C_1. The letter, f stands for the face centroid, which is defined as the point where two neighboring cells meet. Additionally, $\overrightarrow{r_0}$ and $\overrightarrow{r_1}$ are position vectors directed from the cell centroids C_o and C_1, respectively to the face centroid.

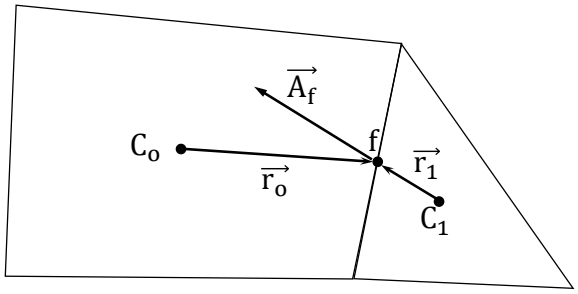


Figure 3.1. Illustration of control volume discretizing

In the computational domain, Eq 3.2 applies to every single control volume or cell. On a given cell, the discretization of this equation can be stated as follows:

$$\frac{\partial \rho \phi}{\partial t} V + \sum_{f}^{N_{faces}} \rho_f \overrightarrow{v_f} \phi_f \overrightarrow{A_f} = \sum_{f}^{N_{faces}} \Gamma_{\phi} \nabla \phi_f \overrightarrow{A_f} + S_{\phi} V \tag{3.3}$$

The discretized scalar transport equation comprises of unknown scalar variable ϕ at the center of its own and as well as the neighboring cells. As a result, a linearized version of the

discretized scalar transport equation is required. The linearized coefficients of ϕ are a_p and a_{nb}, where a_p is for the current cell and a_{nb} is the neighboring cell. This equation can be expressed as follows:

$$a_p\phi = \sum_{nb} a_{nb}\phi_{nb} + b \tag{3.4}$$

Discretization

Discretization of Transient Terms

The transient derivative of a scalar variable ϕ was discretized and evaluated using a backward difference scheme. The first and second order transient discretization equations are as follows:

$$\frac{\partial\phi}{\partial t} = \frac{\phi^{n+1} - \phi^{n}}{\Delta t} \tag{3.5}$$

$$\frac{\partial\phi}{\partial t} = \frac{3\phi^{n+1} - 4\phi^{n} + \phi^{n-1}}{2\Delta t} \tag{3.6}$$

The governing equation was discretized in terms of space and time using the finite volume method for transient simulation. Equations 3.5 and 3.6 are discretized in terms of time step Δt. Temporal discretization integrates all the terms of the differential equations over this time step Δt. The current, previous, and future time steps are denoted by the superscripts n, n-1, and n+1.

Discretization of Advection and Diffusion Terms

Several discretization methods can be used to interpolate the face value from the solution of a one-dimensional advection-diffusion equation. The QUICK scheme has been employed in the current numerical model. This method is based on a weighted average of second order upwind and

central interpolation schemes and can operate on the quadrilateral or hexahedral meshes. To illustrate the interpolation scheme, one dimensional control volume consisting of cells P, W, and E is shown in Fig. 3.2. This method is based on a weighted average of second order upwind and central interpolation schemes. Convected variable ϕ_e can be computed by the following expression n Fig 3.2.:

$$\phi_e = \theta\left[\frac{S_d}{S_c + S_d}\,\phi_P + \frac{S_c}{S_c + S_d}\,\phi_E\right] + (1 - \theta)\left[\frac{S_u + 2S_c}{S_u + S_c}\,\phi_P - \frac{S_c}{S_c + S_u}\,\phi_W\right] \qquad (3.7)$$

where, θ is the weighted average. S_c, S_d, S_u are the lengths of cells P, W, and E, respectively. The values of the scalar variable of cells P, W, and E are ϕ_P , ϕ_W , ϕ_E. These parameters are illustrated in Fig. 3.2. This interpolation method follows an upward scheme, which means the scalar quantities are collected from upstream cells relative to the direction of the normal velocity vector v_n. Face values of desired variables are identical to upstream cell values in a convection-dominated flow.

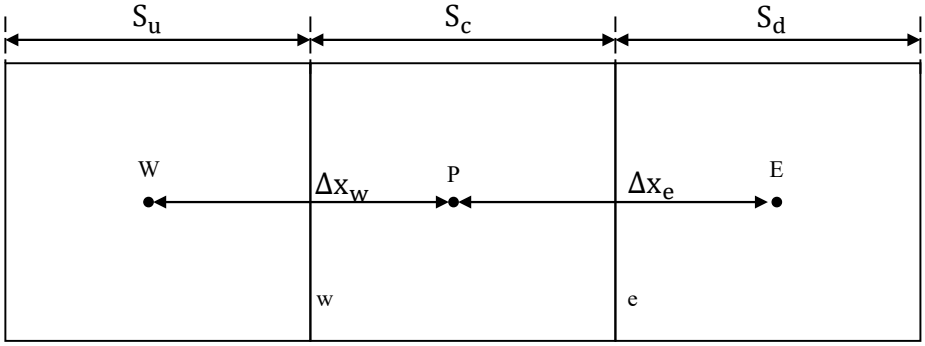


Figure 3.2. Schematic of control volume discretization for quadrilateral or hexahedral meshes

Discretization of Continuity and Momentum Equations

The linear form of the discretized scalar transport equation was used to discretize continuity and momentum equations. Considering force vector ($\vec{F}$), Stress tensor ($\bar{\bar{\tau}}$), and identity matrix (I), the integrated version of the continuity and momentum equations at steady state are shown in Eqs. 3.8 and 3.9.

Continuity equation:
$$\oint \rho\vec{v} \cdot d\vec{A} = 0 \tag{3.8}$$

Momentum equation:
$$\oint \rho\vec{v}\vec{v} \cdot d\vec{A} = -\oint pI \cdot d\vec{A} + \int_V \vec{F}\, dV + \oint \bar{\bar{\tau}} \cdot d\vec{A} \tag{3.9}$$

Pressure (P_{c_0}, P_{c_1}) and velocities ($\overrightarrow{v_{C_0}}$, $\overrightarrow{v_{C_1}}$) between two adjacent cells C_0 and C_1 can be used to provide a simplified form of mass flux through the face f between two adjacent cells C_0 and C_1. Cells C_0 and C_1 and face f are shown in Fig. 3.1.

$$J_f = \hat{J}_f + d_f\left(P_{C_0} - P_{C_1}\right) \tag{3.10}$$

where, J_f is the mass flux through face f. $\hat{J}_f$ can be expressed as:

$$\hat{J}_f = \left(\rho_f \frac{a_{p,C_0}\overrightarrow{v_{C_0}} + a_{p,C_1}\overrightarrow{v_{C_1}}}{a_{p,C_0} + a_{p,C_1}}\right).\hat{n} + J_{HOT} \tag{3.11}$$

Where, d_f is the function of average of the linerarized coefficient a_p for cells C_0 and C_1, expressed in Eq. 3.4. P_{C_0} and P_{C_1} and pressures of cells C_0 and C_1, while $\overrightarrow{v_{C_0}}$ and $\overrightarrow{v_{C_1}}$ are velocities of cells C_0 and C_1 respectively. J_{HOT} is the high order correction term for non-orthogonal meshes.

J_f can be written as a linearized form of the scalar transport equation.

$$J_f = \rho_f \frac{a_{p,C_0}\overrightarrow{v_{C_0}} + a_{p,C_1}\overrightarrow{v_{C_1}}}{a_{p,C_0} + a_{p,C_1}} + d_f\left(\left(P_{C_0} + (\nabla P)_{C_0} \cdot \overrightarrow{r_0}\right) - \left(P_{c_1} + (\nabla P)_{C_1} \cdot \overrightarrow{r_1}\right)\right) \tag{3.12}$$

The face and cell center values of velocity $\vec{v}$ are linked using the momentum weighted average method [72]. This method is useful for avoiding unrealistic pressure values induced by linear interpolation.

The following simplified discretized equation is obtained by integrating the continuity equation with respect to the control volume.

$$\sum_{f}^{N_{faCes}} J_f A_f = 0 \tag{3.13}$$

The linearized form of the continuity equation does not explicitly calculate the pressure. The Navier-Stokes equation cannot be discretized without solving the pressure field. Likewise, the momentum equation cannot be solved for unknown pressure distribution. Pressure correction techniques are commonly employed in an iterative procedure to ensure that the velocity field satisfies the continuity equation by adjusting the pressure field at each iteration. As a result, mass flux through face f, denoted by J_f, must be expressed as:

$$J_f = \hat{J}_f^* + d_f(P_{C_0}^* - P_{C_1}^*) + d_f(P_{C_0}' - P_{C_1}') \tag{3.14}$$

Or, in a simplified form:

$$J_f = J_f^* + J_f' \tag{3.15}$$

J_f^* represents the mass heat flux (J_f) across face f, which corresponds to the assumed pressure field (P*). J_f' is a mass heat flux correction technique that is linked with the cell pressure correction values (P_{C_0}' and P_{C_1}').

This pressure correction scheme formulates a discretized equation for the pressure correlation p′ which is given by:

$$a_p p' = \sum a_{nb} p'_{nb} + b \tag{3.16}$$

where the source term b is the net flow rate into the cell and can be expressed as:

$$b = \sum_{f}^{N_{faces}} J_f^* A_f \tag{3.17}$$

The momentum equation was discretized by replacing the scalar quantity with the velocity vector components. The velocity field is obtained by solving this equation. The pressure values between the cell centers vary smoothly. Therefore, a standard scheme was integrated into the momentum coefficient equation to determine the pressure values at different faces by interpolation [72] and is shown in Eq. 3.18

x momentum equation: $$a_p u = \sum_{nb} a_{nb} u_{nb} + \sum p_f A \cdot \hat{i} + S \tag{3.18}$$

where,

$$P_f = \frac{\frac{P_{C_0}}{a_{p,C_0}} + \frac{P_{C_1}}{a_{p,C_1}}}{\frac{1}{a_{p,C_0}} + \frac{1}{a_{p,C_1}}} \tag{3.19}$$

Pressure based Segregated Algorithm

All the governing equations are solved in terms of solution variables using a pressure-based segregation method. The coefficients of discretized continuity and momentum equations are solved simultaneously in the pressure-based coupled algorithm [73]. Figure 3.3 shows the pressure-based segregated solving workflow used in the current numerical model. Once a set of

solutions is found, the procedure is repeated until convergence occurs within each time step. While solving for the solution variables at each iteration, user defined functions were added. For example, as shown in Fig. 3.3, user-defined momentum sources were added to the discretized momentum equation while solving for velocity components by momentum conservation. In addition, user defined properties were added at the end of each iteration to update the material properties. The computational time for the pressure-based coupled algorithm is very high, despite offering low accuracy in the solution. Segregated algorithm solves each variable separately and updates the value of the solution variables after convergence. Segregated algorithms reduce computing time while maintaining high accuracy. Therefore, the current investigation included a pressure-based segregation algorithm. At first, the components of the velocity are computed. The momentum equations were solved using updated pressure and face mass flux values. The pressure correction equation was solved using the updated velocity field and mass flow numbers. Using the calculated variables from the pressure correction equation, the face mass fluxes, pressure, and velocity field values were adjusted. Finally, the energy and source terms were solved, considering user defined source term for laser heat. After finding the temperatures, the material properties are updated. The user defined properties of materials are taken into account during this stage. Then the overall solution's convergence was computed for that iteration step. When the solution meets the convergence criterion for that time, the solution advances to next time step. Otherwise, it continue to update the characteristics of the solution variable and repeat the processes in the next iteation until the convergence conditions are met. Even though the solution convergence was slow due to continuous iteration of the linked non-linear governing equation, the convergence of the solution was achieved. At each iteration, the normalized rate of convergence was checked. The

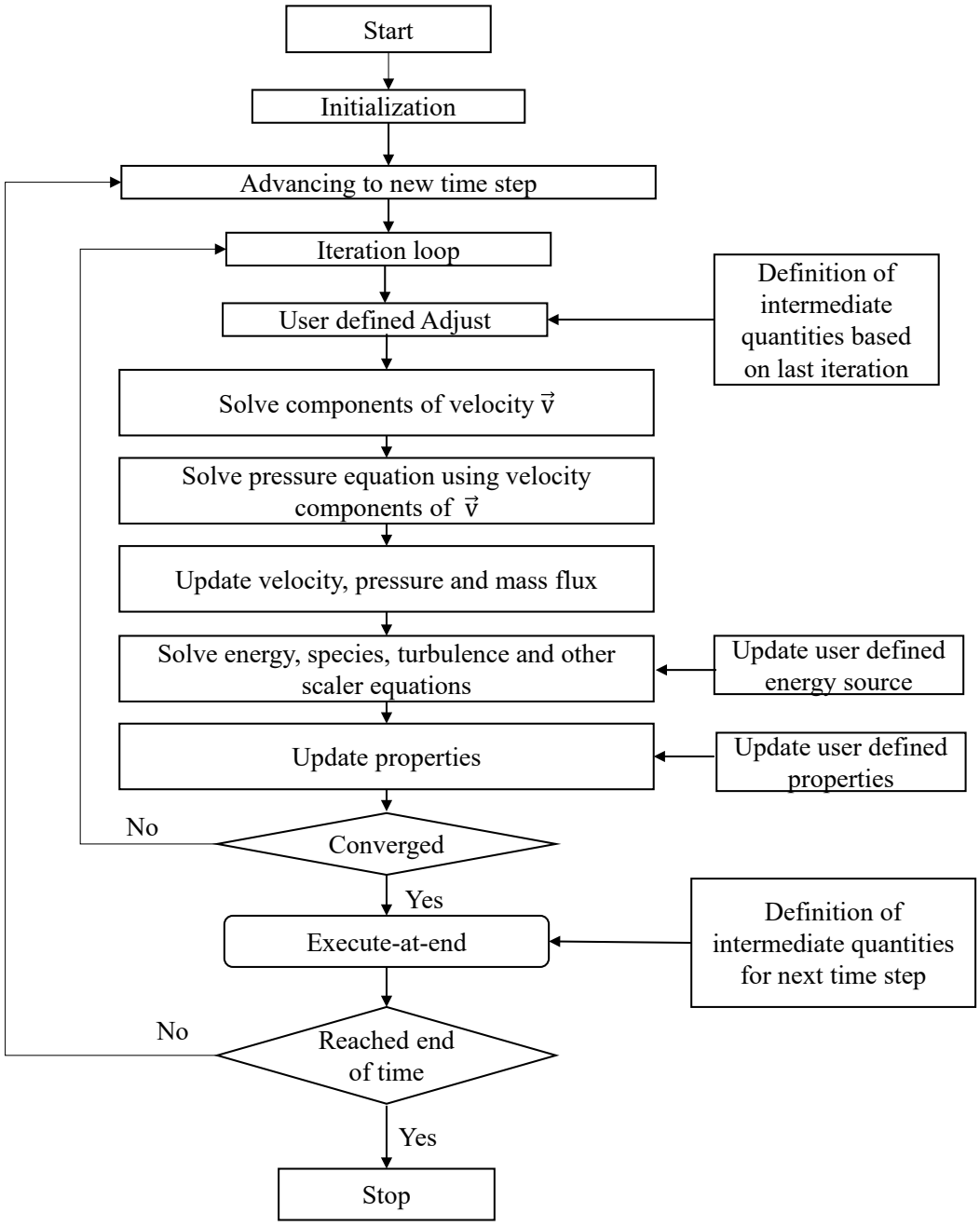


Figure 3.3. Overview of the pressure-based segregated algorithm.

convergence monitor was set to a value of 10^{-6}. If the normalized rate of change of all process variables was less than or equal to the value of the convergence monitor, the solution was termed converged. For a scalar quantity ϕ, the normalized convergence monitor may be stated as:

$$\text{Convergence Monitor} = \sum_{i=1}^{n_{cells}} \frac{\left|\phi_i^k - \phi_i^{k-1}\right|}{\left|\phi_i^k\right|} \tag{3.22}$$

The sum of the results calculated between the current (k) iteration and the previous iteration (k-1), divided by the sum of the current iteration's results, is used by the convergence monitor (k). This absolute value computation was done for all cells, n_{cells}. The solver continues these processes at each time step until the preset time has been reached.

Grid Independence Test

Grid independence tests were performed to select a grid size that produced accurate results at an optimum computational time. These tests were carried out to find the minimum number of cells in the grid that could generate numerical results that have a negligible difference from the numerical results produced at a higher number of cells. The computational time increases with the increase in the number of cells. Therefore, choosing the smallest grid size that produces accurate numerical results increases computational time and resources efficiency. In the current CFD model, the mesh was denser near the symmetric wall and the top wall. This was done to produce accurate results for the heat and fluid flow in the molten pool. Six different grids were studied in terms of the maximum temperature and the maximum velocity generated at the top wall. Fig. 3.4 shows the maximum temperature and velocity resulting from the different numbers of cells in the

mesh. The parameters selected for this study were 180 W laser power, 300 mm/s scanning speed, and the radius of the laser was 50 µm. The laser heat source was modeled with a volumetric heat

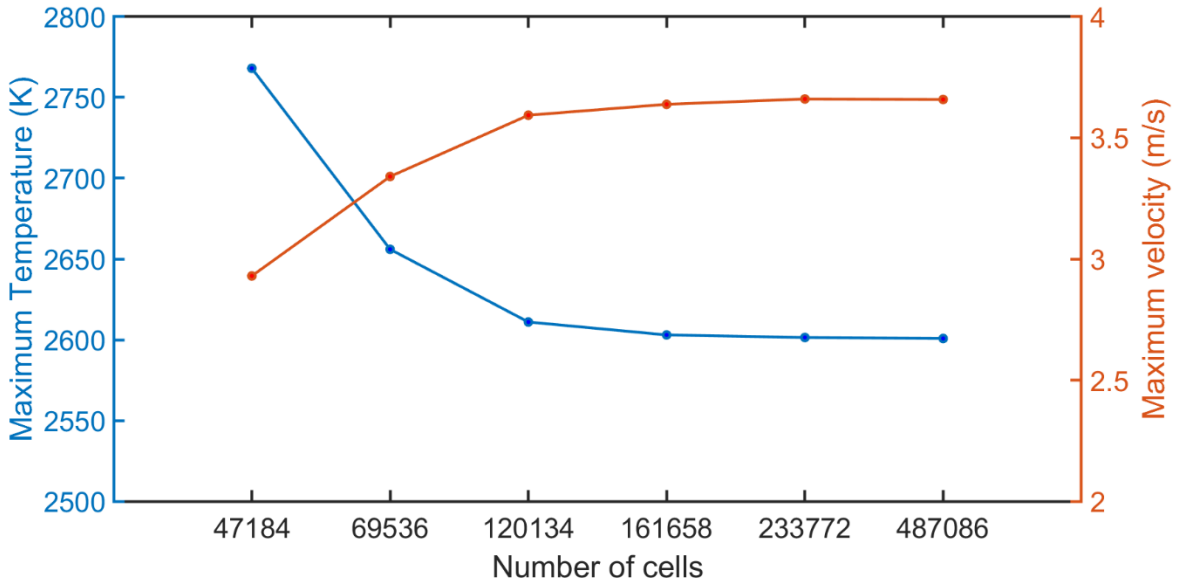


Figure 3.4. Grid independence test of the numerical model.

source using Eq. 2.5. Heat losses on the walls were formulated using Eq. 2.6. In addition, Eqs. (2.10- 2.11) was used to add Marangoni shear stress on the top wall. The initial temperature was set to 373 K for this case study. The symmetric boundary condition was added to increase computational efficiency. The numerical results were calculated at 1750 µs on the top wall. From Fig. 3.4, a small difference in maximum temperature and velocities was observed at the last three mesh sizes consisting of 161658, 233772, and 487086 cells, respectively. in. The difference in maximum temperature was less than 0.1 % among those meshes. The difference in maximum velocity was less than 0.1 % between the last two meshes. Therefore, the mesh with 233772 cells was selected for the numerical study in the present research. Fig. 3.5 depicts the computational mesh where it is observed that the mesh is denser near the symmetric wall and the top wall. In

addition, the mesh is denser in the powder bed and the laser scan track region to provide more accurate numerical results of heat and fluid flow.

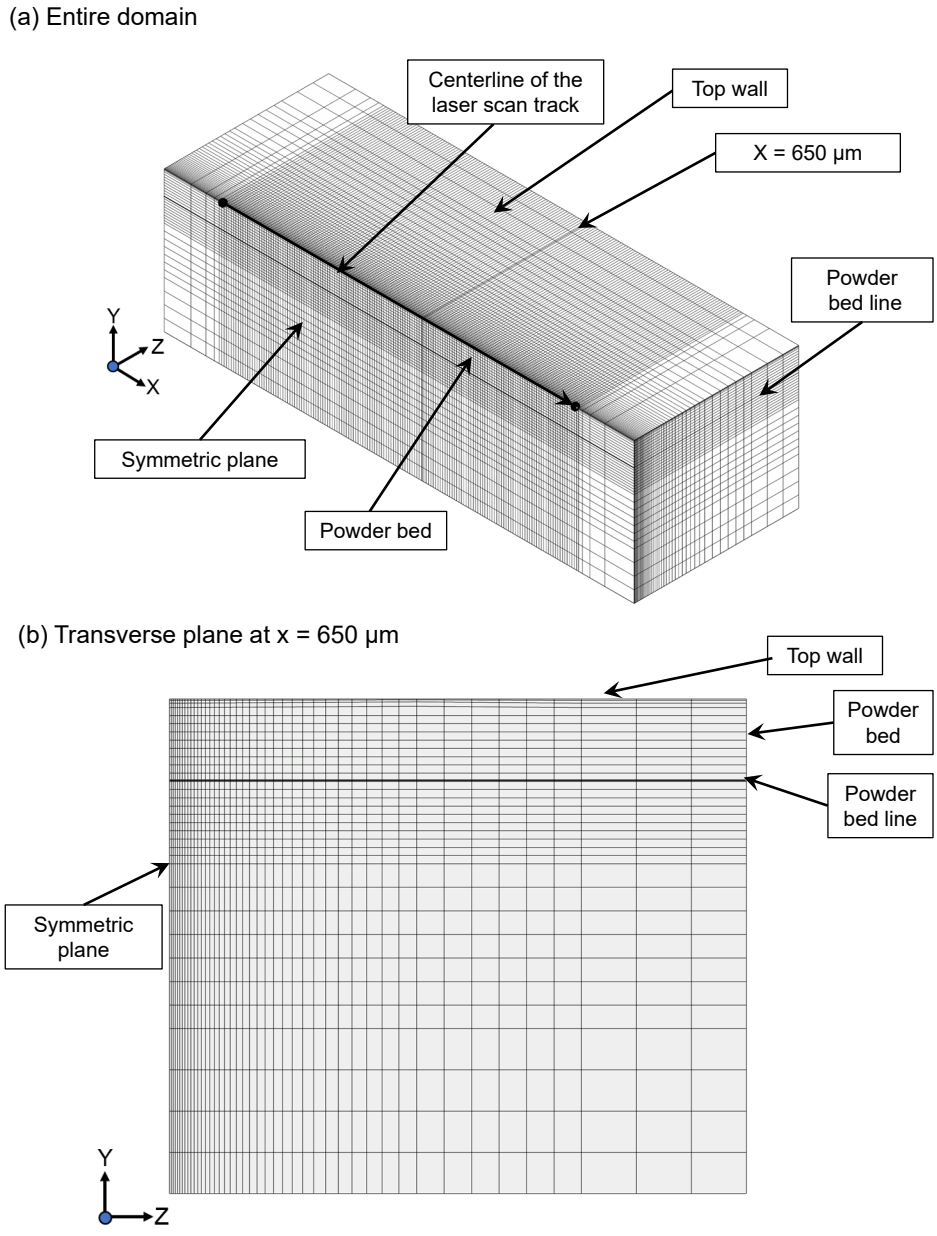


Figure 3.5. Computational mesh at: (a) entire domain, (b) transverse plane at x = 650 µm.

.

Code Validation

The present study involved both the computational fluid dynamics (CFD) modeling of the selective laser melting (SLM) process and the particle transport model. Thereby, it was imperative to validate both of these models to gain confidence in collaborating the nanoparticle transport model in the CFD model of the SLM process. The current CFD model was validated by comparing it with the experimental and numerical results published in the literature. The melt pool geometry computed from the present model during selective laser melting of AlSi10Mg alloy was validated with experimental data from Aversa et al. [4]. However, the particle transport model was not included in this comparative study. The particle transport model was separately validated by the numerical results of Bagheri et al. [74] to determine the feasibility of the particle transport algorithm in ANSYS FLUENT. Details of the validation process are explained in the following sections.

Validation of The Melt Pool eometry

Aversa et al. [4] experimentally measured the melt pool geometry for AlSi10Mg alloy for various laser power and laser scanning speeds. Their investigation was performed on a single scan track to analyze the effects of laser process parameters for a single solidified layer. The authors measured the melt pool geometry in terms of the width and depth of the melted region in the substrate. The melted region in the substrate can be referred to as the molten substrate. Therefore, the present CFD model for SLM was compared with the width and depth of the molten substrate, experimentally measured by Aversa et al. [4].

Aversa et al. [4] used AlSi10Mg alloy powders with a mean diameter of 30 μm in the powder bed and the same material in bulk form for the solid substrate. The powder bed height was

50 μm, and the powder bed was preheated to 100 °C before being subjected to laser melting. The authors selected several different combinations of laser power and laser scanning speed in their study. For validation purposes, the simulated melt pool geometry was compared for two different cases :

1. Varying laser powder from 100 W to 195 W, with a constant laser scan speed at 300 mm/s.
2. Varying laser scan speed from 300 mm/s to 1200 mm/s, with a constant laser power of 180W.

In the current CFD model, the laser heat source was modeled with a volumetric heat source using Eq. 2.5. Heat losses on the walls were formulated using Eq. 2.6. The temperature of the ambient was set to 300K. In addition, Eqs. (2.10- 2.11) was used to add Marangoni shear stress on the top wall. The initial temperature was set to 373 K for this case study. The thermophysical properties of aluminum alloy were taken from Table 2.1 for this validation study. The melt pool geometry was calculated from the temperature history for the current CFD model. Due to rapid melting and solidification in the selective laser melting process, the melt pool geometry at a specific cross-section changes very rapidly. In order to find the regions which experienced melting, the maximum temperature distribution at the transverse (y-z) plane at x = 650 um was tracked from the temperature history. The maximum temperature profile for 180 W laser power and 300 mm/s scanning speed is presented in Fig. 3.6 (a). As symmetry was considered in the model, results were computed and shown in half of the total domain. In Fig. 3.6 (a), the isotherm of the liquidus temperature line is represented by a black curve, marking the boundary of the final melt pool. The regions above the liquidus isotherm line have experienced melting during the SLM process and

represent the final melt pool geometry. Figure 3.6 (b) presents the entire melt pool regions in red color. The molten substrate region below the powder bed line is also shown in Fig 3.6 (b). This exact figure is placed beside the published experimental micrograph image [4] at a cross-section of the solidified layer in Fig. 3.7 for visual comparison. The figure further illustrates the computed width and depth of the molten substrate for both cases. The results of the shape of the molten substrate from the current CFD model were in good agreement, having a deviation less than 7% with the experimentally documented result. However, the shape of the melt pool at the powder bed region, computed by the current CFD model, does not match the experimentally obtained image of the melt pool. This is because molten pool surface deformation was not considered in the current model. Nevertheless, to focus on analyzing the transport of thermo-fluidic behavior with a simple and efficient model, the present model was subjected to further investigations. Several other researchers also adopted this comparison method to validate the SLM process model with experimental results in the literature [16,22,75].

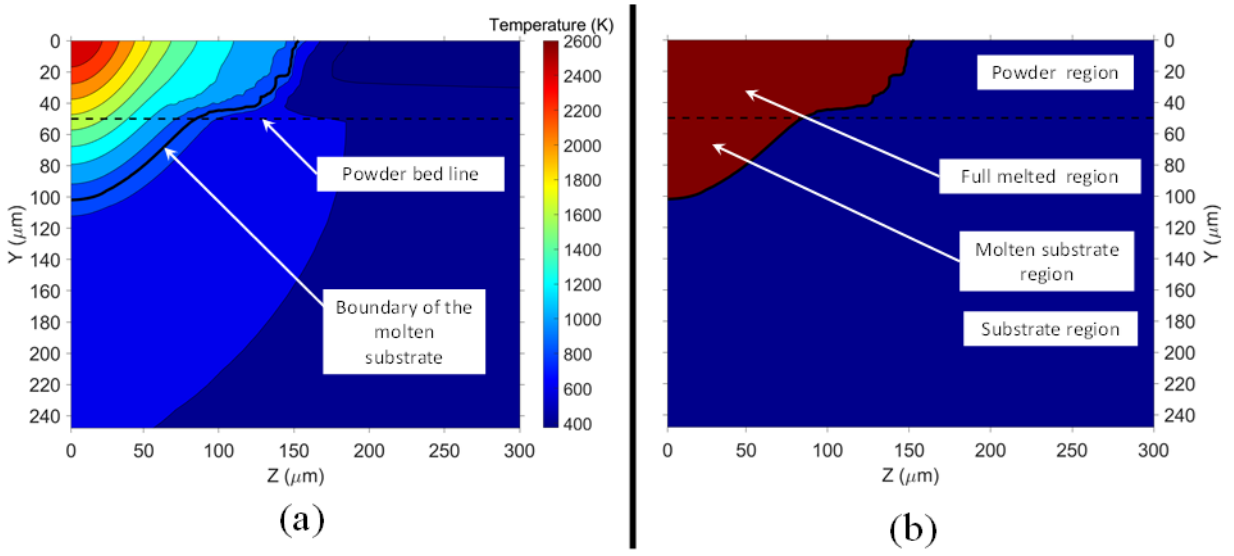


Figure 3.6. Illustration of forming melted zone at transverse (y-z) plane at x = 650 µm for 180W laser power and 300 mm/s scanning speed: (a) Maximum temperature profile (b) Final melted zone.

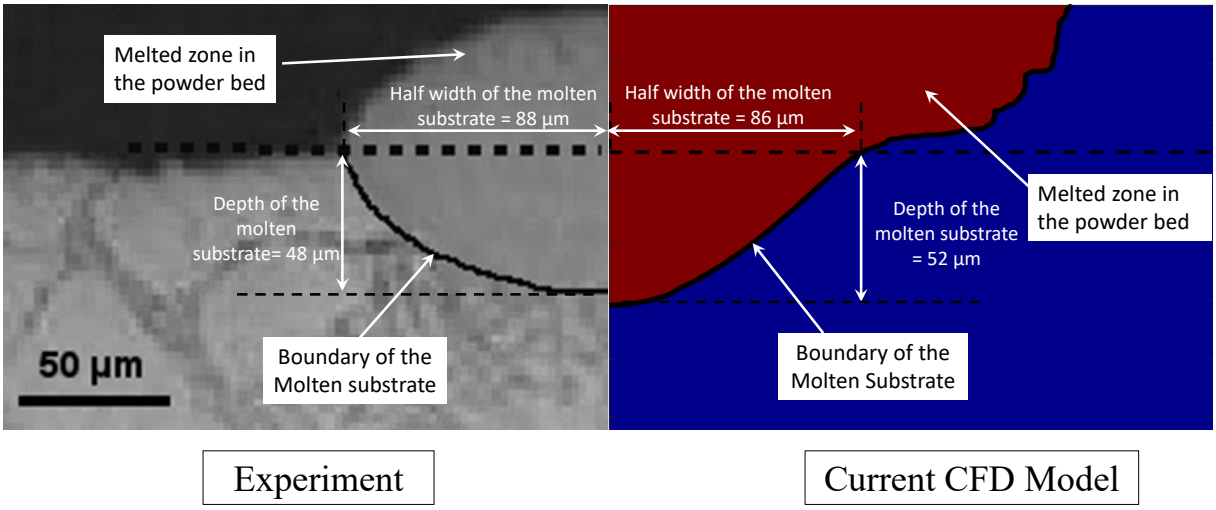
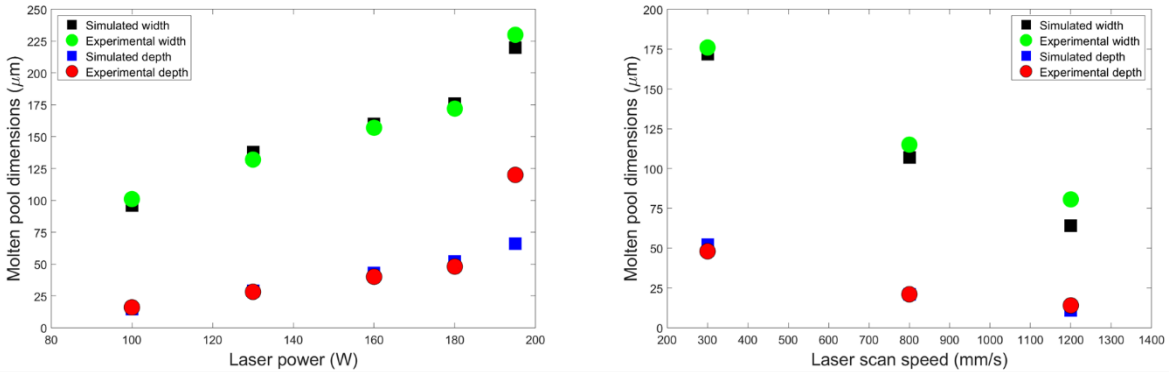


Figure 3.7. Comparison of the geometry of the molten substrate with published experimental data [4] for 180 W laser power and 300 mm/s laser scanning speed.

Figures 3.8 (a) and (b) demonstrate a quantitative comparison of the width and depth of the molten substrate between the present CFD model and the published data for the cases mentioned above. The half-width of the melt pool computed from the present model was multiplied by two to find the numerical width for these cases. The comparison indicated that the current model was in good agreement with the published experimental data when the power of the laser ranged from 100 W to 180 W at 300 mm/s scan speed. However, at laser power of 195W, a keyhole-type melt pool was generated during the experimental study by Aversa et al. [4]. This type of melt pool is observed when the surface temperature of the melt pool becomes higher than the boiling temperature of the metal [21]. As a result, some liquid metals evaporate and create a low-pressure region at the surface of the melt pool. A recoil pressure force is generated, which pushes down the molten metal from the gas-liquid interface and increases the molten pool depth. Recoil pressure and deformation of the gas-liquid interface were not considered in this CFD model. Hence, a



(a) (b)

Figure 3.8. Comparison of numerical and experimental results [4]: (a) for varying laser power from 100 W to 195 W at a laser scan speed of 300 mm/s, (b) for varying laser scan speed keeping laser power constant at 180 W.

significant deviation was observed in the measured depth of the molten substrate between the current CFD model and the published experimental result. The limitation of the present model is that it can measure melt pool geometries with reasonable accuracy when the surface temperature does not exceed the boiling temperature of the material. This type of melt pool geometry is known as conduction type melt pool [18,75]. The comparison of the shape of the molten substrate between the CFD model and the experimental work for varying laser scan speeds is shown in Fig. 3.8 (b). The result indicated that the CFD model computed molten substrate geometry deviated from experimental results at higher laser scanning speed. For laser scan speed of 1200 mm/s, deviation in width and depth were more than 10%. This is due to several assumptions and simplifications made in the model. In addition, melt pool geometry can become very unstable at higher scan speeds due to insufficient laser energy density [21]. Therefore, experimental data can be irregular. Based on the comparison with experimental results, the present CFD analysis of the selective laser melting of aluminum alloy is limited to process parameters that yield conduction-type melt pools

at low to moderate laser scan speeds. The selected process parameters for this study are mentioned in Chapter 5.

Validation of Particle Tracking Model

The present work was validated by comparing particle distribution results at a given time from the numerical study of solid particle tracking at high Rayleigh numbers by Bagheri et al. [74]. This has been done to build confidence on the particle tracking algorithm in ANSYS Fluent. In their study, the authors modeled a 2D rectangular air-filled enclosure with 5000 solid particles. The rectangular enclosure was differentially heated at the left and the right wall, and the horizontal walls were insulated. For a Rayleigh number of 10^5, the particle distribution after 50 seconds was compared with the present study as shown in Fig. 3.9. As can be seen from the figure, the results obtained from the current numerical model show good agreement.

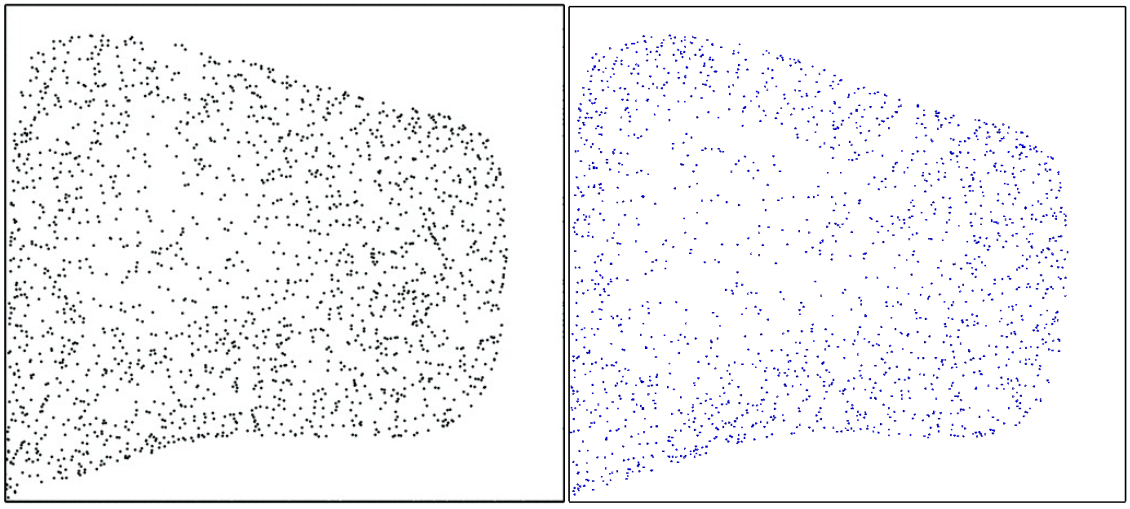


Figure 3.9. Comparison of numerically obtained particle distribution results: (a1) showing numerical results from Bagheri et al. [74] and (a2) showing results from the current numerical model.

CHAPTER FOUR

CELLULAR AUTOMATA SOLIDIFICATION MODEL

Introduction

Cellular Automata (CA) method describes the spatial and temporal evolution of a physical system by applying deterministic and probabilistic transformation rules [52]. The microstructure formation during solidification is simulated using a 2D Cellular Automata (CA) model following the approach described by Zhang et al. [11]. The computational domain of this 2D CA model is discretized into a finite amount of regular square elements called cells. Each cell is associated with several variables that describe the temperature (T), state (S), and crystallographic orientation (O) of the cell. Each variable holds numerical values to define the system completely. As shown in Fig. 4.1, four different states are defined for a cell to represent the condition of the material, i.e.

- S = 0: Liquid cell.
- S = 1: Interface liquid cell.
- S = 2: Interface solid cell.
- S = 3: Solid cell.

Orientation variable (O) represents the grain orientation of each cell. Grain orientation angle of the solidified grains is selected between (-45° to 45°) with respect to the y-axis. The range is distributed into 48 orientation classes to reduce the complexity of the problem [9]. For liquid cells, the value of the orientation variable is set to -50° to differentiate it from the solid cells. These grain orientation angles are stored in the orientation variable matrix (O) associated with all the cells in the CA domain. The grain orientation angle of a cell is described later in this chapter. CA

simulation is discretized into a finite amount of time steps, and at each time step, the values of the variables are updated depending on pre-defined transition rules. During the transition, the state and orientation of the current cells and the neighboring cells are considered. These transition rules are described in the next section. The Moore neighborhood is considered in this model, which contains nine nearest neighbors in 2D, including the cell itself, and shown in Fig 4.1.

Cell Transition rules

Cellular Automata (CA) model simulates the melting and solidification of metal by updating state and orientation variables at each time step. Initially, all the cells are in a solid state

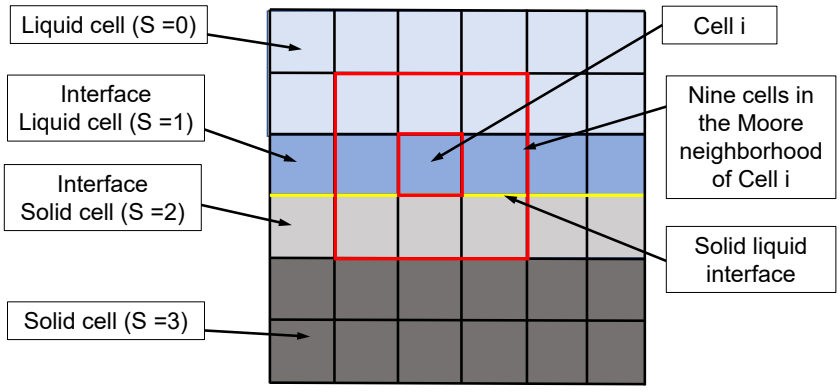


Figure 4.1. Schematic representation of a 2D CA domain with Moore neighborhood.

(S = 3). As the laser scans over the solid cells, some cells experience melting. If the temperature of the solid cell becomes higher than the liquidus temperature (T_L) at a specific time, then its cell state is updated to liquid, having a value of 0 or 1. The value of the melting cell depends on its neighborhood. If the melting cell has a solid cell (S = 2,3) in its neighborhood, then the cell is identified as the liquid interface cell (S = 1); otherwise, it is defined as the liquid cell (S = 0). The orientation of the melted cell is set to -50° to differentiate it from the solid cells. Conversely, at the

melt pool boundary, the solid cell (S = 3) having liquid cells (S = 0,1) in its neighborhood is transformed into a solid interface cell (S = 2).

During the solidification process, new grains are formed in the melt pool region. The grain growth process is modeled by the "modified decentered polygon" method following the "modified decentered square" approach by Zhang et al. [11]. The "modified decentered polygon" is described in the grain growth modeling section of this chapter. Using this method, the liquid interface cells are transformed into solid interface cells (S =1 → S = 2) provided that the cell temperature is lower than the liquidus temperature. The transition rules for melting and solidification are presented in Table 4.1, where T_i is the local temperature of cell i, T_L is the liquidus temperature, and S_{nb} represents the state of the neighbor cell.

Table 4.1. Transition rules for melting and solidification.

Process	Cell state before transition	Transition rule	Cell state after the transition
Melting	2,3	$T_i \geq T_L$ and all neighbors are liquid ($S_{nb} \leq 1$)	0
	2,3	$T_i \geq T_L$ and solid cells ($S_{nb} \geq 2$) exist in the neighborhood	1
	1	All cells in the neighborhood are liquid ($S_{nb} \leq 1$)	0
Solidification	0	At least one solid cell ($S_{nb} \geq 2$) exist in the neighborhood	1
	1	$T_i < T_L$ and cell captured by "modified decentred polygon"	2
	2	All cells in the neighborhood are solid ($S_{nb} \geq 2$)	3

Nucleation Modeling

In the present Cellular Automata model, grain nucleation phenomena were incorporated. During the solidification process, new grains can nucleate in undercooled liquid metal ahead of the solidification front, provided that the undercooling has reached a critical value. Undercooling refers to the liquid whose temperature has dropped below its solidification temperature but still has not solidified. As discussed earlier in Chapter 2, if the grain nucleation occurs in the presence of bulk amount of liquid, that is referred to as Bulk nucleation. The grain nucleation process is described by a Gaussian distribution function proposed by Gandin et al. [76]. The Gaussian distribution function indicates that grain nucleation density n continuously depends on the level of undercooling (ΔT), which is expressed in the following equation.

$$n(\Delta T) = \frac{N_{max}}{\Delta T_\sigma \sqrt{2\pi}} \int_0^{\Delta T} \exp\left(-\frac{(\Delta T - \Delta T_N)^2}{2(\Delta T_\sigma)^2}\right) d(\Delta T) \quad (4.1)$$

where N_{max} is the maximum nucleation density, ΔT_N is the mean undercooling, and ΔT_σ is the standard deviation. Gandin et al. [9] proposed a nucleation model that integrated this Gaussian distribution function. A similar approach was followed for bulk nucleation modeling in the current CA grain growth model. In this method, nucleating cells are randomly chosen, and the number of nucleating cells is calculated by the following equation:

$$N = N_{max,2D} \times C_y \times C_z \times \Delta x^2 \quad (4.2)$$

where, $N_{max,2D}$ maximum grain nucleation density in 2D. C_y and C_z are the number of cells along the y and z-direction of the simulation domain, and Δx is the length of the 2D square cell. $N_{max,2D}$ is related to the maximum grain nucleation density, N_{max} by Eq, 4.3, which is expressed as:

$$N_{max,2D} = \sqrt[3]{\frac{6}{\pi}} (N_{max})^{\frac{2}{3}} \quad (4.3)$$

N_{max} value is determined by experimental investigation, and for AlSi10Mg, this value is $10^5\ mm^{-3}$ [37]. For each selected bulk nucleating cell, a critical nucleation undercooling ΔT^{crit} value was specified to it using predefined Gaussian distribution parameters. The values for Gaussian distribution parameters are listed in Table 4.2. During simulation, at a time step, if the nominated cells are in an undercooled liquid zone, and its undercooling is greater than the associated ΔT^{crit} value, that cell became an active nucleus, and its state changes from liquid to interface solid cell (S =0,1 → S = 2). A random grain orientation was specified to the newly nucleated cell, and an imaginary polygon was attached to its center. The growth of nucleated cells and existing solid grains are discussed in the following section.

Table 4.2 Gaussian distribution parameter for AlSi10Mg [37].

Nucleation Parameters	Variable	Value
Maximum nucleation density (mm^{-3})	N_{max}	10^5
Mean undercooling (K)	ΔT_N	5
Standard deviation (K)	ΔT_σ	1

Grain Growth Modeling

Solidification of grains was modeled using the "modified decentered polygon" algorithm, following the "modified decentered square" approach by Zhang et al. [11]. Figure 4.2 illustrates the difference between these algorithms. In the "modified decentered square" method, grain growth was modeled using an imaginary square and assumed to have the same growth rate at all

four vertices. Nonetheless, the solidified grain's tendency to orient along the thermal gradient was not considered explicitly in that algorithm. Therefore, the grain growth simulation during solidification was prone to be inaccurate. A modified decentered polygon algorithm was used in the current Cellular Automata (CA) model to resolve this inaccuracy in the grain growth model. This method tracked all the vertices of the four-sided polygon which was used to model the grain growth. In addition, the difference between the direction of the crystallographic orientation of the grain and the local thermal gradient direction was taken into consideration. As a result, the half diagonal of the polygon, with a smaller angle with respect to the thermal gradient direction, favored growing over the other half diagonals of the polygon with larger angles. Therefore, the growth of the polygon was non-uniform, given that the temperature field during solidification was non-uniform. In Fig. 4.2, it is observed that, in the modified decentered square method, all the vertices have the same growth rate at time $t+\Delta t$, while in the modified decentered polygon method, the vertex along the direction of the thermal gradient has the highest growth rate. Modeling 2D grain growth with a non-uniform polygon or quadrilateral was adopted by several other researchers [43,77,78].

Aluminum forms a face-centered cubic (FCC) crystal structure after solidification. Grain growth begins at the melt pool boundary when the temperature of cell i, (T_i) drops below liquidus temperature (T_L). The solid cell at the interface (S = 2) is referred to as a growing cell, and a four-sided polygon is created centered on the cell, as shown in Figure 4.3. The primary dendritic arms of FCC metals have preferred growth directions along six equivalent ⟨100⟩ crystallographic orientations in 3D, which was shown earlier in Fig. 2.5. ⟨100⟩ is the miller indices representing the family of three orthogonal axes in 3D. However, as shown in Fig. 4.3, four mutually perpendicular

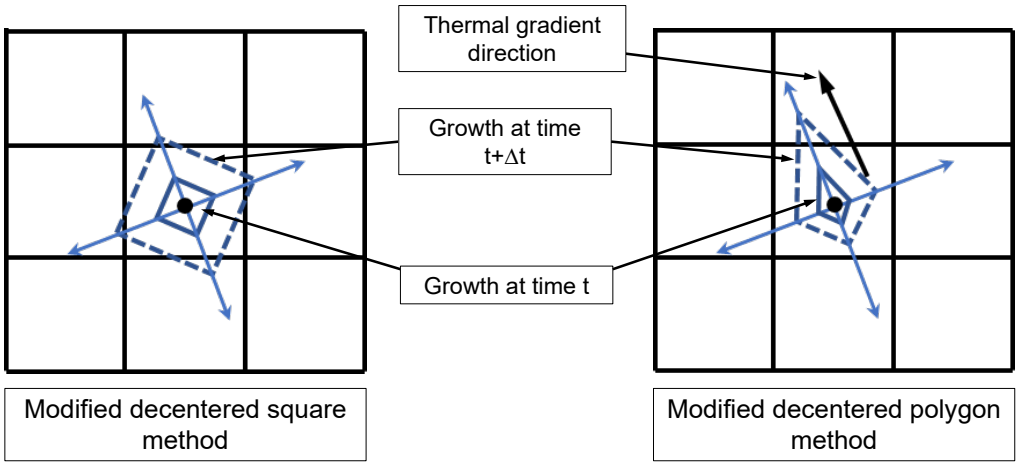


Figure 4.2. Schematic illustration of the modified decentered square and modified decentered polygon algorithm.

axes, ⟨10⟩ along its grain orientation, are chosen as the preferred growth directions in 2D. Here, ⟨10⟩ is the miller indices for the orthogonal axes in 2D. Primary dendrites grow along these axes, represented by the four half diagonals of the four-sided polygon. These half diagonals are shown in Fig. 4.3. The cells in the cellular automata (CA) domain have a global orientation angle and four local orientation angles, each 90° degrees apart from the other. For each of the half diagonals for a cell i, a local orientation angle $\theta_{i,j}$ is associated with it, calculated with respect to the y-axis. The subscript j ranges from 1 to 4. If any of the $\theta_{i,j}$ satisfies the condition expressed in Eq. 4.4 with the y-axis, that orientation angle is referred to as the global orientation angle, θ_i for cell i. This global orientation angle, θ_i is stored as a value for the orientation variable (O) associated with cell i. As discussed earlier, the values of the orientation variable (O) are the grain orientation angles of the solid cells. The half diagonals and the global and local orientation angles are depicted in the schematic diagram in Fig 4.3.

$$\theta_i = \theta_{i,j} \text{ ; if } (-45° \leq \theta_{i,j} \leq 45°) \text{ with respect to y-axis} \quad (4.4)$$

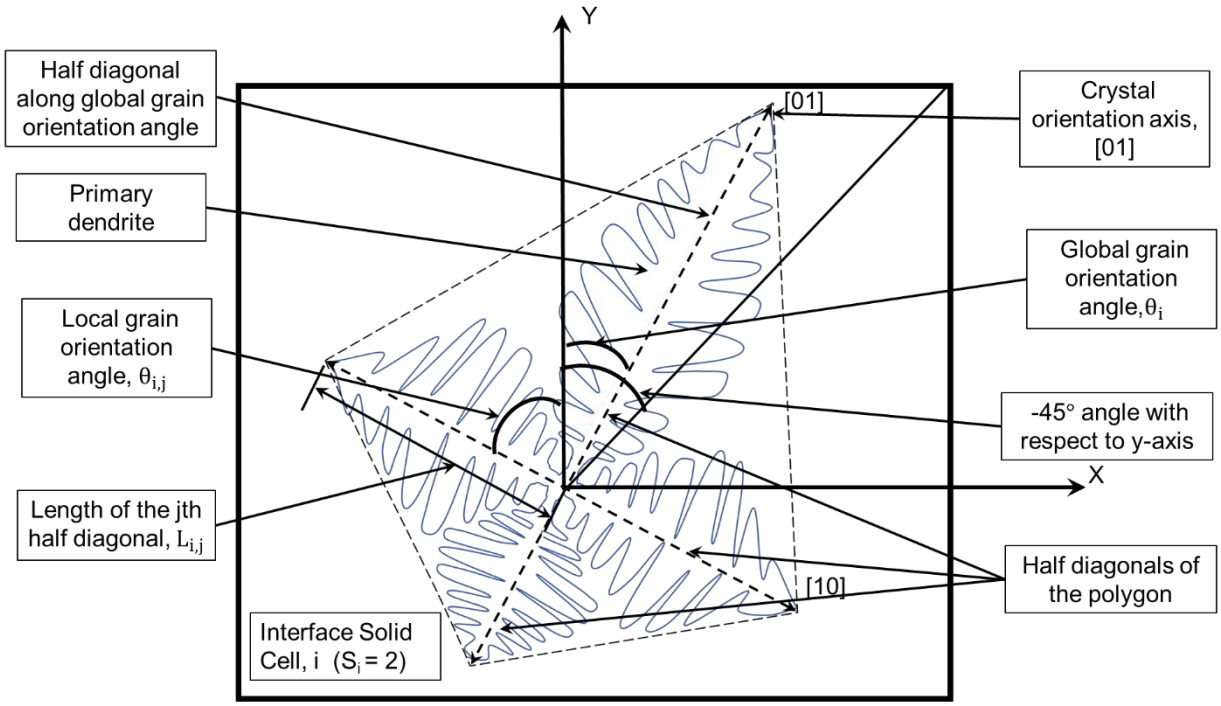


Figure 4.3. Schematic illustration of dendritic growth of a cubic metal represented in 2D CA domain.

The apexes of the polygon correspond to the tips of primary dendrites. The length of jth half diagonal for a cell i is represented as $L_{i,j}$. where the values of the subscript j range from 1 to 4. The length of the half diagonal is measured from the center to the tip of the polygon along the crystal orientation axis and is shown in Fig. 4.3. Its length increases with time step (Δt) by the following equation [11]:

$$L_{i,j} = \sum_t v_{i,j} \Delta t \text{ if } S_i = 2 \quad (4.5)$$

where ($v_{i,j}$) is the dendritic growth rate for jth half diagonal for cell i. Here, the subscript j ranges from 1 to 4. As a result, $v_{i,j}$ calculates the growth rate for each of the half diagonals individually.

The calculation for $v_{i,j}$ is conducted in two steps. Firstly, the velocity of the solidification front, v_{s_i} is calculated as a function of undercooling (ΔT_i) for all the half diagonals of cell i, using the KGT model [12] in the following equations:

$$v_{s_i} = a\Delta T_i^3 + b\Delta T_i^2 + c\Delta T_i \tag{4.6}$$

$$\Delta T_i = T_L - T_i \tag{4.7}$$

where, the value of the fitting coefficients are a = -8e-7; b = 2e-4 and c = 2.1e-3 [12]. According to the competitive grain growth mechanism, the solidification front tends to advance in the direction of the local thermal gradient. Therefore, the growing cell that has a primary dendrite directed along the local thermal gradient, the growing cell tends to grow in that direction. To integrate this aspect into this model, the grain growth velocity for each of the four half diagonals of cell i is expressed by [15]:

$$v_{i,j} = v_{s_i}\left[1 + \delta_k \cos\left[4\left(\theta_{t,i} - \theta_{i,j}\right)\right]\right] \tag{4.8}$$

where, $\theta_{t,i}$ is the angle between the direction of the projected local thermal gradient in 2D CA domain and the y-axis for cell i. $\theta_{i,j}$ is the grain orientation angle for the jth half diagonal of the interface solid cell i, and and δ_k is the anisotropic coefficient. As mentioned earlier, subscript j ranges from 1 to 4. This indicates that the growth velocities of all the four half diagonals are calculated individually in this model. A constant value of 0.3 is applied for the anisotropic coefficient δ_k [12].

The angle between the direction of the local thermal gradient and the y-axis, $\theta_{t,i}$ has been calculated from the projected direction of the local thermal gradient in the 2D CA domain and the y-axis (vertical axis) for any cell i. The vector field of the local thermal gradient has been calculated

from the CFD model and then interpolated into each of the cells in the CA domain. The following equation has been used to calculate $\theta_{t,i}$ associated with cell i:

$$\theta_{t,i} = \cos^{-1}\left(\frac{G_{y,i}}{\sqrt{G_{y,i}^2 + G_{z,i}^2}}\right) \tag{4.9}$$

where, the components of the thermal gradient vector in the y and z directions for cell i are $G_{y,i}$ and $G_{z,i}$ respectively. These calculations are performed using a MATLAB script. In Eq. 4.8, The term $\left(\theta_{t,i} - \theta_{i,j}\right)$ is equal to the misorientation angle, θ. As discussed earlier in the "Nucleation And Grain Growth In SLM" section of Chapter 2, misorientation angle refers to the angle between the direction of the local thermal gradient and local grain orientation. Grains with the smallest misorientation angle are favored to grow during solidification.

Cell Capture Mechanism

The four-sided polygon centered from the interface solid cell (S=2) grows during solidification. At an instant, when the apexes of the polygon are large enough to intersect with one of the neighbor cells, the cell capture mechanism takes place. This capturing method transforms the interface liquid cells into interface solid cells (S=1 → S=2). During this stage, the grain orientation information of the interface solid cell is transferred to the captured interface liquid cell. The evolution of grain is modeled during solidification by this process. A group of solid cells (S = 2,3), having the same orientation values, is defined as a grain in the CA domain. However, the global grain orientation values are different between the two grains. Therefore, the cell boundaries parting two grains are identified as grain boundaries in this model.

A schematic diagram is shown in Fig. 4.4 to illustrate the grain capture method. An interface solid cell a (S = 2), with a growing polygon, is shown in the figure. Global grain orientation angle of the cell is θ_a. Neighboring cells, b, c, and d are liquid at the interface (S = 1).

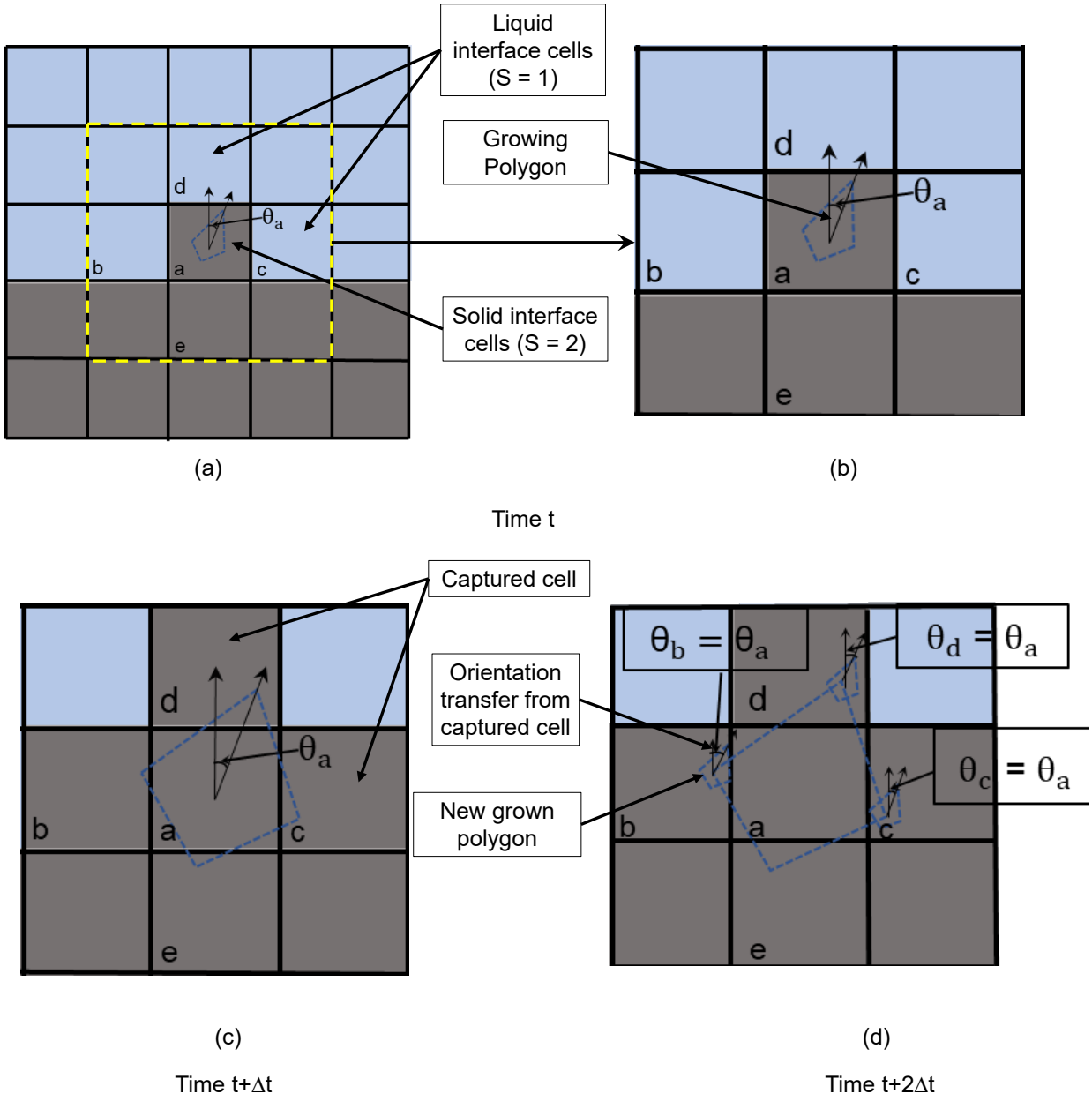


Figure 4.4. Schematic diagram of grain capture method by modified decentered polygon method.

With the increase of time, as the polygon grows, its apexes can intersect with the neighboring cells b, c, and d. These cells are captured by cell a, and their states are updated to interface solid cells ($S = 1 \rightarrow S = 2$). At the same time, the global grain orientation angle of the cell a is transmitted to those cells (θ_b, θ_c, $\theta_d = \theta_a$). These global orientation angles are stored as the values of the orientation variable (O) for cells b, c, and d. In the next time step, these cells start to grow their own polygons. The half diagonals of these polygons originate at the intersecting vertex from cell a, and they all have the same global orientation angle θ_a. Because of having the same orientation, these groups of cells are referred to as single grain in the current CA model. The tips of the new polygons capture more interface liquid cells, provided that the temperature of that cell is below the liquidus temperature, T_L. In case, two or more neighboring cells capture the same cell at a given time step, the local grain growth velocities of the capturing half diagonals are compared at that time instant. The cell with higher local grain growth velocity captures the interface liquid cell.

Coupling with CFD Model

The 2D microstructure model using the Cellular Automata (CA) method was one way coupled with the 3D computational fluid dynamics (CFD) model. As shown earlier, in Fig 2.1, two transverse (y-z) planes at x = 550 μm and x = 650 μm in the CFD domain were selected to study the grain evolution by the CA grain growth model. In the CFD model, the dimensions of those two transverse planes are 350×300 μm^2 with a plane of symmetry along its left side. However, the domain size selected for the CA model was 300×120 μm^2. The symmetry plane of the CFD model was mapped along the middle of this CA domain, as shown in Fig. 4.5. The CA model is both probabilistic and deterministic, which invalidates the assumption of symmetry for this simulation model. In the current CA model, the melting and solidification phenomena were

simulated using the predefined transition rules that were described in Table 4.1. According to these predefined rules, the values of the state (S) and orientation (O) variables of the cells in the CA domain were updated at each time step. Following the predefined rules during the simulation can be referred to as the deterministic approach of the current CA model. However, the bulk nucleation algorithm of the current CA model was probabilistic. The bulk nucleating cells were randomly selected in the CA domain. In addition, the grain orientation angles of the nucleated cells were randomly chosen between 48 orientation classes ranging from -45° to 45° with respect to the y-axis. The bulk nucleation mechanism was described earlier in the "Nucleation Modeling" section of this chapter. As a result, the current CA model simulates the microstructure following both probabilistic and deterministic methods.

As symmetry was not included in the CA model, the computed solution in CFD was mirrored at the plane of symmetry before integrating into the CA model. Figure 4.5 further depicts that the CA model does not encompass the entire region in the transverse planes of the CFD model. From the literature, it was found that the molten pool's size usually ranged from a few tens to a hundred micrometers in the selective laser melting process [6]. The current CA model was focused on simulating the regrowth of grains in the melted region only. Hence, selecting a smaller dimension, including the entire melt pool area and a small part of the surrounding the unmelted powder bed and substrate region, was a reasonable and computationally efficient approach [11,12,14]. In the current CFD model, the cells were in 3D, and their sizes were non-uniform along the transverse plane, which were shown in Fig. 3.5. However, the cells in the CA domain were 2D squares with a uniform size of $1 \times 1\ \mu m^2$. Therefore, the cell center values of the 3D cells that coincided with the transverse planes were linearly interpolated into the CA domain using

MATLAB's linear interpolation scheme [79]. Several other researchers also took this approach to couple the 3D CFD model with a 2D CA model [12,15,77].

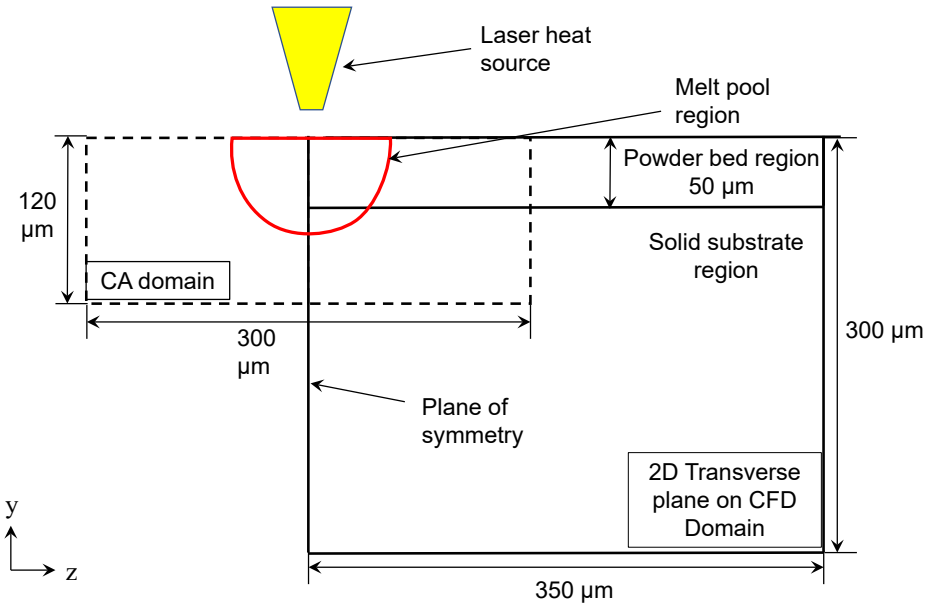


Figure 4.5. Schematic illustration of CA computational domain and its relation with the transverse plane of the CFD simulation domain.

The nanoparticles' positions computed by the particle transport model in CFD were three-dimensionally distributed within each cell. The transverse (y-z) planes at x = 550 µm and 650 µm were located along the cell centers of the cells they had coincided with. The cells were uniformly 5 µm thick in the x-direction. All the nanoparticles bounded by the CFD cells along those transverse planes were considered in the 2D CA domain. While extracting nanoparticles positions from those cells, their x coordinates were neglected. The y and z coordinates of the nanoparticle positions of the solidified regions computed in CFD are mirrored at the symmetric plane and mapped in the CA domain. While coupling the CFD model computed nanoparticle distribution into the CA domain, only the final positions of nanoparticles in the resolidified region were considered. It was assumed that the velocity of the nanoparticle was negligible when the

solidification occurred. The 2D square cells in the CA domain within which the positions of the nanoparticles are mapped are selected as viable cells for bulk nucleation. As described earlier in the chapter, following the bulk nucleation mechanism, when the cell reaches a critical undercooling temperature associated with it, it can nucleate new grains in the CA domain.

The workflow of coupling these two models is illustrated in Fig 4.6. At first, the 2D CA simulation domain is initialized with solid powder and substrate cells with random orientations.

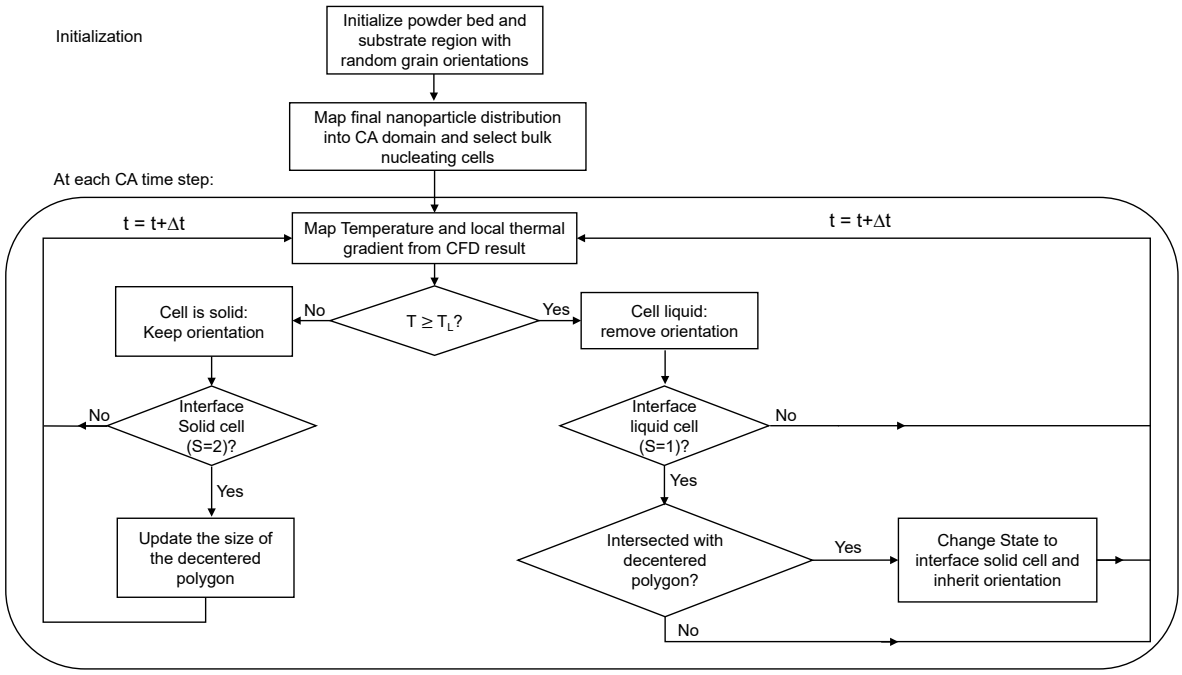


Figure 4.6. Diagram showing the workflow of CA grain growth model coupled with a CFD model.

Then, the positions of the nanoparticles are mapped into the CA domain and selected as potential cells for nucleation. Afterward, the temperature and the local thermal gradient field computed with the CFD model are imported into the CA model at each time step. The same time step size of 0.5 μs is chosen for CFD and CA models. The states of the CA cells are updated at the new time step

following the transition rules described in Table 4.1. The velocities of the solid interface cells (S = 2) are calculated based on interpolated temperature distribution and thermal gradient field. During the CA simulation, the decentered polygon associated with the growing solid interface cell (S=2) may intersect with a neighboring liquid interface cell (S=1). In that case, the neighboring cell solidifies with the inherited orientation of the growing cell. This process is referred to as the cell capture mechanism which is described earlier in this chapter. The simulation goes to the next time step after that with the latest grain orientations, where all these processes are repeated until the molten pool fully solidifies.

Simulation Parameters

Proper selection of simulation parameters is essential for the numerical stability of the grain growth simulation by Cellular Automata (CA) model [12]. Therefore, simulation parameters, such as time step size Δt, cell size Δx, and initial CA domain were carefully chosen in this numerical model. However, due to the probabilistic aspect of the CA method, the same result can not be reproduced even for the same exact case. Therefore, the conventional approach to studying the numerical method's stability by varying grid and time step size is not applicable for this Cellular Automata method. Hence, the simulation parameters were selected based on published data on the CA model and experimental observation.

The length (Δx) of the 2D square cells in the Cellular Automata domain was set to 1 μm based on the size of the secondary dendritic arm spacing of the aluminum alloy powder [78]. Tang et al. [80] experimentally calculated the secondary dendritic arm spacing of AlSi10Mg alloy powders around 1-1.5 μm. The powder materials in the powder bed region in the current study had a constant diameter of 20 μm. Thereby, selecting a cell size of 1 μm to simulate the grain growth

of aluminum alloy was a reasonable approach. Several researchers applied the same cell size for the CA domain to simulate grain growth for aluminum alloy [12]. The time step size was selected as such that it satisfied the following criteria [37], expressed in Eq. 4.10:

$$\Delta t \leq 0.25 \frac{\Delta x}{\max (v_{i,j})} \tag{4.10}$$

where, Δx is the cell size and $v_{i,j}$ is the growth velocity of the jth dendrite of cell i. This criterion ensures that the half diagonals, $L_{i,j,}$ do not exceed more than a quarter of the cell's size during a single time step. The right-hand side of Eq. 4.10 can measure the Courant–Friedrichs–Lewy (CFL) number for the CA model with a stability coefficient of 0.25. The CFL number can be used to evaluate the time step required for the stability of this transient CA simulation for a given cell size and maximum grain growth velocity. From Eq. 4.6, it is observed that the grain growth velocity is dependent on the amount of undercooling. The difference between liquidus and solidus temperature of aluminum alloy was set to 40 K in the CFD model. Since CFD and CA domains were coupled, a cell in the CA domain had a maximum of 40 K undercooling before it solidified. This amount of undercooling results in a maximum value that can be selected for the time step size Δt is around 0.8 μs if the cell size is 1 μm according to Eq. 4.10. In the present study, a constant time step size of 0.5 μs was selected for numerical stability.

Initial grain structure is also an important aspect that controls grain growth. Therefore, it is imperative to have an initial grain structure consistent with experimentally published data to have a satisfactory result. The smallest grain size of aluminum alloy powders is around 1 μm [80], while the grain size of bulk aluminum alloy in the substrate region is around 10 μm [81]. So, the CA model is initialized with a randomly oriented grain structure with an average grain size of 10

μm in the substrate region and 1 μm in the powder bed region. The initial grain structure selected for this study is shown in Fig. 4.7. Since the selection of cell size, time step size, and initial grain structure was consistent with published data, the model can provide a reliable prediction of grain evolution during solidification. The validation of this CA model considering these simulation parameters is explained in the next section.

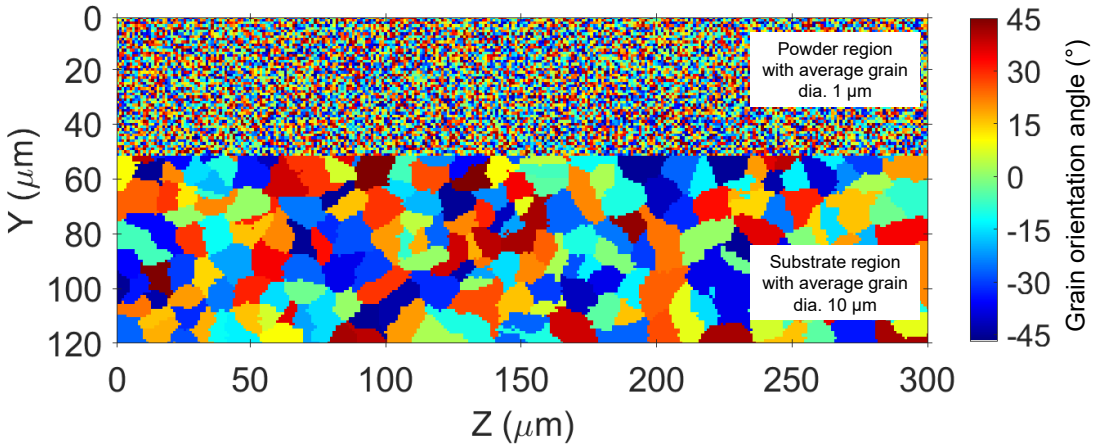


Figure 4.7. Initial grain structure for CA grain growth model.

Validation of Cellular Automata Microstructure Model

The Cellular Automata (CA) microstructure model must be validated with published results before employing it to analyze microstructure formation during the selective laser melting (SLM) process. Therefore, the present CA grain growth model was validated by comparing it with both numerical and experimental results documented in the literature. The competitive grain growth algorithm implemented in the present CA model was validated against a numerical grain growth model documented by Rai et al. [82]. In addition, average grain diameter can be measured from the resulting grain structure predicted by the current CA model. Hence, the average grain size computed from the present microstructure model was validated with experimental data published

by Baumard et al. [83]. The numerical and experimental validation of the current model are described in the following sections.

Validation of Competitive Grain Growth Algorithm

The competitive grain growth algorithm of the current Cellular Automata model was validated by numerical results published by Rai et al. [82]. In their study, a 2D CA domain was initialized with liquid cells. Randomly oriented solid cells are then placed at the bottom of the domain, acting as nucleated grains. The entire domain was subjected to a cooling rate of 0.1 K/s and a thermal gradient of 250 K/m in the positive y-direction. The final solidified grain structure and misorientation angle of the solidified grains were compared with the present CA model and shown in Fig. 4.8. Misorientation of grains is described earlier in this chapter, which refers to the difference between the direction of the thermal gradient and grain orientation angle. Here, the grains which have a grain orientation angle closer to 0° have a smaller misorientation angle. These grains are shown in green and yellow colors according to the defined colorbar. Grains with the smallest misorientation angle are favored to grow during solidification. As shown in Fig. 4.8, for both cases, in the lower part of the domain, the grains with larger misorientation angles fail to grow, competing with grains with smaller misorientation angles. As a result, the number of grains decreases as the solidification progresses. Figures 4.8 (a) and (b) further illustrate that the grains with a misorientation of $\sim\pm 5^0$ are able to survive by the competitive grain growth mechanism for both cases. The comparison indicates that the current CA grain growth model can predict the competitive grain growth mechanism with good accuracy.

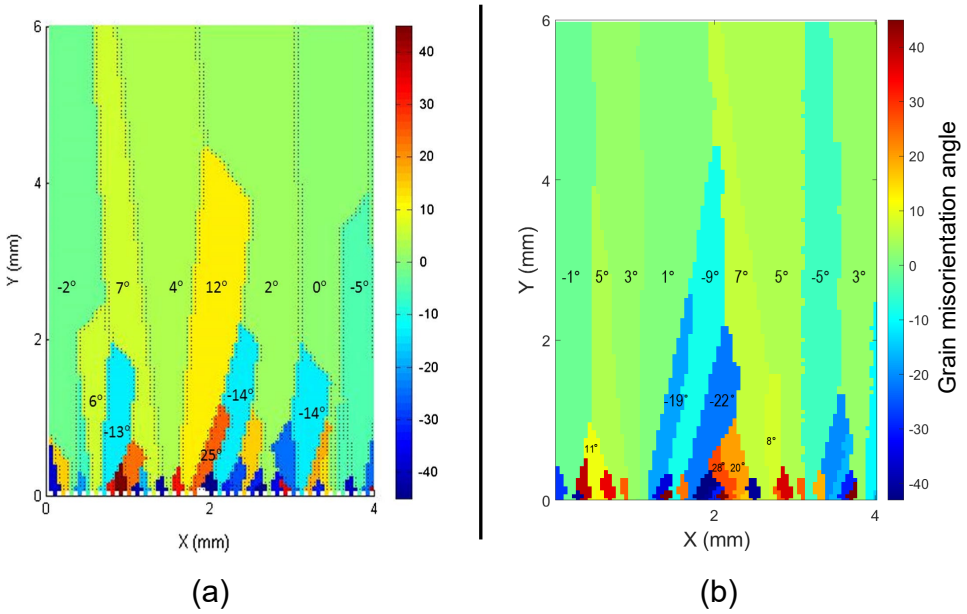


Figure 4.8. Comparison of competitive grain growth algorithm: (a) numerical results computed by Rai et al. [82], and (b) results from the current CA model.

Validation of Average Grain Size

One of the critical parts of this study is to accurately compute the average grain size of the microstructure predicted by the present Cellular Automata (CA) model. The solidified microstructure predicted by the current CA model was compared with the experimental results of Baumard et al. [83]. In their study, a solid rectangular block of 316 Stainless steel was subjected to melting and resolidification by a 400 W laser moving at 400 mm/s scanning speed. The authors analyzed the grain morphology from the microscopic images at a cross-section of the solidified layer. As shown in Figs. 4.9 (a) and (b), the microstructure predicted by the present CA model is qualitatively compared to the published micrograph image by Baumard et al. [83]. The grains and their orientations with respect to the y-axis are shown in different colors in the image of the predicted microstructure. In the experimental micrograph image depicted in Fig. 4.9 (b) the grains

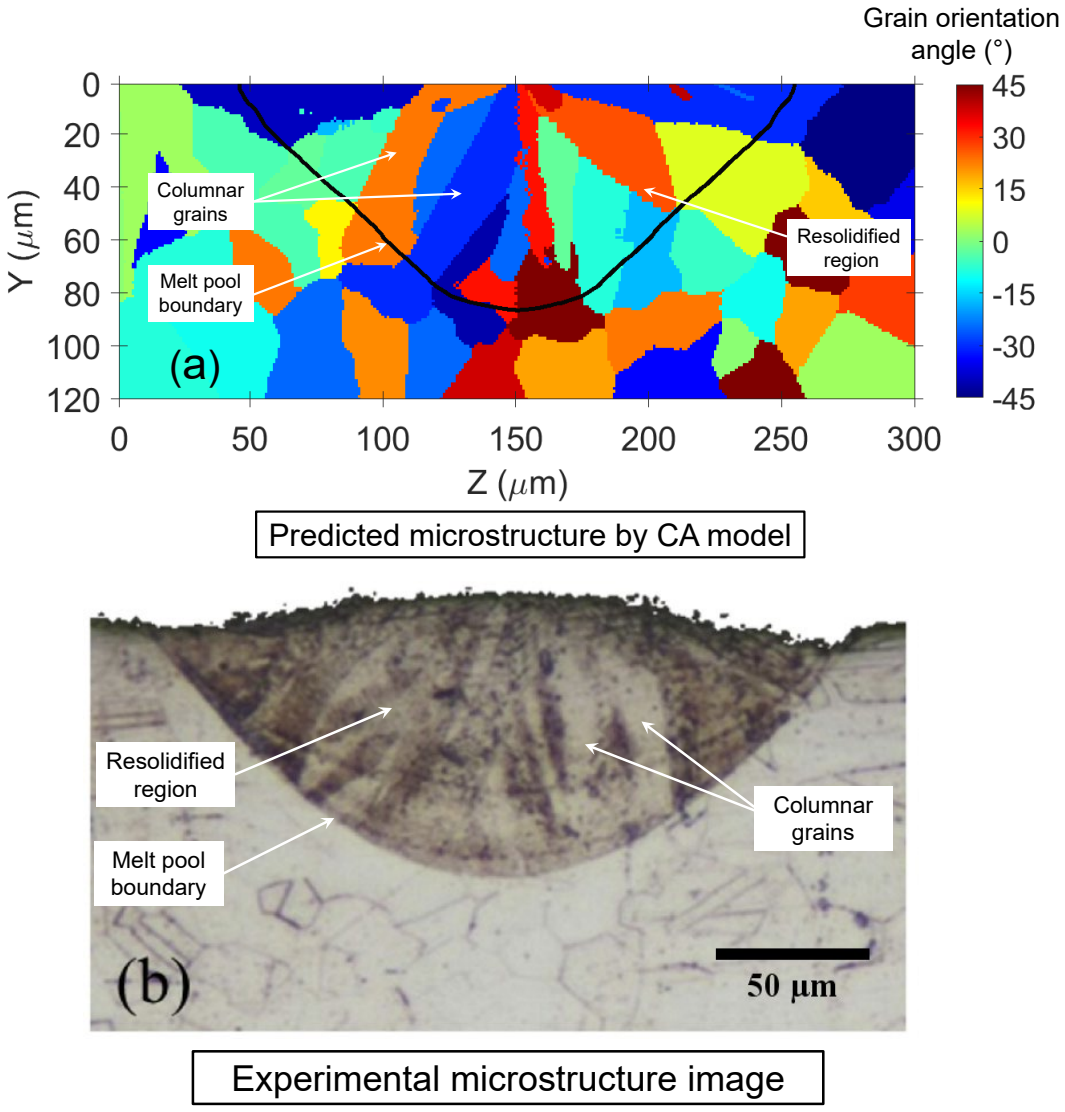


Figure 4.9. Comparison of microstructures for the solidified layer of 316 Stainless steel at a cross-section between (a) results from the present Cellular Automata grain growth model and (b) experimental results published by Baumard et al. [83].

and their adjacent boundaries can be distinguished by a change of texture among them. Figures 4.9 (a) and (b) further illustrate that large columnar grains originated by epitaxial growth predominate the resolidified regions in both cases. Epitaxial growth refers to the growth of grains from the partially melted grains at the melt pool boundary. It is also observed from the figures that the columnar grains are oriented perpendicular to the melt pool boundary, which is the direction of the

local thermal gradient. The visual comparison in the figures indicates that the predicted microstructure by the current CA grain growth model shows good qualitative agreement with the experimental microstructure.

In addition, a quantitative comparison was drawn in terms of average grain size measured from the CA model predicted microstructure with the experimental data documented by Baumard et al. [83]. The average grain diameter at a 2D cross-section was measured using the intercept length method following the procedures described in ASTM E-1382 standard [84]. Figure 4.10 illustrates the process of grain measurement by the intercept length method. According to the ASTM E-1382 standard, a rectangular test grid with parallel test lines was fitted to the image in 0^0, 45^0, $90^0$and 135^0 rotation with respect to the horizontal axis. A grid spacing of 25 μm, larger than the apparent grain diameter, was chosen. The grain boundaries which intersected with the test lines were pointed out. The difference between two intersecting points across the grid line is the grain intercept, as shown in Fig 4.10. In order to measure the mean intercept length, all the intercept lengths were summed and divided by the total number of intercepts. This process yielded a mean intercept length of 17.7 μm for the grains in the resolidified region, predicted by the current CA microstructure model. For this mean intercept length, the average grain diameter was interpolated from Table 2, titled “Grain size relationships” in the ASTM E-1382 standard [84].

In addition, a quantitative comparison was drawn in terms of average grain size measured from the CA model predicted microstructure with the experimental data documented by Baumard et al. [83]. The average grain diameter at a 2D cross-section was measured using the intercept length method following the procedures described in ASTM E-1382 standard [84]. Figure 4.10 illustrates the process of grain measurement by the intercept length method. According to the

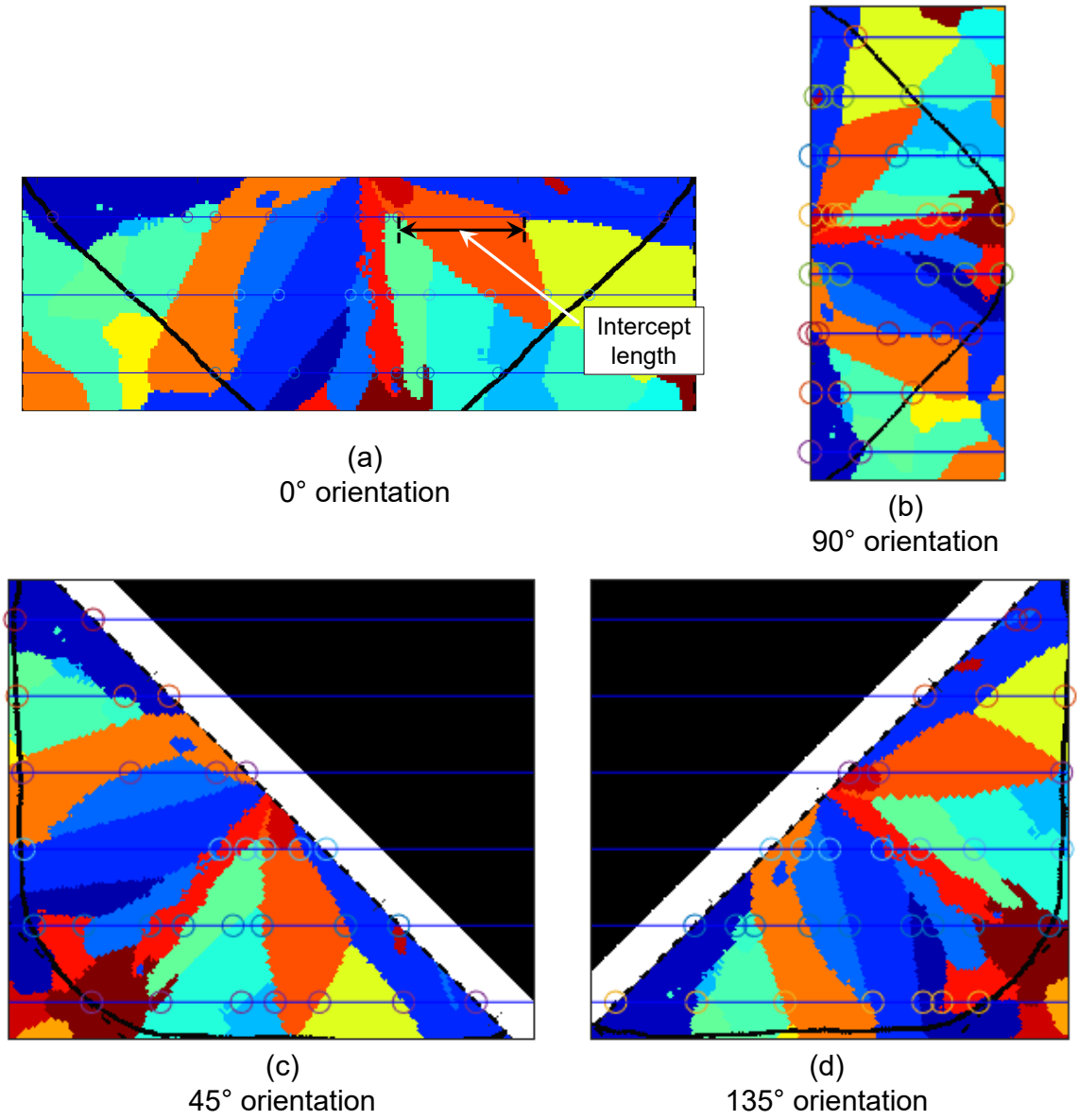


Figure 4.10. Grain size measurement by intercept length method for (a) 0° orientation, (b) 90° orientation, (c) 45° orientation, (d) 135° orientation for the predicted microstructure by the current CA model.

ASTM E-1382 standard, a rectangular test grid with parallel test lines was fitted to the image in 0^0, 45^0, $90^0$and 135^0 rotation with respect to the horizontal axis. A grid spacing of 25 µm, larger than the apparent grain diameter, was chosen. The grain boundaries which intersected with the test

lines were pointed out. The difference between two intersecting points across the grid line is the grain intercept, as shown in Fig 4.10. In order to measure the mean intercept length, all the intercept lengths were summed and divided by the total number of intercepts. This process yielded a mean intercept length of 17.7 μm for the grains in the resolidified region, predicted by the current CA grain growth model. For this mean intercept length, the average grain diameter was interpolated from Table 2, titled "Grain size relationships" in the ASTM E-1382 standard [84]. The average grain diameter found for the cross-section of the predicted microstructure was 20.67 μm, which showed a 6% deviation from the average grain diameter measured by Baumard et al. [83], as documented in Table 4.3. Both qualitative and quantitative comparisons of the predicted microstructure by the current Cellular Automata model are in good agreement with the experimentally published data. Hence, this CA model can be implemented in analyzing microstructures formed during selective laser melting of AlSi10Mg alloy for different process parameters which are discussed in chapter 6.

Table 4.3 Grain size measurement by linear intercept method and comparison of average grain diameter at a cross-section with experimental data.

Image rotation (°)	Number of directed test lines	Grid spacing (μm)	Average intercept length (μm) for each rotation)	Average intercept length (μm) including all rotation)	Average grain diameter from ASTM E-1382 [84]	Experimentally measured average grain diameter by Baumard et al. [83]	Deviation from experimental result
0	3	25	17.7	17.7	20.7	22	6%
90	8	25	16.0				
45	6	25	19.5				
135	6	25	17.5				

CHAPTER FIVE

RESULTS AND DISCUSSIONS

Introduction

The results of the current numerical analysis with coupled Computational Fluid Dynamics (CFD) and Cellular Automata (CA) model of the selective laser melting (SLM) process were prudently interpreted to derive meaningful conclusions. Numerical results for temperature distribution, velocity field, and other thermal variables were computed from the 3D CFD model after the quasi-steady state was achieved. The quasi-steady state was determined by tracking the maximum temperature history at the top surface of the computational domain. The distribution of nanoparticles was evaluated in 2D transverse planes using the current CFD model's particle transport algorithm. A Cellular Automata (CA) model was used to simulate the microstructure evolution in 2D transverse planes during the solidification process. The temperature history, local thermal gradient, and final nanoparticle distribution computed from the CFD model were considered in the CA model while simulating the microstructure formation. In addition, the current CA model simulated two types of microstructures: 1) considering the bulk nucleation effects of the nanoparticles and 2) without considering the bulk nucleation effects of the nanoparticles. These two types of microstructures were compared qualitatively and quantitatively in this study. The comparison showed interesting findings that were consistent with experimentally published results. The effects of three process variables were analyzed: i) laser power, ii) laser scanning speed, and iii) the preheating temperature. To study the effects of the parametric change, only one parameter was changed while the other two were kept constant. Process parameters used in the

current model are described in the following section. ANSYS CFD-Post [53] was used to post-process the CFD results, while MATLAB [79] was used to post-process the predicted microstructure.

To the best of our knowledge, no studies were conducted to numerically calculate the diffusion of the nanoparticles in the SLM process. In the current numerical investigation, the transport of the nanoparticles in 2D transverse planes was evaluated from the 3D CFD model of the SLM process. The influence of the liquid metal flow on the transport of the nanoparticles inside the molten pool was studied in detail. In addition, the final distribution of the nanoparticles calculated by the CFD model was mapped into the Cellular Automata (CA) domain. The positions of the nanoparticles acted as bulk nucleation sites in the present CA microstructure model. The coupling of the nanoparticle distribution with the CA microstructure model is a new aspect of simulating microstructure by the CA model. The detailed workflow of coupling the CFD model with the CA model was described in Fig. 4.6. This novel modeling approach was used to investigate the microstructure formation in the presence of the nanoparticles.

Modeling of Process Parameters

One of the objectives of this study was to describe the experimental findings in selective laser melting (SLM) of metal matrix nanocomposites with numerical tools. This was done so because the experimental measurement systems for the SLM process are too expensive and prone to be inaccurate. The modeling of the process parameters was based on physical process variables used in the SLM process, such as laser power, laser scanning speed, laser spot diameter, preheating temperature etc. The process parameters that were varied in the current numerical study are: i) laser power, ii) laser scanning speed, and iii) the preheating temperature.

The present research was aimed to analyze the effects of these process variables on the local distribution of reinforced ceramic nanoparticles in the solidified microstructure of the metal matrix. In addition, temperature distribution, velocity field, and Marangoni number associated with the molten liquid metal were computed from the CFD model. The effects of these calculated parameters on the transport of the nanoparticles were explored. The microstructure predicted by the Cellular Automata (CA) model was one way coupled with the CFD model. The coupling of the CA model with the CFD model was described earlier in Fig 4.6. In addition, the solidification parameters such as thermal gradient and cooling rate calculated from the CFD model were used to assess the dynamics of the microstructure formation. Furthermore, the effects of the local nanoparticle distribution on the microstructure formation were thoroughly analyzed.

Symmetry was considered in the CFD model to increase the efficiency of computational time and resources. The top wall of the domain was assumed as a non-deformable interface between the ambient air and metallic material. A moving laser heat source was modeled on the top wall using a volumetric Gaussian distributed heat source using Eq. 2.5. Marangoni convection and heat loss due to radiation, convection, and vaporization were added as the boundary conditions on the top wall using Eqs. 2.6-2.12. Except for the symmetric wall, the other walls had convection and radiation heat losses with the ambient. A total of 60,000 TiB_2 nanoparticles were introduced into the CFD domain as discrete particles, whereas, AlSi10Mg aluminum alloy was chosen as the metallic material for the powder bed and substrate region. The resulting nanoparticle redistribution and temperature variables along two transverse planes were imported into a Cellular Automata model. The CA model simulated the 2D microstructures across the transverse plane, illustrating the formation of grains. The average grain size was measured following the ASTM E-1382

standard [84] and compared between the microstructures generated with nanoparticles and without nanoparticles.

Computational Matrix

The process parameters selected for the present study are listed in Table 5.1.

Table 5.1. Process parameters used in the present numerical model.

Parameter	Value
Laser power, P (W)	125, 150,175 and 200
Laser scanning speed, V_L (mm/s)	300,400,500 and 600
Preheating temperature, T_0 (K)	300, 373 and 473
Laser spot radius, r_b (μm)	50
Optical penetration depth of the laser, S (μm)	50
Porosity of the powder bed, ϕ	0.5
Powder bed thickness, δ (μm)	50

The effects of varying laser power, laser scanning speed, and preheating temperature of the powder bed and substrate were investigated in the current study. The CFD model simulated a total of 11 cases. The studied cases were categorized in three sections as listed in Table 5.2:

Table 5.2. Computational matrix for the study of process parameters.

Name of the Study	Laser power, P (W)	Laser scanning speed, V_L (mm/s)	Pre-heating temperature, T_0 (K)
Varying laser power	125	500	373
	150	500	373
	175	500	373
	200	500	373
Varying laser scanning speed	150	300	373
	150	400	373
	150	500	373
	150	600	373
Varying pre-heating temperature	150	500	300
	150	500	373
	150	500	473

As mentioned earlier, the Cellular Automata computational domain was in 2D, and it was coupled with two transverse planes in the CFD domain. The CA model simulated two types of microstructures mentioned earlier at those two transverse planes for all the cases listed in Table 5.2. As a result, a total of 44 cases were run using the CA model.

Nanoparticles were uniformly distributed in the powder bed region of the CFD domain. In order to increase computational efficiency, rather than distributing the nanoparticles in the entire volume of the powder bed domain, they were uniformly distributed in a region of 750 μm × 50 μm × 200 μm, and shown in Fig 5.1 (a). The initial distribution of the nanoparticles was based on the dimensions of the scan track of the laser and the highest half-width of the molten pool. Nanoparticles' initial positions were only affected if a molten pool was created at their locations. The length of the laser scan track selected for this study was 750 μm in the x-direction starting from x = 125 μm. Since the molten pool velocities were prominent in the laser scan track, the nanoparticles were positioned along the laser scan track. In addition, the highest half-widths of the molten pools calculated in the z-direction were less than 200 μm. As a result, the nanoparticles initially positioned beyond the highest width of the molten pool along the z-direction were not affected. So, selecting initial nanoparticles positions inside the dimensions illustrated in Fig. 5.1 was a reasonable assumption. The transverse (y-z) planes that were subjected to study in the present investigation were at x= 550 um and x = 650 μm. The same initial nanoparticle distribution was employed in those transverse planes. During laser melting and solidification, the transport of nanoparticles was analyzed on those planes. Initially, 400 solid nanoparticles were positioned in those transverse planes and are shown in Fig. 5.1 (b). The initial distribution and volume fraction of nanoparticles in the CFD domain were kept the same for all the cases. Nanoparticle tracking

was executed from the reference frame of the 2D transverse planes at x = 550 um and 650 um. Only the nanoparticles located in the cells along the selected planes were tracked at any given time and displayed in the result. Ignoring the x coordinates of the nanoparticles, the particle distribution was studied based on their y and z coordinates. After the 2D transverse planes were fully solidified, the distributions of the nanoparticles were imported into the 2D CA computational domain. The cells of the CA domain holding the nanoparticles were selected as the bulk nucleating cells when prescribed conditions were fulfilled. The bulk nucleation algorithm of the current CA model was described earlier in chapter 4.

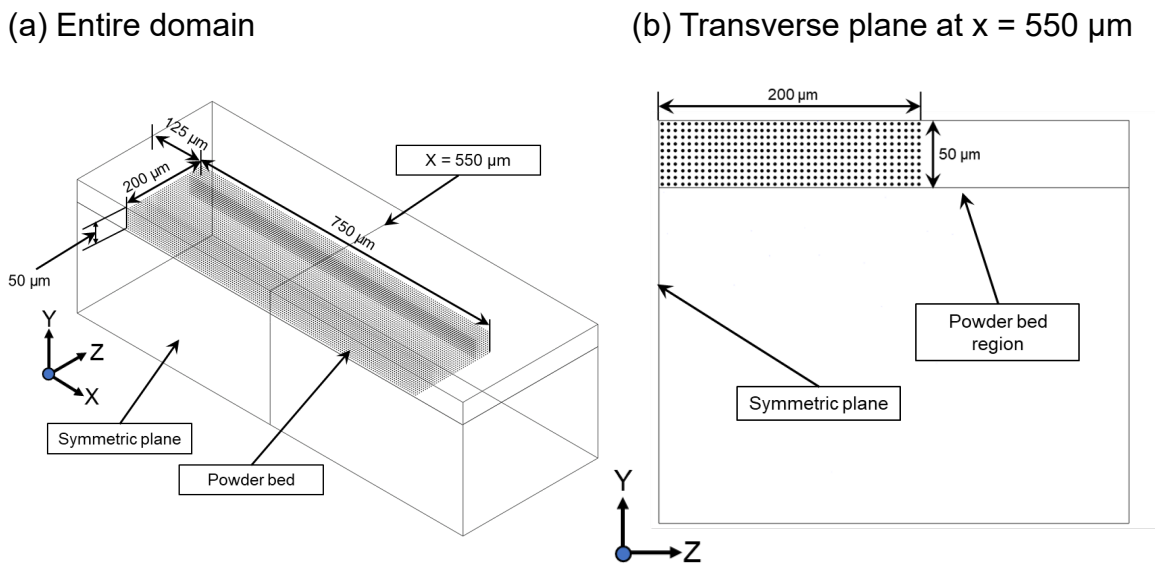


Figure 5.1. Initial distribution of the nanoparticles: (a) in entire domain, (b) at a transverse (y-z) plane at x = 550 µm.

Temperature Characteristics in Selective Laser Melting

Temperature distribution and its associated temperature gradient and temperature history field play a crucial role in determining the stability of the selective laser melting (SLM) process. Temperature distribution in the powder and substrate region was primarily controlled by the energy density of the moving laser modeled as a volumetric heat source. Figure 5.2 shows the temperature distribution at time 1050 μs, for the case with 150 W laser power, 500 mm/s scanning speed with preheating temperature of 373 K. The volumetric heat source was Gaussian in the horizontal (x-z) plane and exponentially decreased from the surface of the powder bed along its depth in the vertical direction. As a result, it created a high-temperature region colored in red around the laser spot center on the powder bed surface, as shown in Figure 5.2 (b). An increase in temperature was caused by two main factors, i.e., heat exerted by the moving laser and heat transfer from the previous laser-activated region. As depicted in this figure, the temperature gradually decreased from the laser spot center to the width and the depth of the powder bed and the substrate. When the temperature reached the liquidus temperature of AlSi10Mg alloy, i.e., 873 K, the region melted and became a molten pool. Since heat exchange took place between the powder bed and the underlying solid substrate, both the powders and the solid substrate melted to form the liquid molten pool. Figure 5.2 (b) shows the molten pool region bounded by the liquidus temperature isotherm. The molten pool solidified as the laser heat source moved away from the molten region, diffusing heat to the surrounding metallic materials and the ambient through conduction, convection, and radiation heat transfer. The current model employed very low temperature-dependent thermal conductivity for the powder bed because of its porosity using Eqs. 2.13 and

2.14. As a result, the solidified region and the molten pool have a very high thermal conductivity than the unmelted powder region, as shown in Fig 5.3.

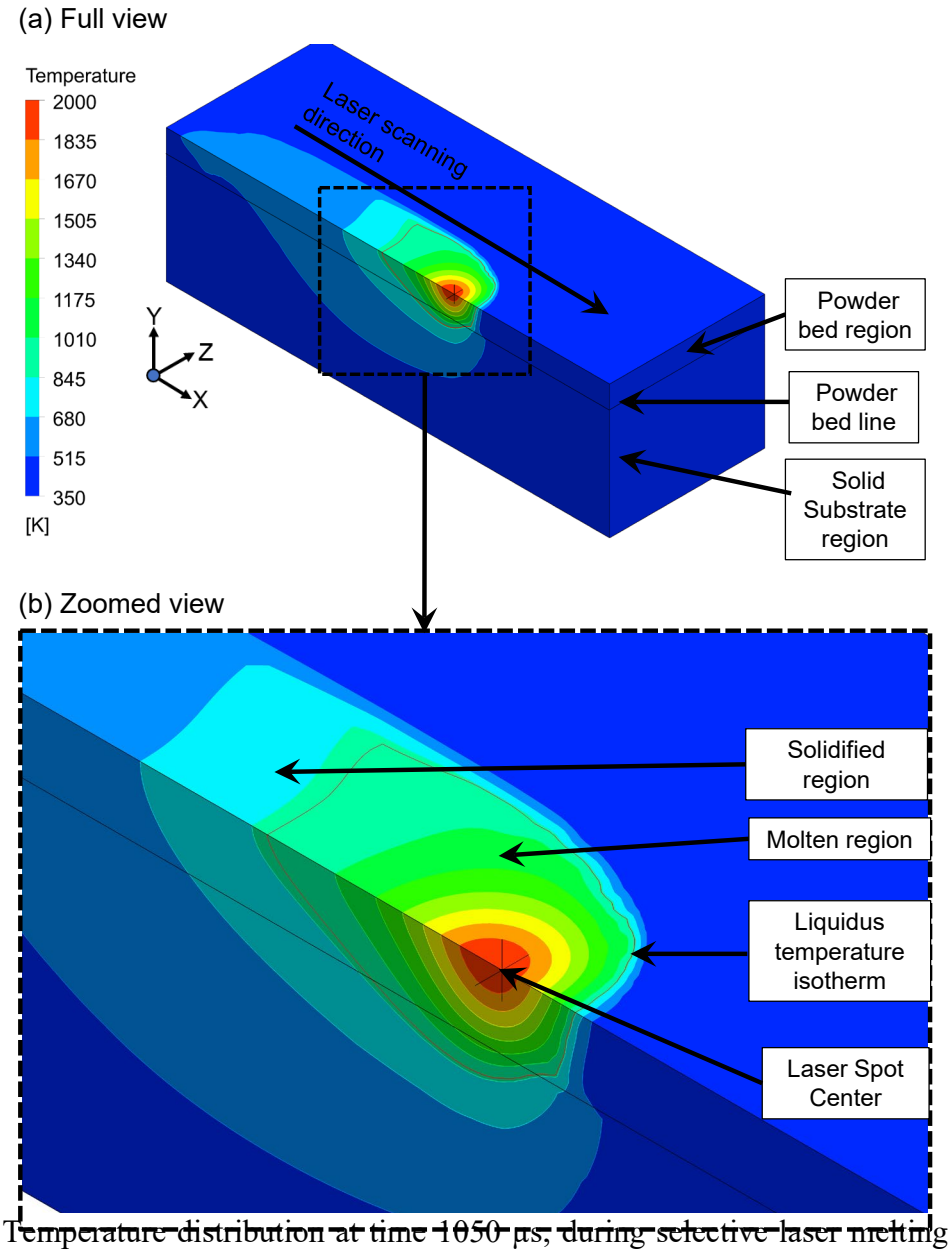


Figure 5.2. Temperature distribution at time 1050 μs, during selective laser melting at 150 W laser power and 500 mm/s scanning speed with 100° C preheated temperature: (a) full isometric view of the computational domain, (b) zoomed view of the selected box.

The difference in thermal conductivity yielded distinctive temperature distributions among the powder bed, the molten pool, and the solid region. Figure 5.3 shows that the thermal conductivity is very low in the unmelted powder region and very high in the solidified region. The unmelted powder region is colored in blue, while the solid regions are shown in red color in this figure. The figure further shows that the low thermally conductive powder region exists at the front and the left side of the molten pool boundary. Therefore, the accumulated heat in the molten pool did not diffuse very well through these regions. Conversely, the heat diffusion rate was much higher behind the molten pool because of the high thermal conductivity of the solid regions. Hence, the temperature profile is much elongated behind the molten pool compared to its front and the sides and shown in Fig. 5.3.

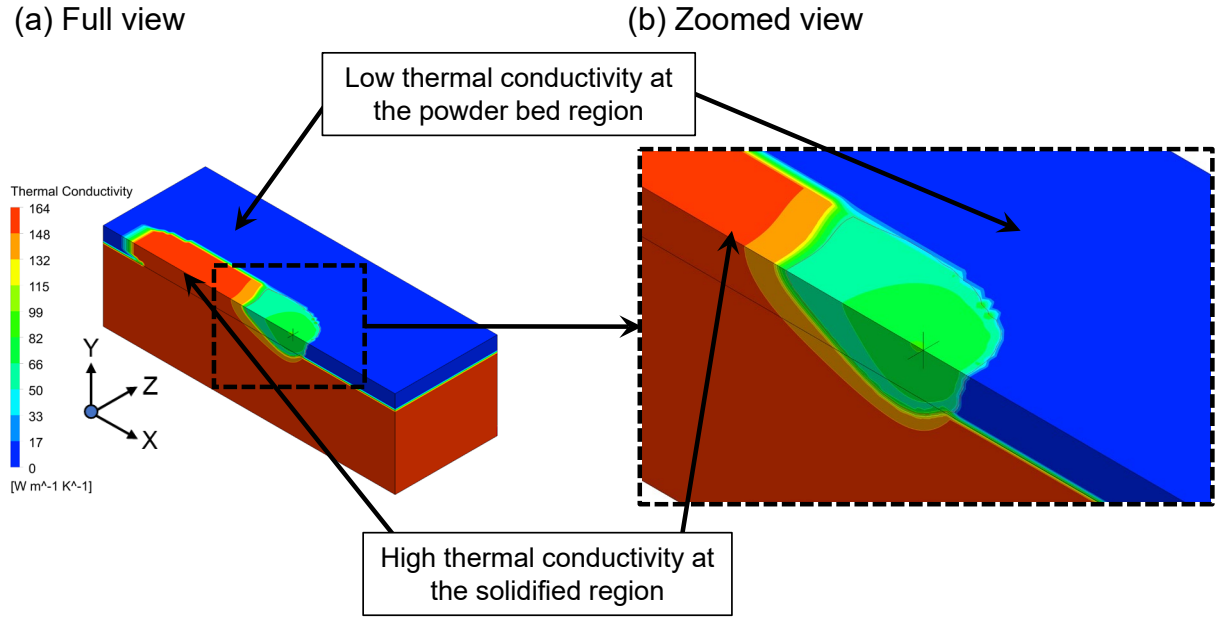


Figure 5.3. Difference in thermal conductivity in the powder bed, molten pool, and substrate region during selective laser melting: (a) full isometric view of the computational domain, (b) zoomed view of the selected box.

The temperature gradient field was also affected by the difference in the thermal conductivity among the powder bed, liquid, and solid metal during the SLM process. In addition, Marangoni convection in the molten pool is dependent on the temperature gradient at the free surface of the liquid metal. Hence, this temperature characteristic significantly influences the liquid metal flow in the molten pool. Figure 5.4 shows the temperature gradient field for the same case shown in Fig. 5.2. The relative magnitude and the direction of the temperature gradient vector

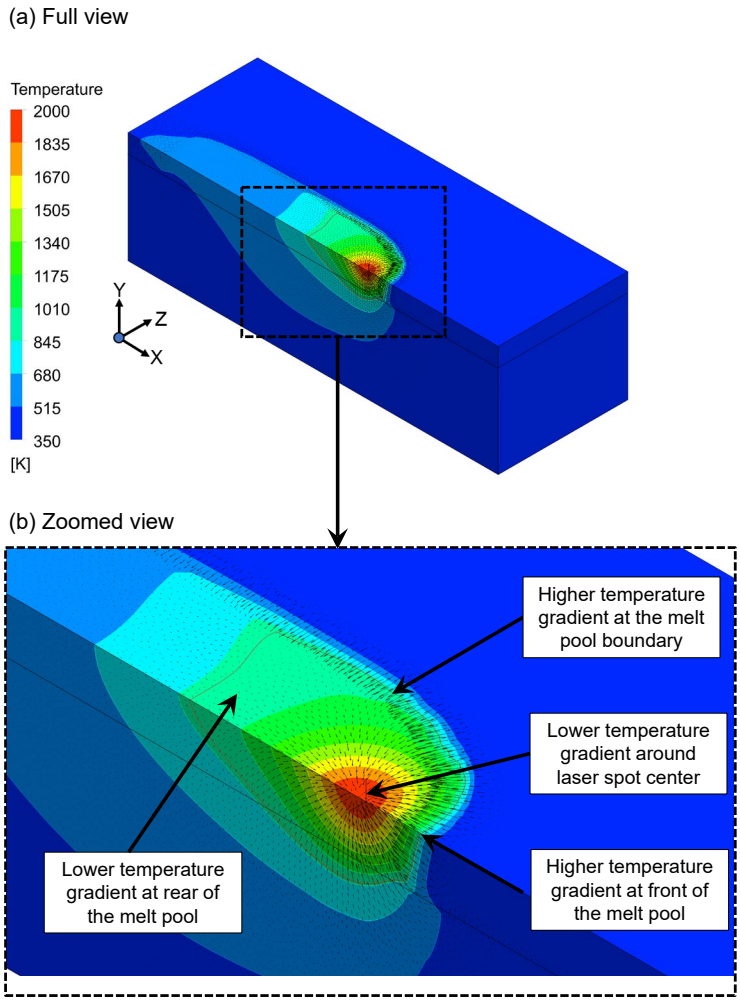


Figure 5.4. Temperature and thermal gradient distribution at time 1050 µs during selective laser melting at 150 W laser power, 500 mm/s scanning speed, and 100° C preheated temperature: (a) full isometric view of the computational domain, (b) zoomed view of the selected box.

field are represented by the length and direction of the arrows in Fig. 5.4. The vectors are perpendicular to the temperature contours and directed towards the high-temperature region around the laser spot center. This figure further depicts a higher temperature gradient at the front and sides of the molten pool boundary at the powder bed surface compared to the lower thermal gradient at the rear end of the molten pool. The thermal gradient gradually increased in the intermediate region from the melt pool boundary to the periphery of the high temperature region. From the periphery to the center of the high temperature region, the temperature gradient again decreased to a low value. Since laser heat previously melted the rear end of the melt pool and thus increased its thermal conductivity, the thermal gradient was relatively low there.

Temperature distribution in the symmetric and the transverse plane is shown in Fig. 5.5. As discussed earlier, the liquidus temperature line bounds the melt pool region. The molten pool region is defined by its length, width, and depth. The length and the maximum depth of the molten pool can be determined directly from the symmetric plane, shown in Fig. 5.5 (a). As the current model assumed symmetrical conditions, only the half width of the molten pool can be calculated. The depth of the molten pool varies along the molten pool length. The half width of the molten pool also varies at different cross-sections of the melt pool along its length. The reason behind the variation of the shape of the molten pool at different cross-sections is discussed later in this chapter. Half width can be calculated from the transverse plane, as shown in Fig 5.5 (b). The molten pool dimensions for this case are listed in Table 5.3.

When the maximum temperature reaches a steady state, melt pool volume becomes stable. A high melt pool volume ensures good fusion between the powder bed and the underlying

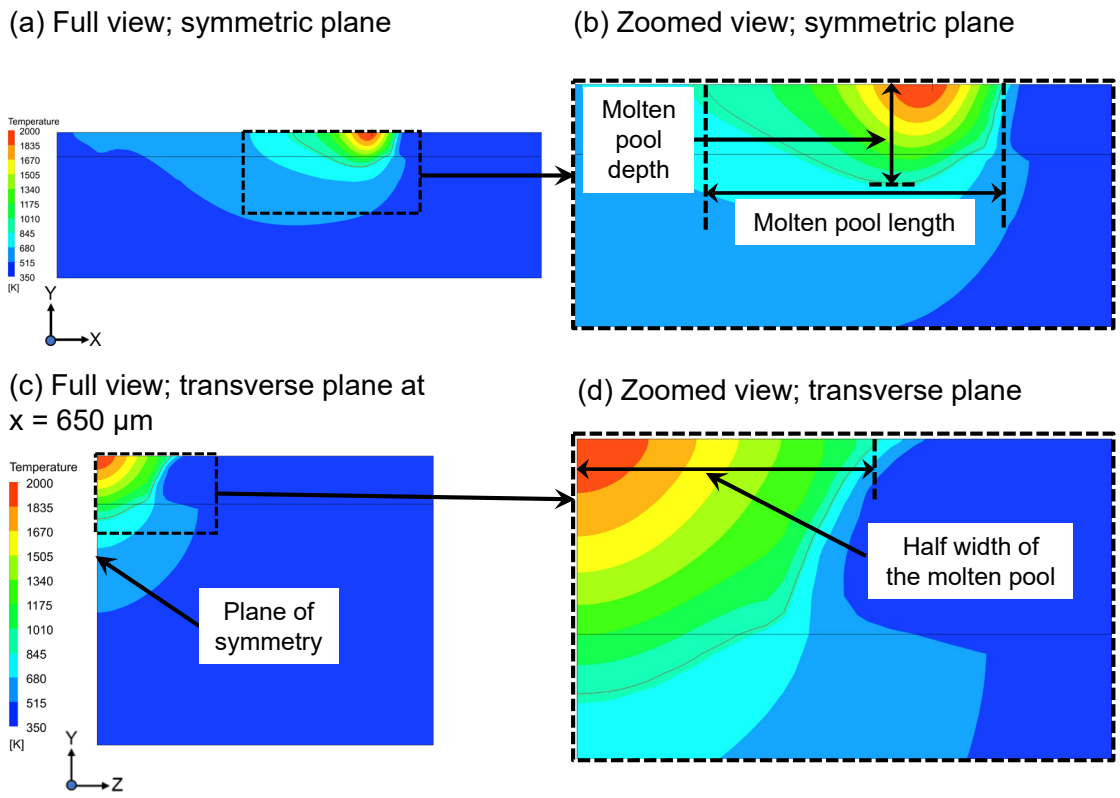


Figure 5.5. Melt pool dimensions in (a) symmetric plane (b) transverse plane.

Table 5.3 Molten pool dimensions.

Case	Molten pool half width (µm)	Molten pool depth (µm)	Molten pool length (µm)
150 W laser power, 500 mm/s scanning speed with 100°C preheating	102	70	215

substrate, reducing defects due to improper melting. Figure 5.6 shows the histories of the maximum temperature and temperature of the representative points P1 and P2. The process parameters for Fig. 5.6 are the same as selected for illustrating Fig. 5.2. The temperature history plot shows that the maximum temperature at the powder bed surface rises rapidly to a maximum stable temperature of 1980 K at 400 µs. This phenomenon indicates that the temperature

distribution in the SLM process reaches a steady state very quickly. After the laser scanning is completed at 1500 µs, the max temperature decreases sharply below the liquidus temperature indicating all the molten region is solidified. The temperature history curve for points P1 and P2 indicates that temperature rises very quickly to the maximum temperature of 1980 K once the moving laser heats these selected points. The temperature of these selected points decreases rapidly as the laser heat source moves away. However, after the sharp decrease from the maximum temperature, those regions solidify at a slower rate as their temperatures go close to the liquidus temperature.

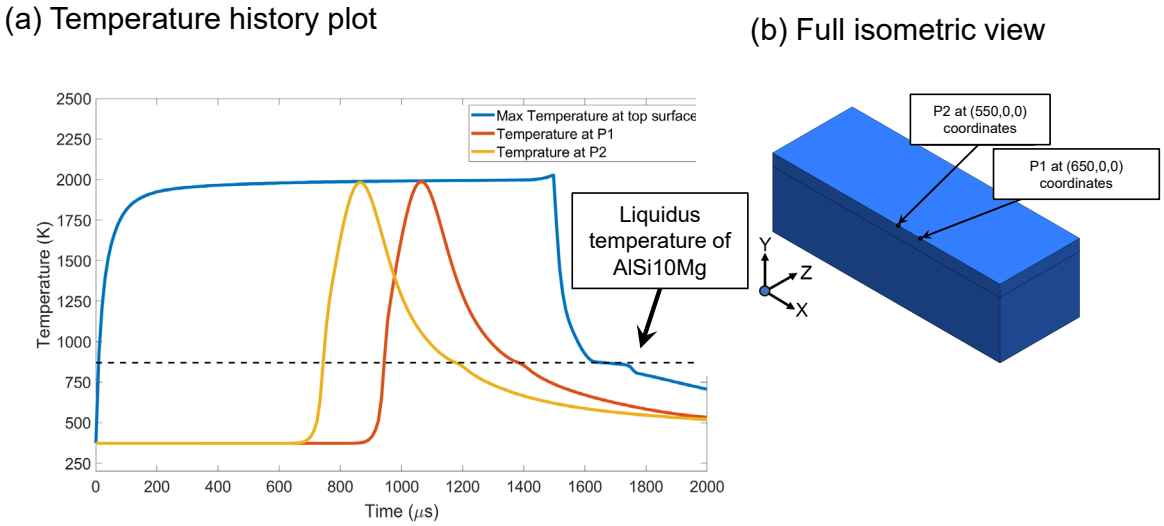


Figure 5.6. Temperature histories of the maximum temperature and representative points P1 and P2: (a) temperature history plot, (b) Coordinates of points P1 and P2.

Temperature distributions due to moving lasers at different times are shown in Figure 5.7 (a-d). The figure illustrates that at the early stage of the laser scanning process, i.e., 100 µs, the maximum temperature is much lower than the steady maximum temperature of 1980 K. Therefore, a small molten pool is created at that time instant. At 600 µs, the maximum temperature and the corresponding temperature distribution in the molten pool reach a steady state. As a result, a similar

temperature profile is observed in the melt pool at the top surface and the symmetric plane at 1050 µs. As shown in the temperature history plot in Fig. 5.6 (a), the maximum temperature quickly drops down after the laser scanning is completed. Fig 5.7 (d) illustrates the same phenomena in the temperature distribution at 1600 µs. The figure shows that the high temperature region disappears at this time instant. Consequently, the molten region is solidifying from all sides due to heat loss to its surroundings.

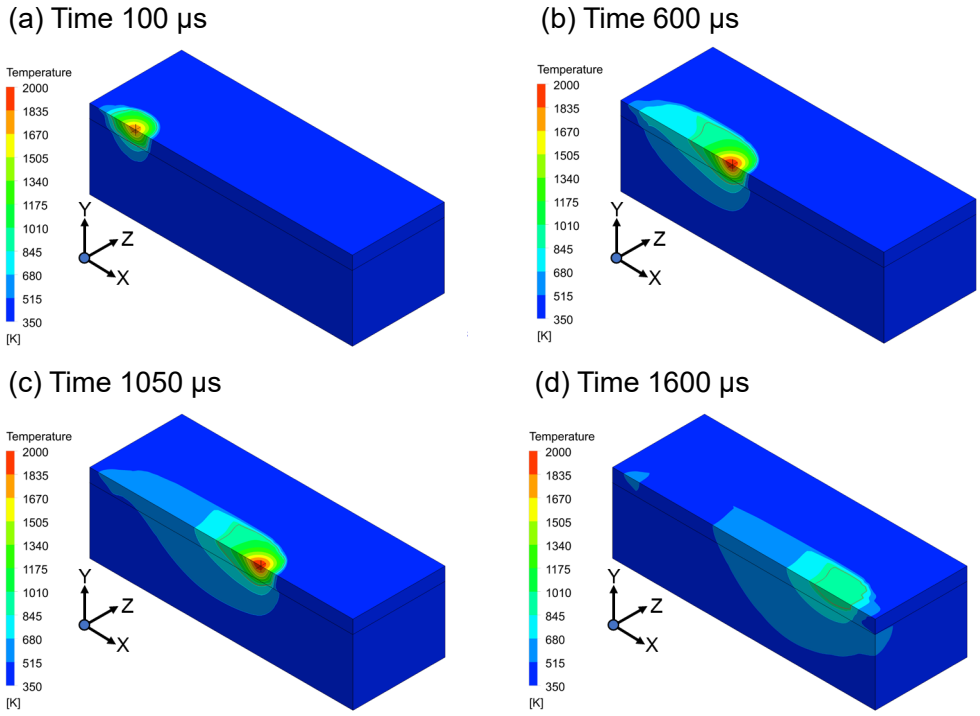


Figure 5.7. Temperature distribution due to moving laser for 150 W, 500 mms/s scanning speed at (a) time 100 µs, (b) 600 µs, (c) 1050 µs, (d) 1600 µs.

Velocity Distribution in Molten Pool

Velocity distribution inside the molten pool is primarily driven by Marangoni convection, natural convection, and the viscosity of liquid metal. Since the Marangoni surface tension coefficient is

negative for AlSi10Mg alloy, the Marangoni force is exerted opposite to the thermal gradient direction. This Marangoni force directs an outward flow from the center to the boundary of the molten pool on the free surface, as shown in Fig. 5.8. The temperature and the velocity field at a time of 1050 µs for a 150 W laser moving at 500 mm/s scanning speed are illustrated in the figure.

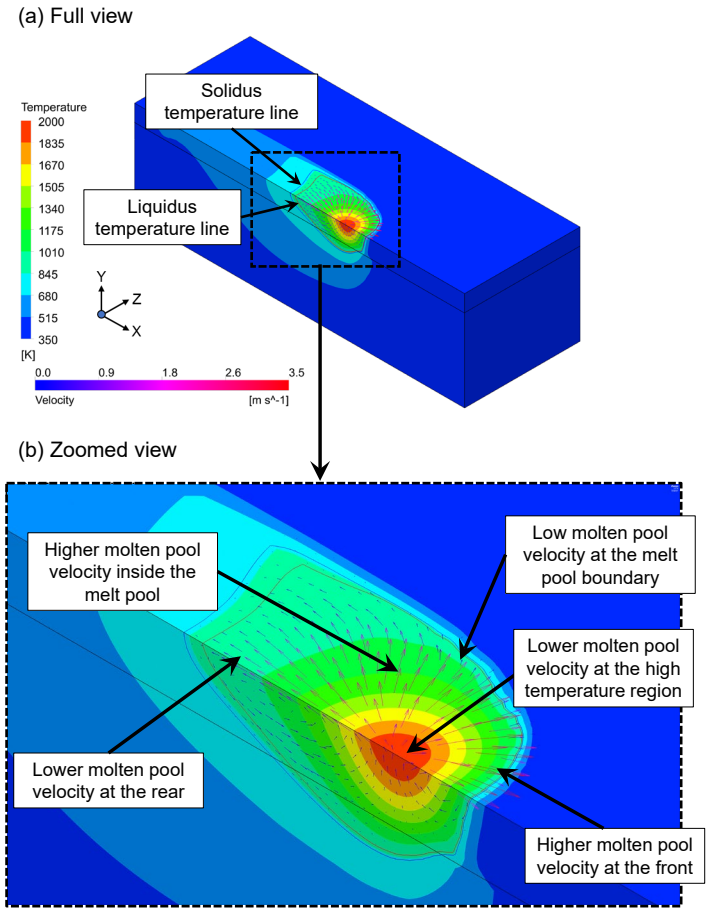


Figure 5.8. Temperature and velocity distribution for at time 1050 µs during selective laser melting for 150 W laser moving at 500 mm/s scanning speed, and 100° C preheated temperature: (a) full isometric view of the computational domain, (b) zoomed view of the selected box.

The magnitude of the velocity is differentiated by the color and the relative length of the arrows depicted in this figure. As can be seen from the figure, the velocity magnitude is lower at the center and the boundary of the molten pool. Whereas the molten metal accelerates and decelerates in the

intermediate region. As discussed earlier, the temperature gradient was low in the middle of the high-temperature region. This induced a low surface tension force at the center of the high temperature region at the free surface and resulted in molten metal flowing outwards at a low velocity. The velocity magnitudes then increased in the intermediate region, caused by a higher temperature gradient. The molten pool flow finally decreased as it approached its boundary, where the liquid was more viscous than its intermediate region. A temperature-dependent viscosity was set for the liquid metal using Eq. 2.17-2.18, which showed higher viscosity at a lower temperature at the molten pool boundary than in the other regions. In addition, as expected, no velocity is shown in the unmelted region in Fig. 5.8, as a high mushy zone constant was set for the solid and the powder region, increasing its viscous effects. The figure also depicts that the molten pool velocity is higher at the front of the melt pool compared to its rear part because of its higher temperature gradient.

The Marangoni force and the buoyancy force induce two opposite recirculation zones parallel to the symmetry plane. To illustrate this phenomenon, the velocity field in the symmetric plane and two planes parallel to the symmetric plane (x-y) at z = 40 μm and z = 80 μm are selected, as shown in Fig. 5.9. Process parameters were the same as used before. Figure 5.10 shows the temperature and the velocity field tangential to these selected planes. As shown in Figs. 5.10 (a1-a2), at the symmetric plane, a clockwise rotating flow at the front of the melt pool and an anti-clockwise rotating flow at the rear of the molten pool exist. As shown in Fig. 5.4, the thermal gradient on the free surface of the symmetric plane is directed towards the high temperature region. As a result, Marangoni surface tension force is directed outwards at the free surface. This Marangoni force drives the liquid metal outward from the center of the high temperature region to

the molten pool boundary. As shown in Fig. 5.10 (a1-a2), the temperature of the liquid metal is higher around the center of the high temperature region, and gradually, it decreases along the molten pool boundary. The hotter liquid metal near the central region floats up to the surface and while the cooler liquid metal near the molten pool boundary sinks along the molten pool boundary to the bottom of the molten pool. Therefore, two strong recirculation zones are observed in the symmetric plane of the molten pool due to Marangoni and natural convection. The directions of the rotating flows of these two recirculation zones are opposite to each other and are shown in Fig. 5.10 (a1-a2). However, these two recirculation zones meet below the center of the high temperature region. This generates a combined upward flow in that region which is shown in Figs. 5.10. The

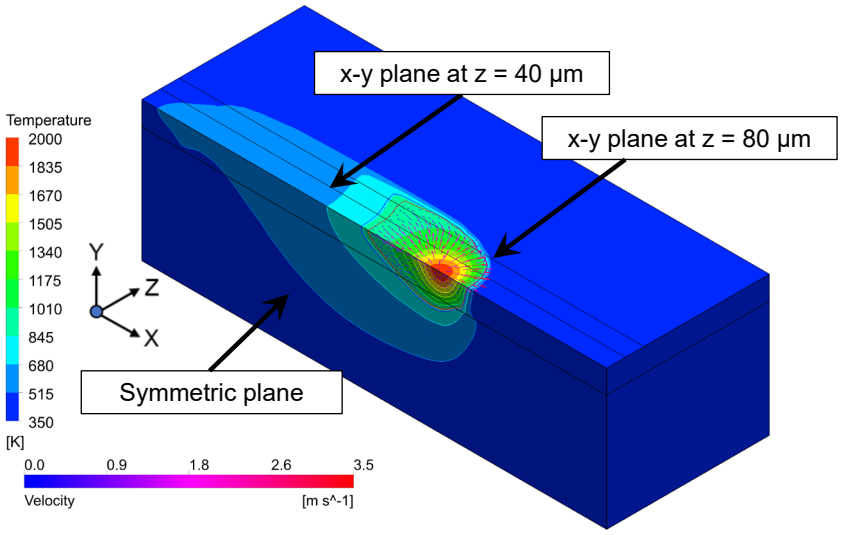


Figure 5.9. Selected x-y planes from the isometric view

strength of the recirculation zones gradually decreases as it moves from the symmetric plane towards its width in the z-direction, as depicted in Figs. 5.10 (b1-b2). Finally, from Figs. 5.10 (c1-c2), it is evident that when the selected x-y plane is close to the molten pool boundary, the recirculation zone diminishes, and the liquid metal flows downward towards its boundary.

For the case of transverse planes, three transverse (y-z) planes are selected in the temperature and velocity distribution shown in Fig. 5.8. The selected planes are depicted in Fig. 5.11, where one plane is at the front of the high temperature region, and two planes are behind the

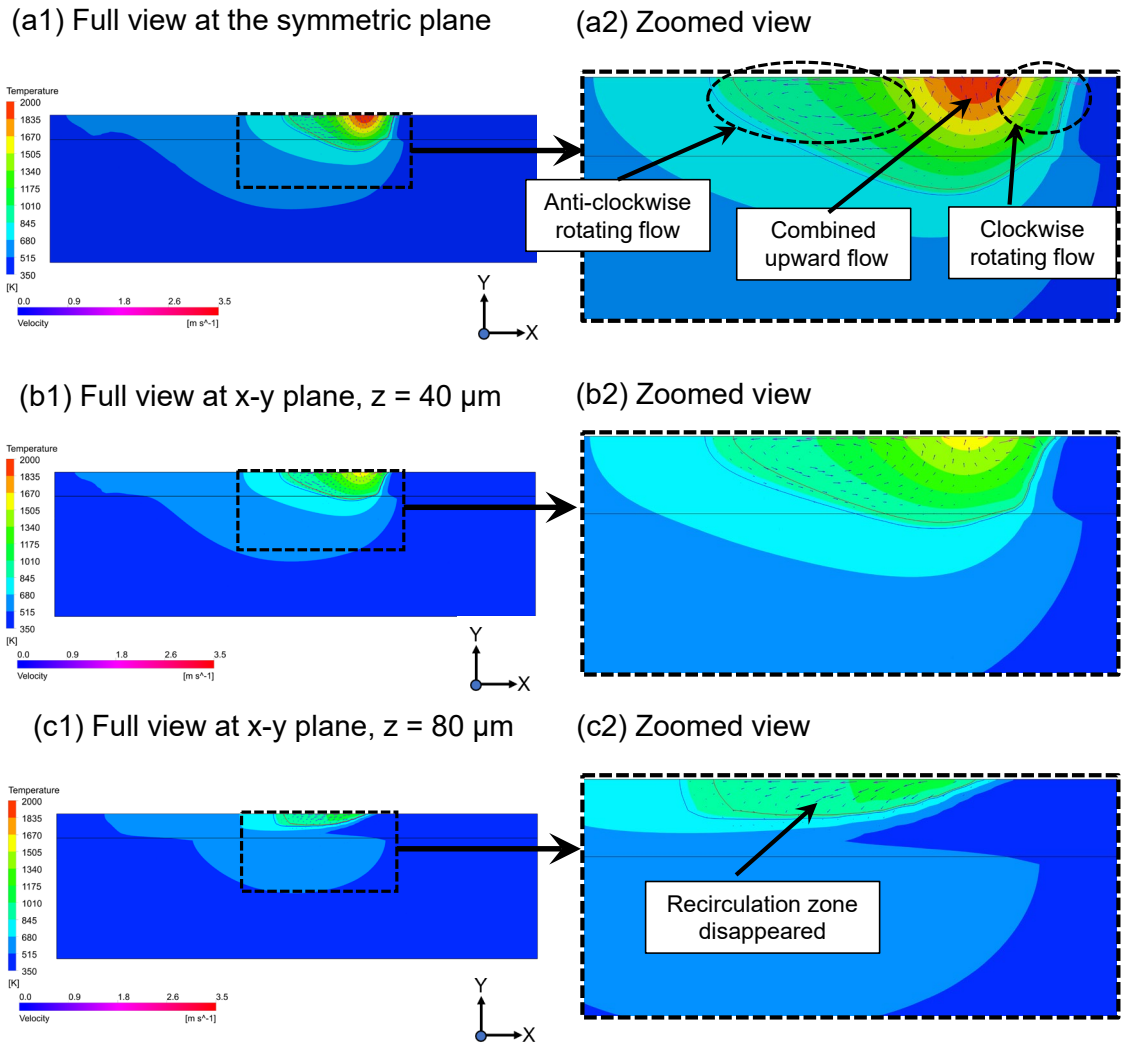


Figure 5.10. Temperature and the tangential velocity field at the selected x-y planes depicted in Fig. 5.9: (a1,b1, and c1) full view of the selected planes, (a2,b2, and c2) zoomed view of the selected boxes.

high temperature region. The temperature and the tangential velocity field of the selected transverse planes are illustrated in Figs. 5.12 (a-c). As shown in Fig. 5.12 (a1-a2), a small

recirculation zone is created near its molten pool boundary, propelled by the Marangoni and buoyancy forces. The normal of this recirculation zone is perpendicular to the normal of the recirculation zones observed in the symmetric plane. The transverse planes shown in Fig 5.12 (b1-b2) are located behind the high temperature region. This figure describes that solidification occurs

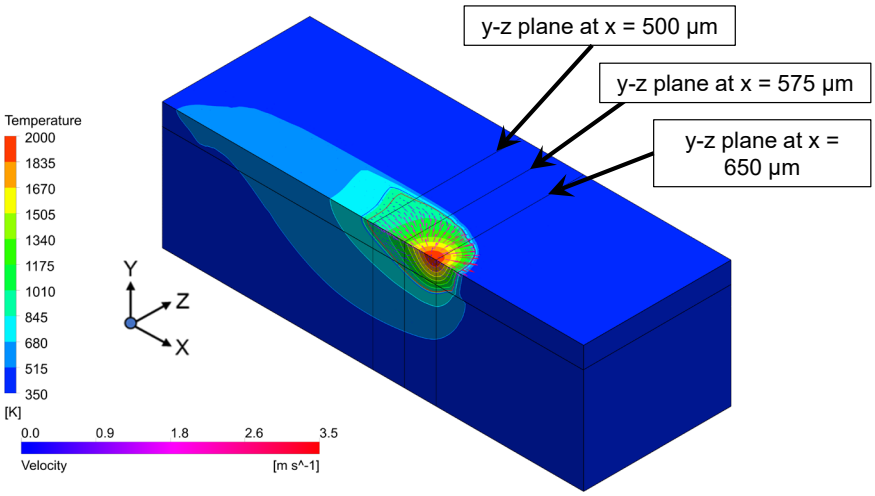


Figure 5.11. Selected y-z planes along the melt pool from the isometric view

from the bottom of the melt pool boundary. The solidus temperature line represents the solidification front. A wider recirculation zone is observed close to the left edge of the molten pool boundary. As a result, the half width of the melt pool increases at this plane. Due to this wider recirculation zone, the heat is convected from the center to the molten pool boundary. Therefore, the temperature variation within this planer region is very small, which induces a weaker Marangoni force. The tangential velocity field at the rear end of the molten pool is shown in Fig 5.12 (c1-c2). At this particular plane, the recirculation zone vanishes, and a downward flow of the molten liquid is observed in this plane.

The influence of Marangoni convection on the recirculation zones created in the x-y and y-z planes has been determined by calculating the Marangoni number of the flow field. Marangoni

number depends on the selected SLM process parameters, which are discussed later in this chapter. It is also worth noting that the natural convection and viscosity of the liquid metal influence the strength of the recirculation zone along with the Marangoni convection. As the mean temperature

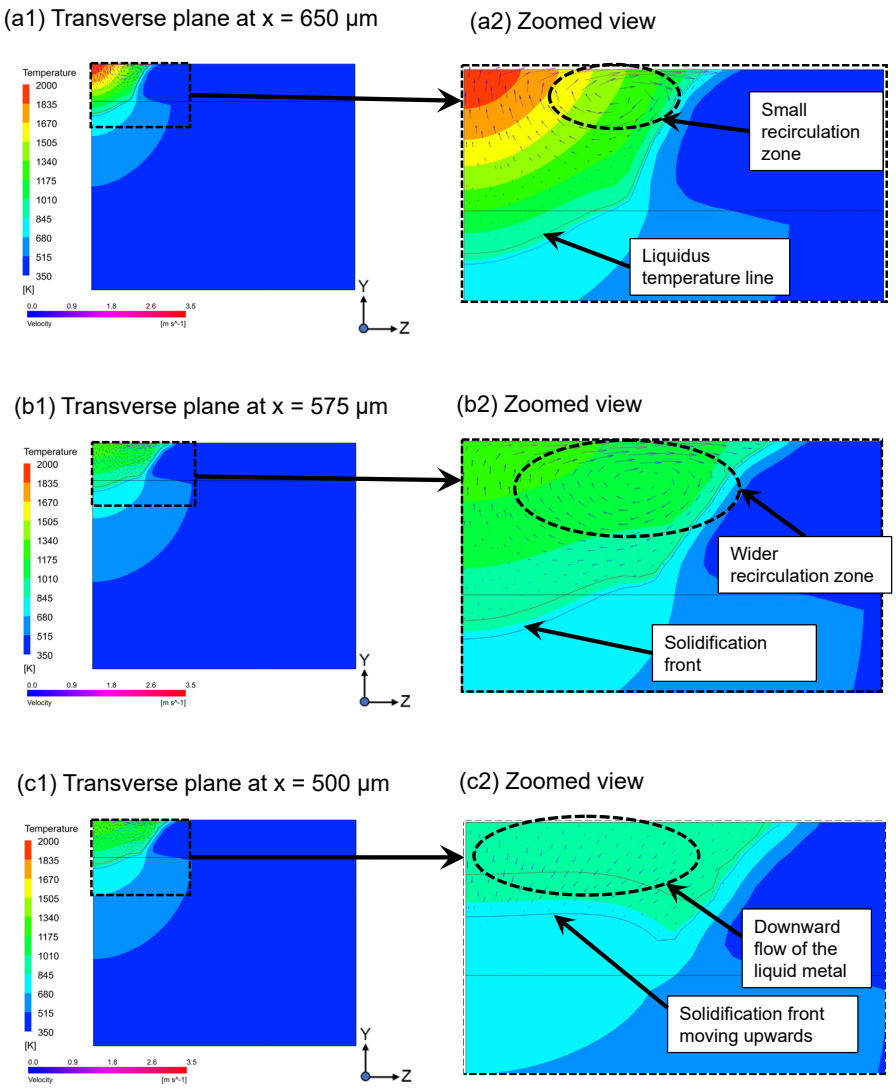


Figure 5.12. Temperature and the tangential velocity field at the selected y-z planes depicted in Fig. 5.11: (a1-a2) Transverse plane at 650 µm, (b1-b2) Transverse plane at 575 µm, and (c1-c2) Transverse plane at 500 µm.

of the molten fluid increases, the natural convection increases due to buoyancy force. In addition, the cooler liquid metal has a higher viscosity compared to hotter liquid metal. Consequently, the magnitude of the molten pool velocity, and hence the strength of the recirculation zone, diminishes where the temperature of the liquid metal is comparatively lower. Therefore, the strength of the recirculation zones is controlled by the Marangoni and the natural convection and the viscosity of the liquid metal.

Nanoparticle Distribution at Transverse Planes

One of the main objectives of the current study was to investigate the nanoparticle transport in the molten pool of the AlSi10Mg alloy matrix. Nanoparticle transport in the molten pool is significantly influenced by the molten fluid velocity field, as stated by Brechet et al. [85]. Two transverse planes were selected in the CFD model to study the nanoparticle transport mechanism and its dependence on the velocity field in the molten pool. These two transverse planes lie in x = 550 μm and 650 μm, earlier shown in Fig. 2.1. Nanoparticle positions were tracked in the cells that coincided with the selected planes. The current CFD model calculated the three dimensional velocity vector field. Therefore, to properly understand the molten fluid flow at a particular transverse plane, 3D velocity vectors acting on that given plane needed to be analyzed. For illustration, the case of 150W laser power, with 500 mm/s scanning speed with a preheated temperature of 100°C, was chosen. Figure 5.13 visually illustrates the process of molten fluid flow and its influence on nanoparticle migration at the time ranging from 1000 μs to 1500 μs. The initial distribution of the TiB_2 nanoparticle was uniform in the powder bed and in the selected planes, which was shown in Fig. 5.1. Figures 5.13 (a1-a12) depict the temperature and velocity field calculated in the entire computational domain. The 3D velocity field acting on the transverse plane

at x = 650 µm is shown in Figs. 5.13 (b1-b12). Figure 5.13 (c1-c12) shows the nanoparticle positions in the front view of the transverse plane with tangential velocity vectors of the associated

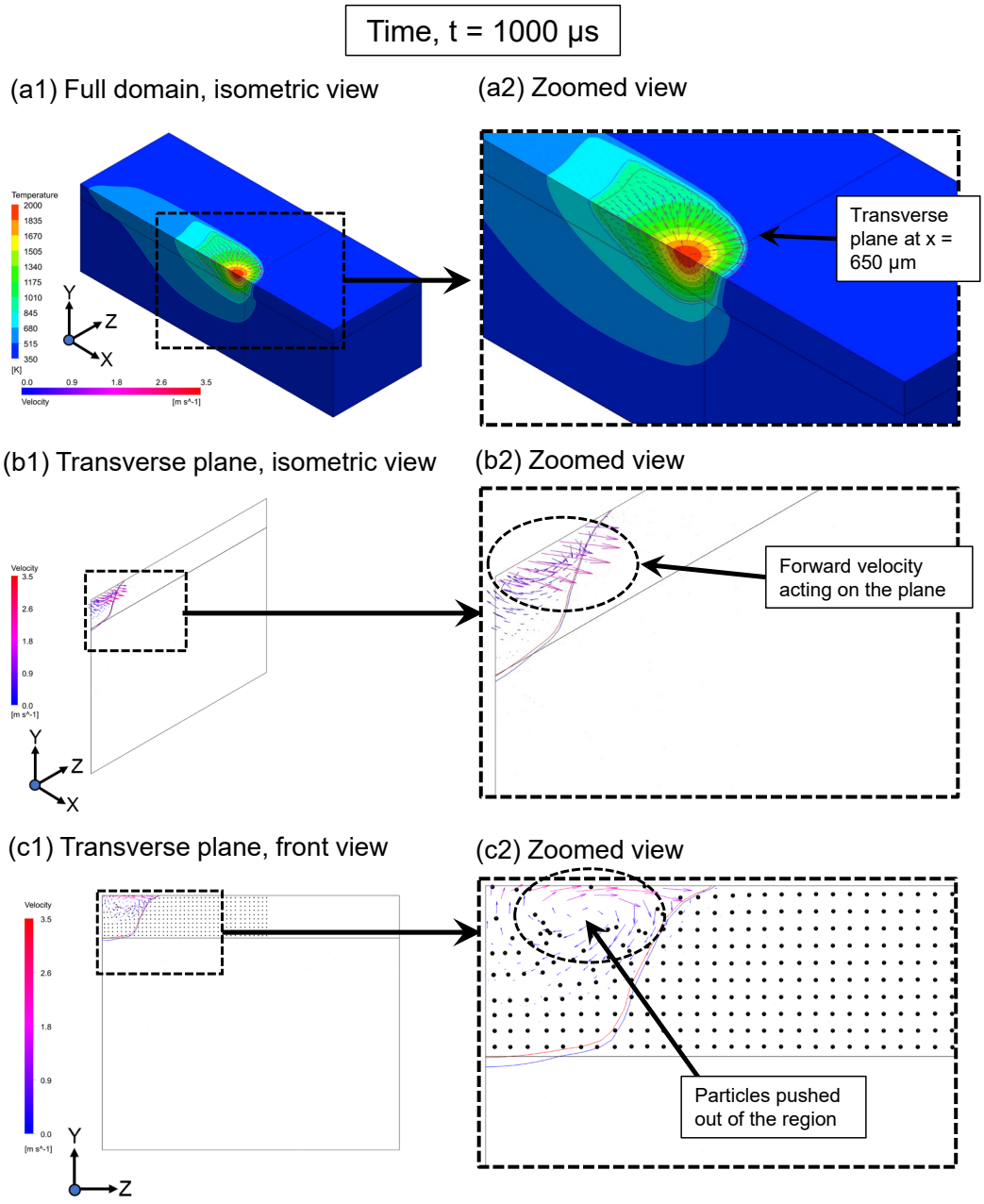


Figure 5.13. Dynamics of nanoparticle transport at a 2D transverse plane: (a1-a12) temperature and velocity in the whole computational domain, (b1-b12) 3D velocity field acting on the transverse plane, (c1-c12) nanoparticle distribution in the transverse plane with the 2D tangential velocity vector of the flow field

Figure 5.13 continued

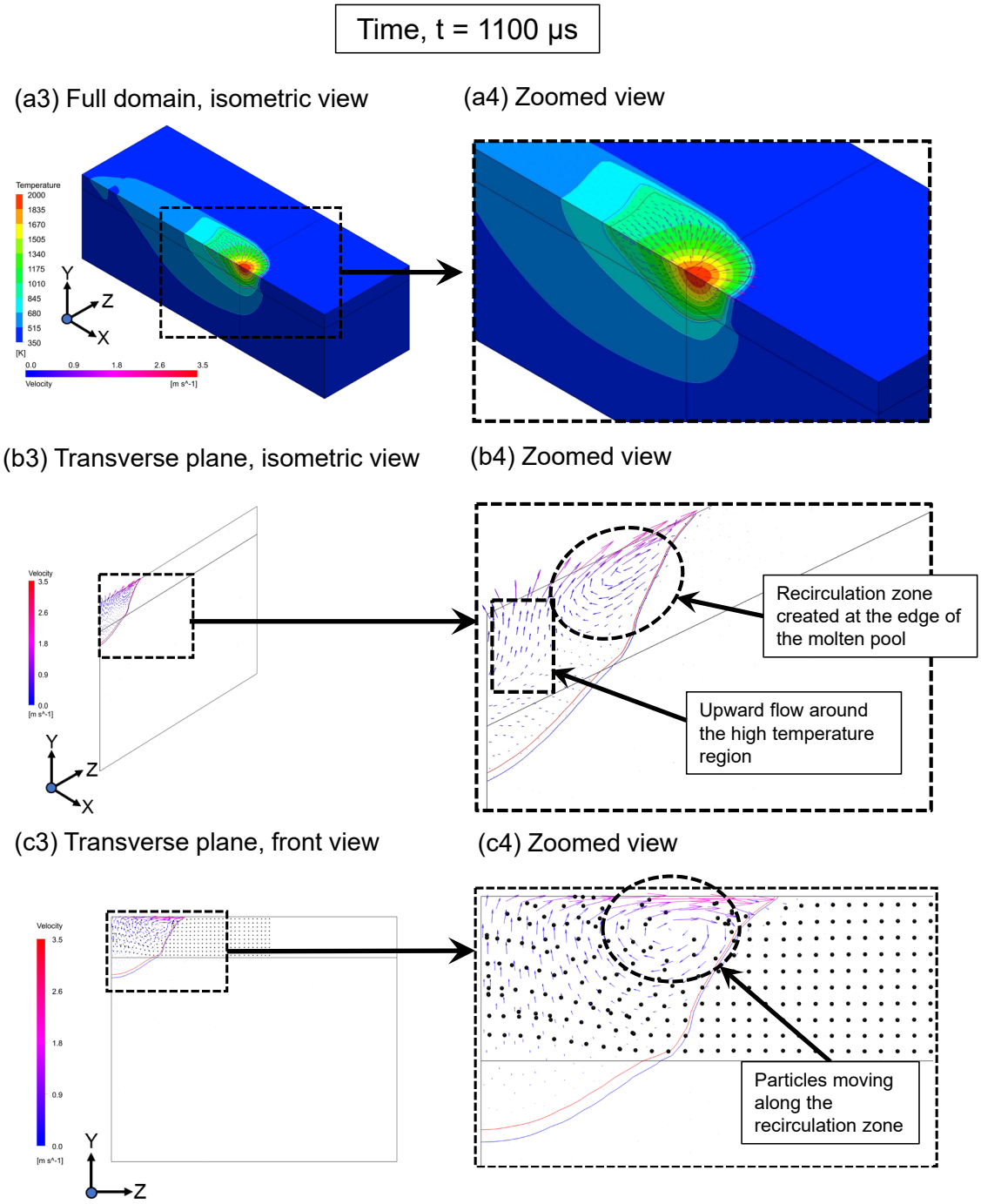


Figure 5.13 continued

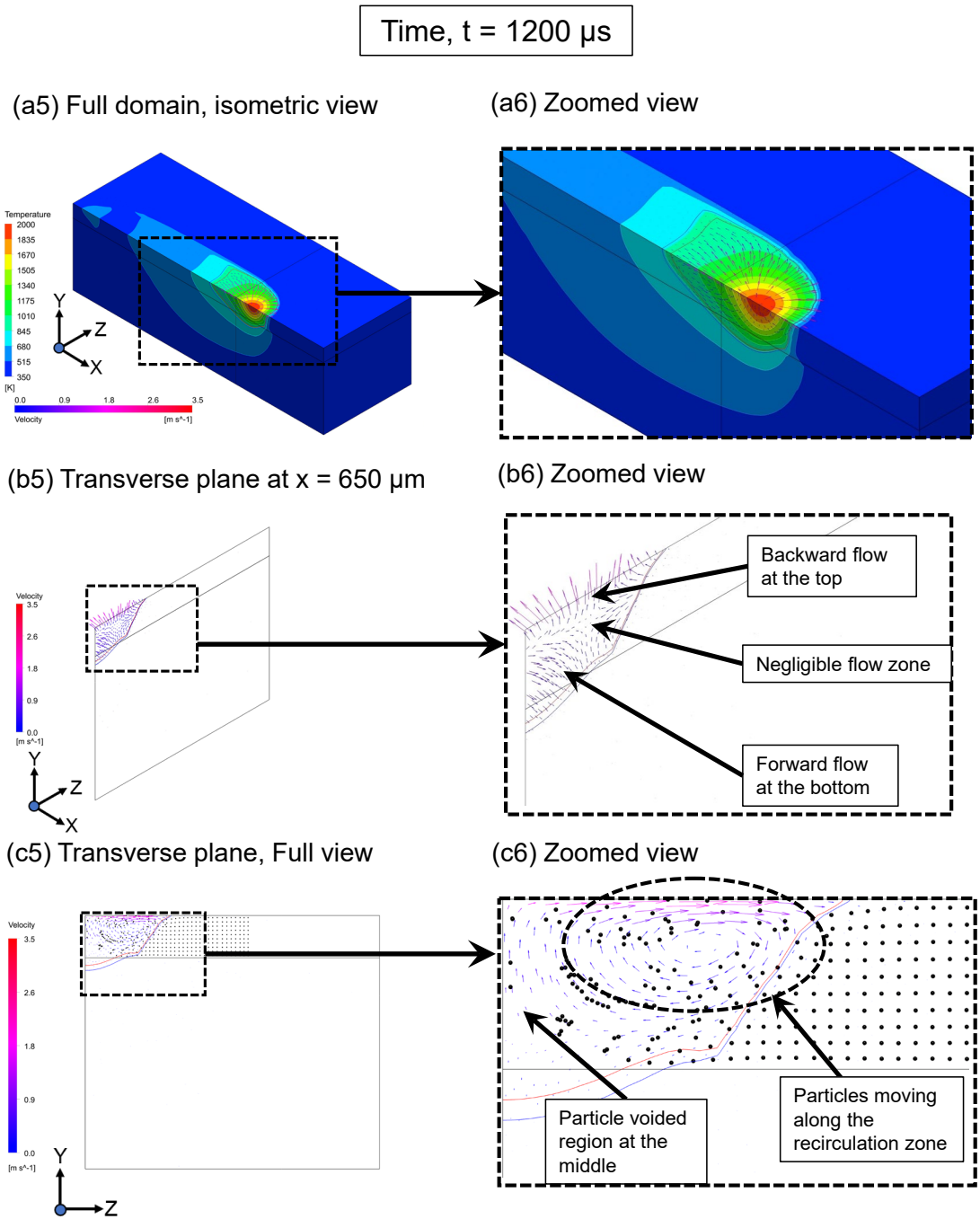


Figure 5.13 continued

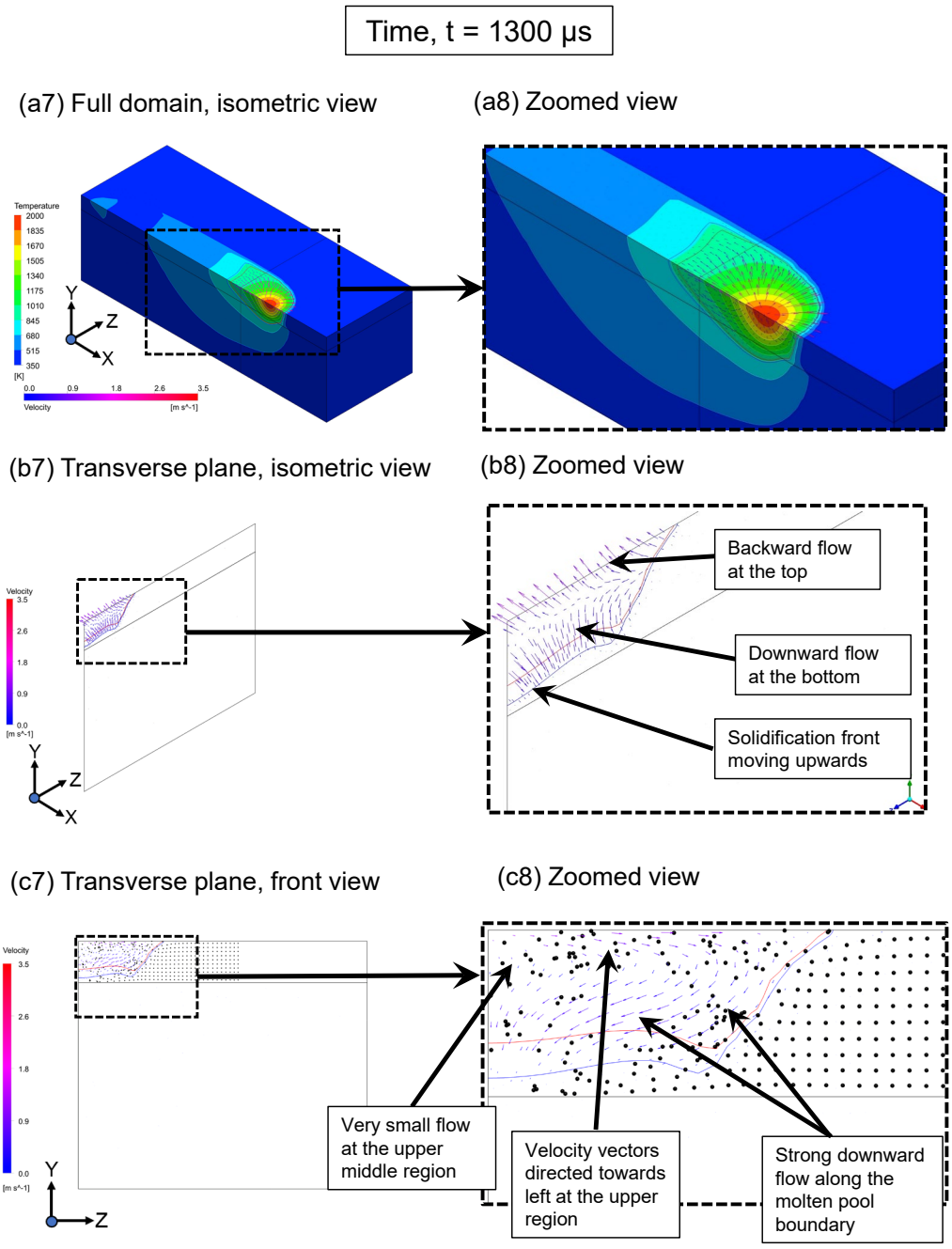


Figure 5.13 continued

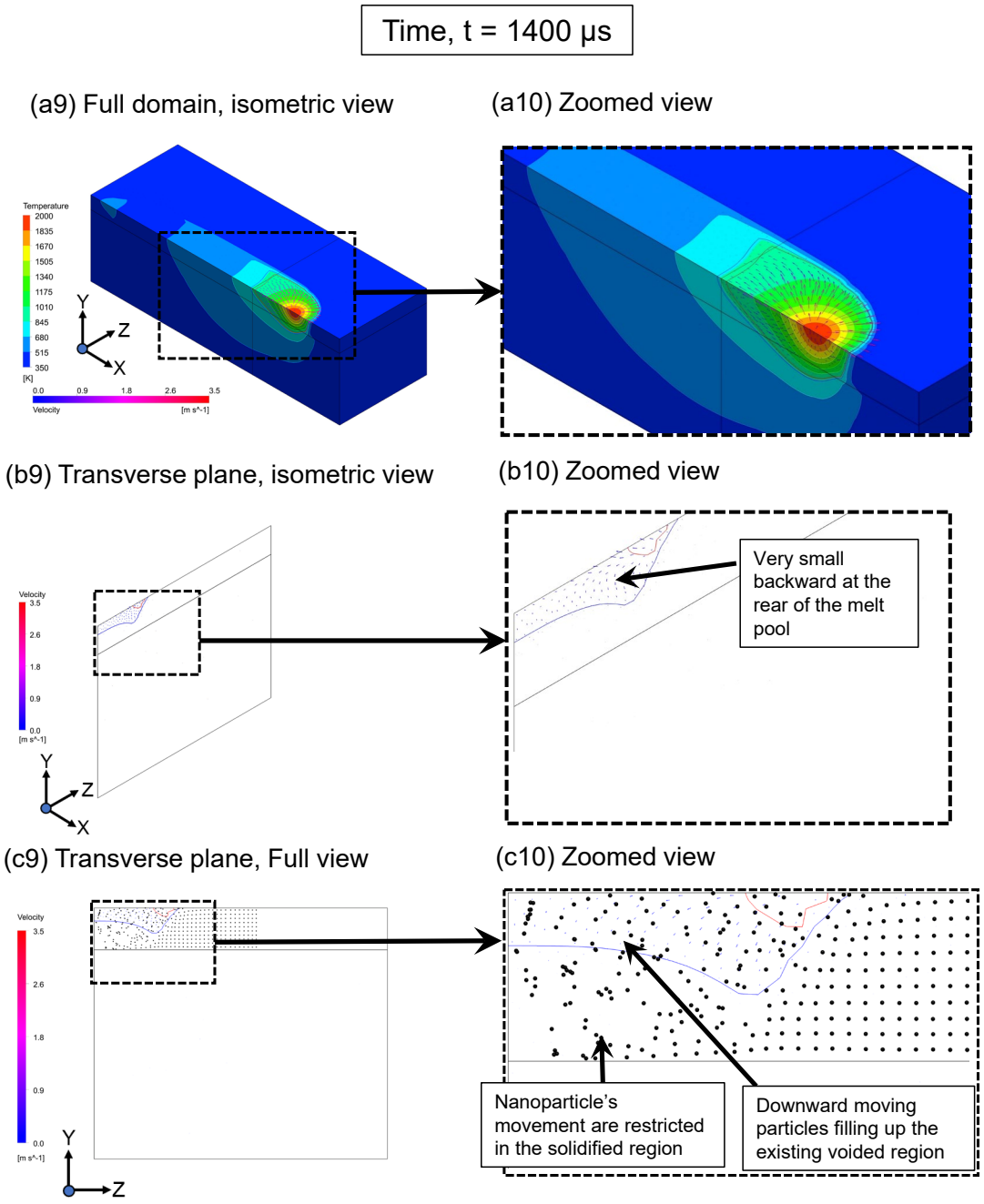
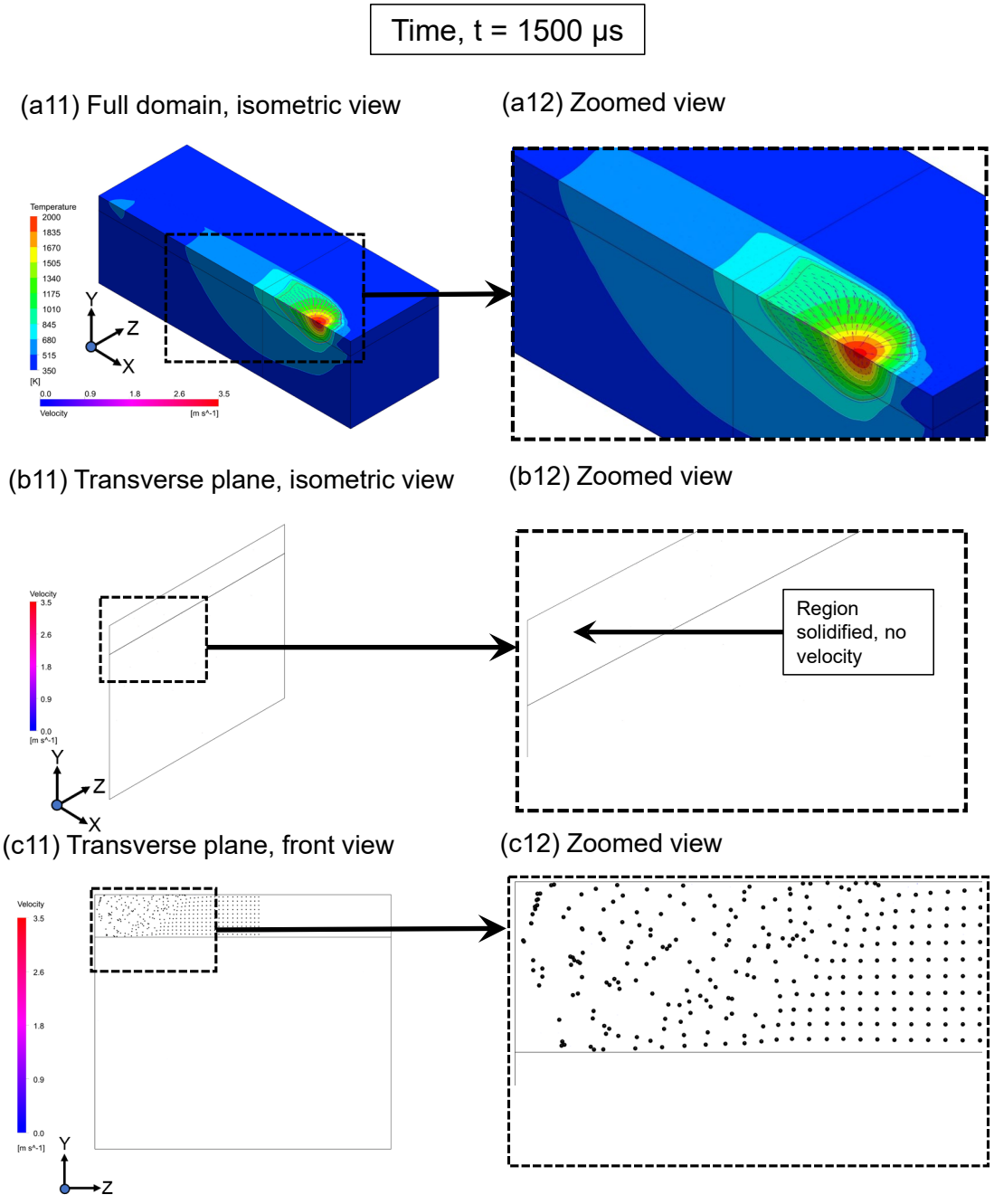


Figure 5.13 continued



flow field. As shown from the figures, at a time of 1000 μs, the transverse plane is located ahead of the high temperature region. The heat flow from the laser-activated region behind the selected plane generates a small melt pool at this plane. As shown earlier in Fig. 5.9 (a), a clockwise rotating flow was present in the molten pool region ahead of the high temperature region. This clockwise rotating flow induces a forward flow in the upper region of the selected plane, acting outward normal to this plane. As a result, the nanoparticles located at this plane are pushed out of the region, as seen in Fig. 5.13 (c1-c2). The molten liquid flow at the bottom part of this 2D plane is very low. Therefore, the nanoparticles' initial positions are undisturbed at that time instant.

At 1100 μs, the transverse plane coincides with the high temperature region, as shown in Figs. 5.13 (a3-a4). The clockwise rotating flow and anti-clockwise rotating flow combine below this high temperature region and, thus, generate an upward flow in the molten pool. As a result, the molten fluid moves upward in the middle region of the transverse plane and carries the nanoparticles with it, as shown in Figs. 5.13 (b3-b4) and (c3-c4). In addition, a strong recirculation zone parallel to the transverse plane is observed at this time instant, impelling the nanoparticle to move along its recirculating flow. It is also evident from Figs. 5.13 (c3-c4) that the nanoparticles are moving along the velocity vectors of the recirculating flow. They are driven out of the center of the recirculating flow by the centrifugal force acting on them.

The transverse plane is positioned at the rear of the high temperature at 1200 μs. The solidification front marked by the solidus temperature line moves upward, indicating solidification occurs from the bottom of the melt pool. As a result, the depth of the molten pool decreases, and its width increases compared to the molten pool dimensions at 1100 μs. The velocity field is dominated by the anti-clockwise flow in this region, as can be seen in Figs. 5.13 (a5-a6). This anti-

clockwise rotating flow stimulates a strong backward flow at the top and a forward flow at the bottom region of the transverse region, depicted in Figs. (b5-b6). Very small velocity magnitudes can be observed between the forward and the backward flow, indicating the region falls in the eye of the anti-clockwise recirculating zone parallel to the symmetric (x-y) plane. As a result, the nanoparticle distribution at that time instant is different from the previous. The backward and the forward flow pushes the nanoparticles out of the transverse plane yielding a nanoparticle-voided region in the middle of the molten region. The tangential velocity directions in the molten pool suggest that a recirculation zone is still active from the middle to the edge of the molten pool. This recirculating flow increases the width of the molten pool. Consequently, the nanoparticles rotate along with the recirculating flow in that region. A particle voided region still exists at the eye of the recirculating flow. The presence of particle voided region at the eye of the recirculating zone can be seen from Figs. (c5-c6).

Figures 5.13 (a7-a8) show that the transverse plane is located further behind the high-temperature region at 1300 μs. The solidification front moves further upward, indicating that more regions from the bottom of the previous molten pool have been solidified. As a result, the depth of the molten pool is shorter than the previous time instant, as can be seen from Figs. 5.13 (b7-a8). Backward flow at the top part and downward flow at the bottom part are evident from these figures. As discussed earlier, this flow pattern is caused by the anti-clockwise recirculating flow parallel to the symmetry plane. The nanoparticle transport is dictated by this flow pattern at this time instant. The nanoparticle voided region observed at last time gets filled with new nanoparticles being carried with this recirculating flow. The recirculation zone, parallel to the transverse plane, becomes wider and weaker than last time, as exhibited in Figs 5.13 (c7-c8). As a result, both the

nanoparticles and the molten pool's width are pushed further to its left edge. From there, the liquid metal moves downward along the solid-liquid interface with the recirculating flow. This downward flow is intensified at the bottom part of this transverse plane, with the backward flow perpendicular to its plane. Therefore, more nanoparticles move downward along the liquidus temperature line at the left of the molten pool boundary. In addition, as shown in Fig. 5.13 (c8), a very small downward flow is observed in the upper middle region, which imparts a slight downward movement to the nanoparticles.

The transverse plane can be seen from Figs. 5.13 (a9-a10) to be positioned at the trailing edge of the molten pool at 1400 μs. A small melt pool distributed along its width in the z-direction is observed in the transverse plane, as depicted in Figs. 5.13 (b9-b10). A very small backward flow is evident at the top part of the transverse plane, as shown in Fig. 5.13 (b9-b10), which carries more nanoparticles to this particular plane. A small downward flow is also exhibited across the transverse plane, pushing the nanoparticles downwards from the top part of the plane. The region captured by the solidification front has no molten pool flow, and thereby nanoparticles' movements are restricted there, as indicated in Figs. (c9-c10). Therefore, the particle voided region created by the flow dynamics at the previous times is filled up with new nanoparticles, creating a local uniform distribution across the transverse plane. At 1500 μs, all the melted region in the transverse plane is solidified, as shown in Figs. 5.13 (a11-a12, b11-b12). As a result, liquid metal flow and the velocity of the nanoparticles become null. The nanoparticle positions shown in Figs. 5.13 (c11-c12) is the final distribution of the nanoparticles at the solidified region.

A uniform local nanoparticle distribution is observed after the complex three-dimensional flow dynamics in the molten pool region. The molten fluid flow is significantly controlled by the

recirculation zones parallel to the symmetry plane acting opposite to each other. Another recirculation zone acting perpendicular to this plane also influences the transport of nanoparticles. Finally, a small nanoparticle-voided region can be seen in the lower middle part of the transverse plane at the solidified region. This can be attributed to the fact that at the trailing edge of the molten pool, the downward flow carrying the nanoparticles from the top to fill up the void space below it was very small. As a result, a relatively higher speed of the upward moving solidification front solidified those voided liquid regions before nanoparticles could reach there. Since the temperature and velocity distribution quickly reaches a quasi-steady state, the same pattern of nanoparticle distribution is observed on the transverse plane located at x = 550 μm. The final distribution of nanoparticles in the solidified regions in the transverse planes at x = 650 um and x = 550 um is exhibited in Fig. 5.14. A local uniform nanoparticle distribution can be observed in the region, which was affected by the 3D molten pool flow. The nanoparticles outside the molten pool boundary remain at their initial positions since those regions were solid. During setting up the model, the liquid and solid phase of the material was differentiated by setting up different dynamic viscosities. A high mushy zone constant of 10^8 was used to restrict the flow in the solid region. As a result, The positons of the nanoparticles were unaffected in the regions where melting did not occur. In the melted region, nanoparticles were redistributed, and the same distribution pattern was observed for the transverse plane at x = 650 μm and x = 550 μm. However, a slight difference can be observed in local nanoparticle distribution in some parts across the transverse plane. Random Brownian force was considered in the particle transport model, which significantly affects the nanoparticles' migration behavior apart from the velocity flow field. This resulted in some differences in final nanoparticle positions in the solidified region.

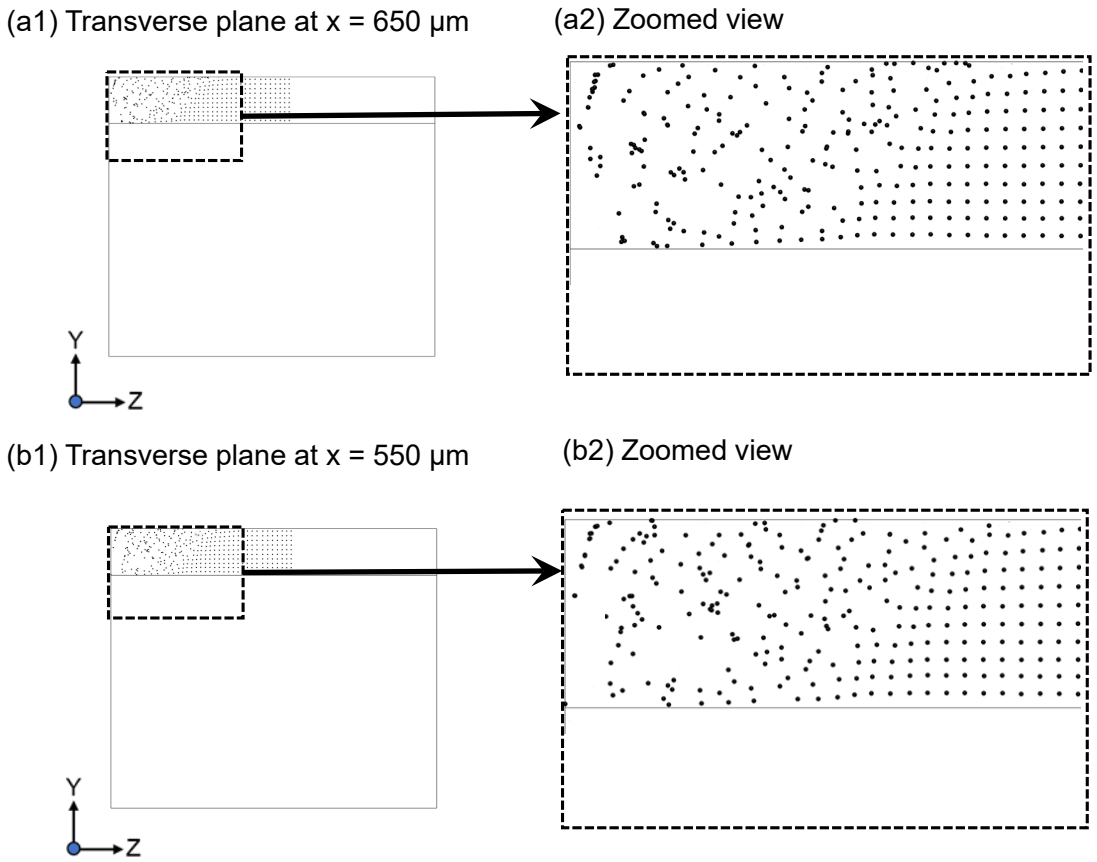


Figure 5.14. Final nanoparticle distribution in the transverse planes: (a1-a2) x = 650 µm, (b1-b2) x = 550 µm for 150 W laser power moving at 500 mm/s scanning speed.

Solidification Parameters and Microstructure Evolution in Transverse plane

Microstructure formation was simulated using a 2D Cellular Automata (CA) model. The temperature history, the local temperature gradient, and final nanoparticle distribution calculated from the current CFD model were incorporated into the CA model. Two transverse planes at x = 650 and 550 µm were selected to analyze microstructure evolution during the melting and solidification of AlSi10Mg alloy caused by a moving laser heat source. A detailed workflow of coupling the CFD model into the CA model was described in “Coupling of CFD and CA model”

in Chapter 4. However, the solidification parameters such as temperature gradient, cooling rate, and solidification rate directly influence the microstructure's morphology and shape in the solidified region. These solidification parameters can be determined from the temperature field and its history. Therefore, these solidification parameters are required to be analyzed before understanding the microstructure evolution during the solidification process.

Calculation of Solidification Parameters

The temperature gradient (G) and the cooling rate ($\dot{T}$) at the solid-liquid interface vary spatially across the depth of the molten pool. The temperature gradient was calculated from the thickness of the mushy zone from an interval of 10 μm from the melt pool surface. As shown in Fig. 5.15, these data points are referred to as data probing points. Probing data points lie along the intersection of the symmetric plane and transverse plane until the molten pool boundary. The temperature gradient G, was calculated using the following equation:

$$G = \frac{T_L - T_S}{y_L - y_S} \tag{5.1}$$

where, $(T_L - T_S)$ is the difference between the liquidus and solidus temperature of AlSi10Mg and $(y_L - y_S)$ is the mushy zone thickness along the y-axis where y_L lies on the selected probe point. The data was taken when the selected probing points coincided with the liquidus temperature isotherm. During solidification, the liquidus temperature line moves upward from the molten pool boundary in the transverse plane, as shown in figure 5.15. This same approach to calculating temperature gradient was taken by Kohnen et al. [86]. The cooling rate was calculated from the temperature history, tracking when the liquidus and solidus temperature lines reached the probing points [87]. The following equation was used to calculate the cooling rate during solidification:

$$(\dot{T}) = \frac{T_L - T_S}{t_L - t_S} \tag{5.2}$$

where, $T_L - T_S$ is the difference between the liquidus and solidus temperature of AlSi10Mg and $(t_L - t_S)$ is the interval between the time required for the solidus and liquidus temperature to reach a particular probe point.

Figure 5.15 (a) shows the thermal gradient and the cooling rate at the selected probe points depicted in 5.15 (b). The powder bed line parting the powder bed and the substrate lies at 50 μm from the top wall, as shown in Fig. 5.15(b). The depth of the probe points from the top wall lies on the horizontal axis of the plot. The thermal gradient is shown on the left vertical axis, whereas the cooling rate is depicted on the right vertical axis of the plot. A very high thermal gradient and the cooling rate are calculated at the solid-liquid interface, at the order of 10^6 and 10^5, respectively. The figure further describes that higher temperature gradients and cooling rates are observed at the solid-liquid interface at the beginning of the solidification. As the solid-liquid interface moves upwards toward the molten pool surface during solidification, both the thermal gradient and the cooling rate decrease. However, the cooling rate increases again when the solid-liquid interface is at a distance of 30 μm from the top wall. This phenomenon suggests that the cooling rate was very high when the solidification front was located in the substrate region, where the material's thermal conductivity was very high. As the solidification front moves into the powder bed region, the molten liquid boundary is surrounded by powder particles with very low thermal conductivity. As a result, the heat can not be diffused well in those places and yields a relatively lower cooling rate. The cooling rate increases again as the solidification front moves closer to the surface of the molten pool, where the heat diffusion rate is prominent because of Marangoni convection. The Marangoni

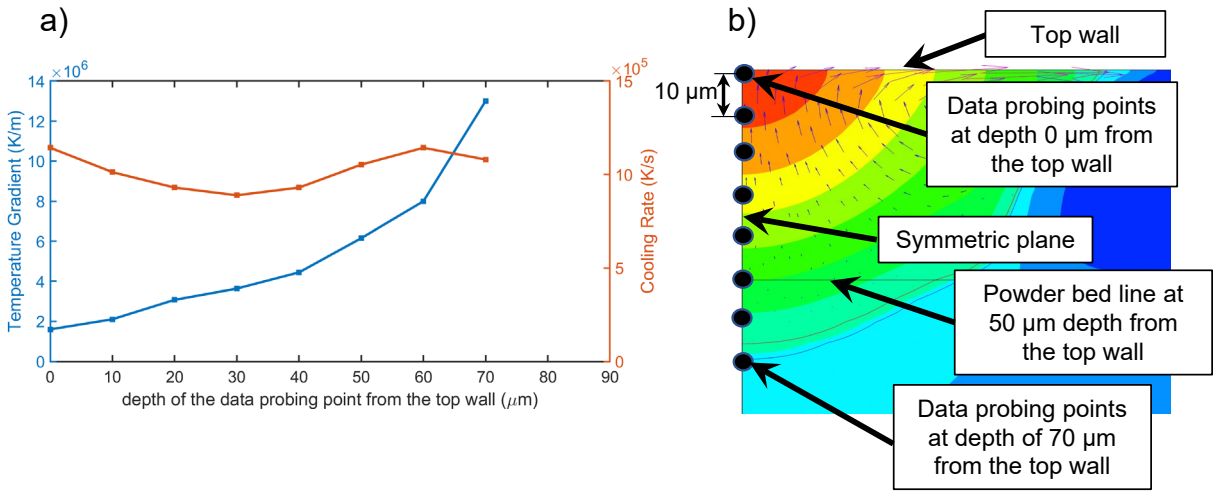


Figure 5.15. (a) Plot of the thermal gradient and cooling rate along the respective probing points of the molten pool at a transverse plane, and (b) representative data probing points from the front view of the transverse plane.

convection diffuses the heat from the center of the molten pool radially outwards to its edge. In addition, heat losses due to convection and radiation to the ambient surroundings occur at the top surface, increasing the cooling rate. The continuous decrease in the thermal gradient as the solidification front moves closer to the surface of the molten pool indicates that the thickness of the mushy zone increases along with it. As the laser heat source moves further away from the transverse plane, the maximum temperature of the top surface decreases. This was evident in Fig. 5.12, where the temperature and velocity distribution of a transverse plane due to moving laser heat source with the increase of time was described earlier in this section. With the decrease of maximum temperature at the top surface, the temperature gradient at the solidification front decreases, resulting in an increase in the mushy zone's thickness.

Microstructure Evolution by The Cellular Automata Model

The present Cellular Automata (CA) model predicted the microstructure evolution by simulating the melting and solidification phenomena during the selective laser melting process. The

temperature distribution, local thermal gradient history, and the final nanoparticle distribution found from the CFD model were one way coupled with the CA model. The coupling of the CA model with the CFD model was earlier described in chapter 4. Figure 5.16 describes the melting process simulated by the current CA model for selective laser melting by 150 W laser power moving at 500 mm/s. The powder bed and substrate were preheated to 373 K for this case. This is the same case described earlier in this chapter to explore the temperature and velocity distribution at different times at a transverse plane during the SLM process. The initial microstructure is shown in Fig. 5.16 (a), where the powder region has a smaller grain size than the substrate region. It is evident from this figure that the grains are randomly oriented between -45° to 45° with respect to the y-axis. The grain orientations represent the crystallographic orientation of the aluminum alloy in a 2D plane. Further information regarding grain orientations in the current CA model was described in chapter four. As the laser heat source moves closer to the transverse plane, the powder region starts melting, as shown in Fig. 5.16 (b). The white region in the figure represents the molten pool, and the blue and red curves, respectively, represent the liquidus and the solidus temperature line. The melting process continues at 1100 μs, increasing the molten pool's width and depth. The depth and the width of this molten pool are the same as the molten pool dimensions calculated from the CFD model.

The microstructure evolution during the solidification process at the transverse plane at x = 650 μm is shown in Figs. 5.17 (a1-a4) and (b1-b4). Figures 5.17 (a1-a4) exhibit the microstructure formation without considering the final distribution of the nanoparticles, whereas Figs. 5.17 (b1-b4) shows the microstructure evolution considering the final distribution of the nanoparticles in the same figure. The nanoparticles acted as impurities during the solidification of

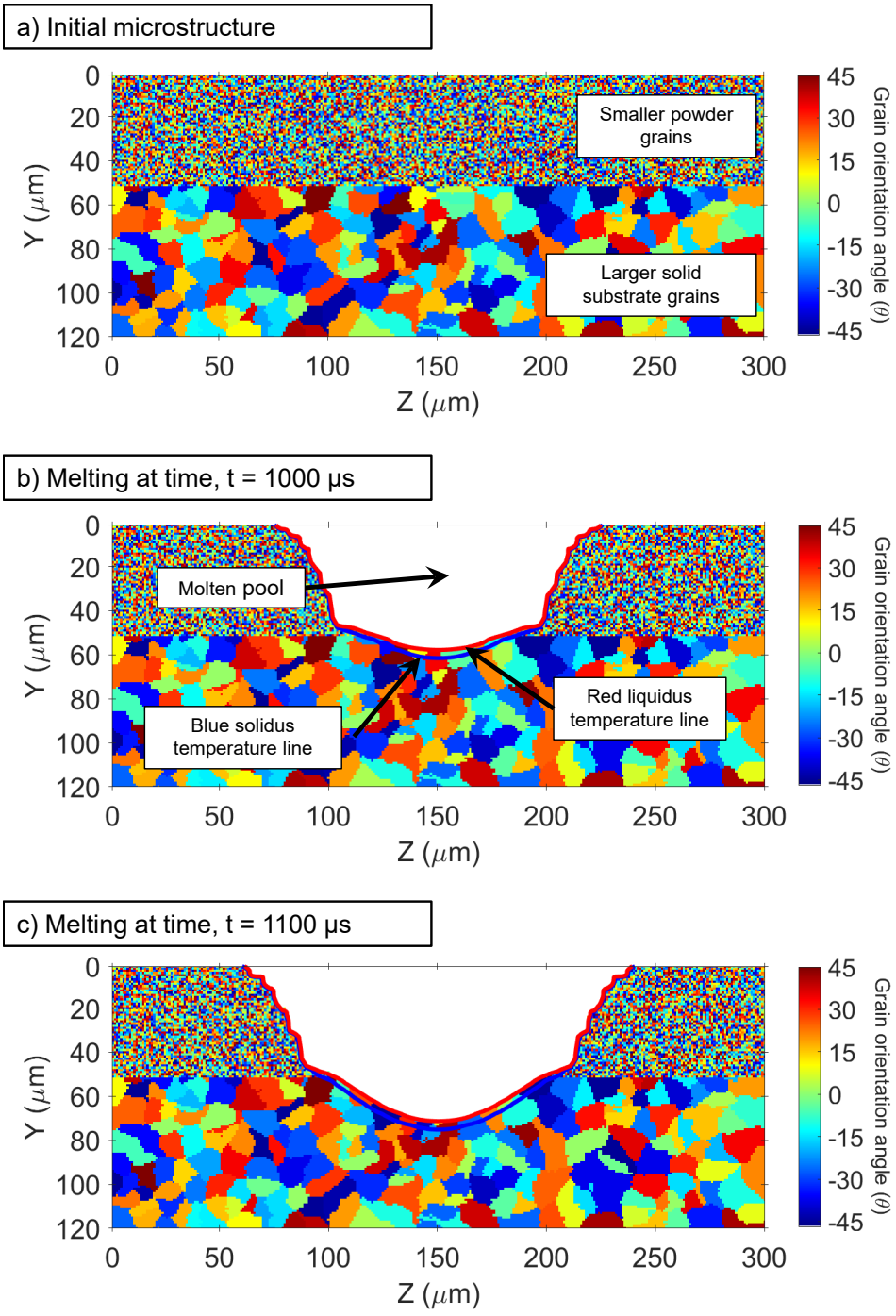


Figure 5.16. Simulation of melting process by the current Cellular Automata model: (a) initial microstructure, (b) melting of microstructures at1000 μs, and (c) melting of microstructures at 1100 μs.

the aluminum alloy matrix, thus increasing grain nucleation, as observed by Martin et al. [49]. In the current CA model, the final distribution of nanoparticles acted as nucleating cells, increasing bulk nucleation in the CA domain. Therefore, the bulk nucleation density was very high in the cases (b1-b4) compared to the cases (a1-a4) where nanoparticles were not considered. As discussed earlier in chapter 4, while coupling the CFD model computed nanoparticle distribution into the CA domain, the in and out-of-plane transport of the nanoparticles in the 2D transverse plane was not considered. The in and out-of-plane migration of the nanoparticles were described in Fig. 5.13. Only the final positions of nanoparticles were considered after the liquid metal solidified. It was assumed that the velocities of the nanoparticles were negligible when solidification occurred during the microstructure simulation by the current CA model.

At the beginning of the solidification process, the temperature gradient and cooling rate at the solid-liquid interface are very high, yielding a low mushy zone thickness. New grains start to grow from the bottom of the molten pool boundary once the temperature drops below the liquidus temperature. Partially melted grains in those regions act as a source of grain nucleation, inheriting their orientation to the newly formed grains. The grain growth process was modeled using the "modified decentered polygon" algorithm described earlier in the "Grain Growth Modeling" section of chapter 4. The grain growth from partially melted grains, defined as epitaxial growth, is evident in both Figs. 5.17 (a1) and (b1). As the same temperature and thermal gradient history were coupled in those cases, the mushy zone thickness is the same for both figures. As the solidification progresses, the new solidified grains grow along the local temperature gradient directions, perpendicular to the liquidus and solidus temperature isotherm, as illustrated in Figs. 5.17 (a2) and (b2). The plot depicted in Fig. 5.15 described that the thermal gradient decreased

and the cooling rate increased as the solidification front moved upward in the powder bed region. The same phenomenon is observed at 1300 µs for the CA simulated microstructure. A decrease in thermal gradient with a high cooling rate, increases the thickness of the mushy zone from the previous time step. Since the cooling rate is high, the solidification front's velocity can not keep up with the liquidus temperature isotherm. Hence, undercooled liquid metal exists between the liquidus temperature line and the solidified grains. This undercooled liquid region can nucleate new grains by the bulk nucleation mechanism.

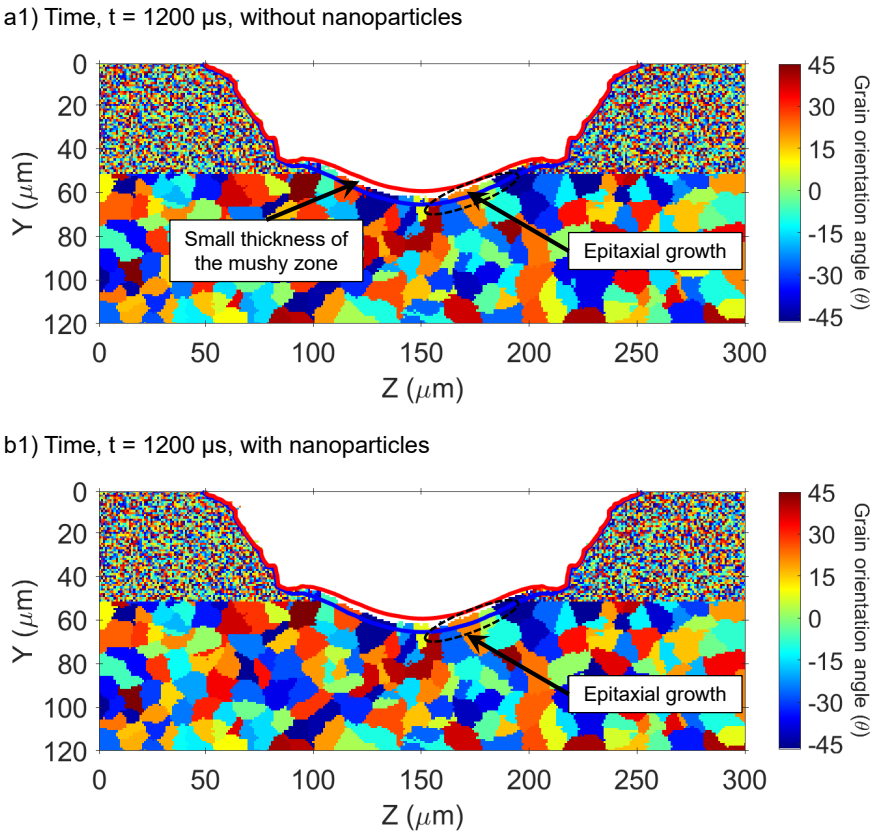
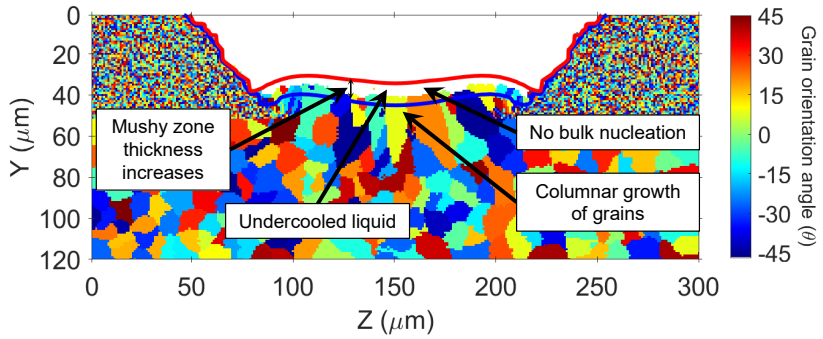


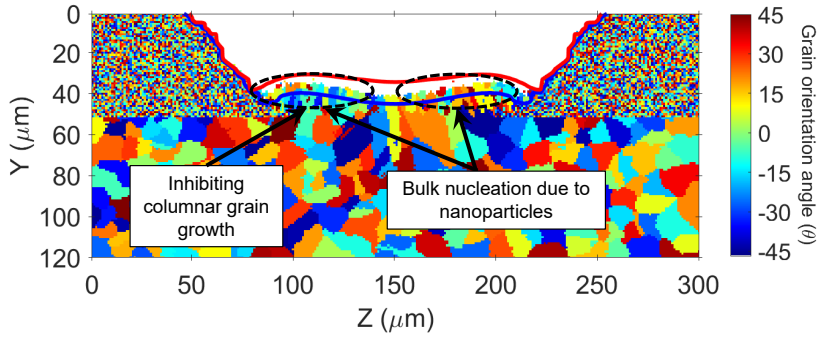
Figure 5.17. Microstructure evolution by 2D Cellular automata model at specific time steps: (a1-a4) without considering nanoparticles, and (b1-b4) considering nanoparticles in the CA domain.

Figure 5.17 continued

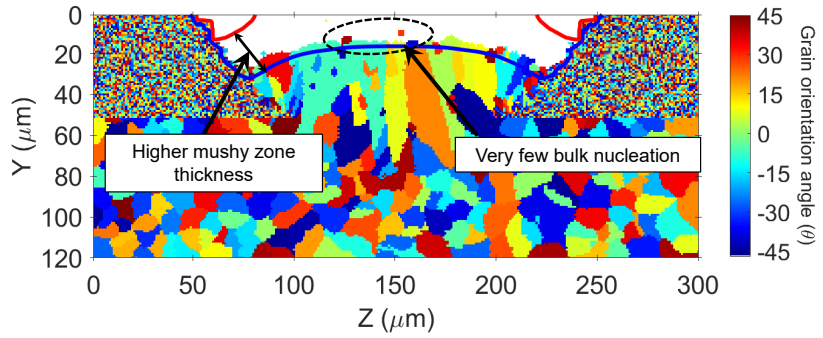
a2) Time, t = 1300 μs, without nanoparticles



b2) Time, t = 1300 μs, with nanoparticles



a3) Time, t = 1400 μs, without nanoparticles



b3) Time, t = 1400 μs, with nanoparticles

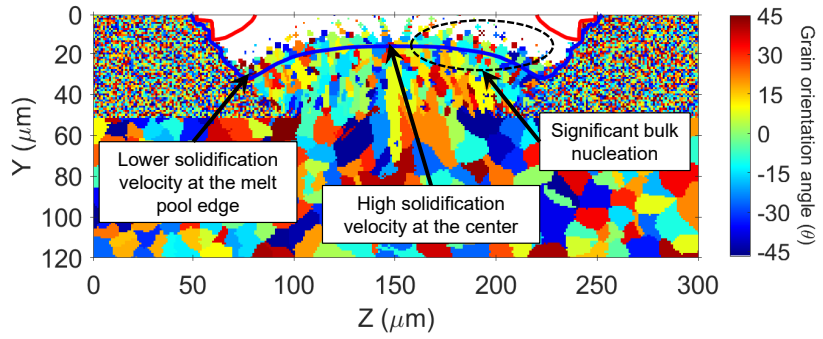
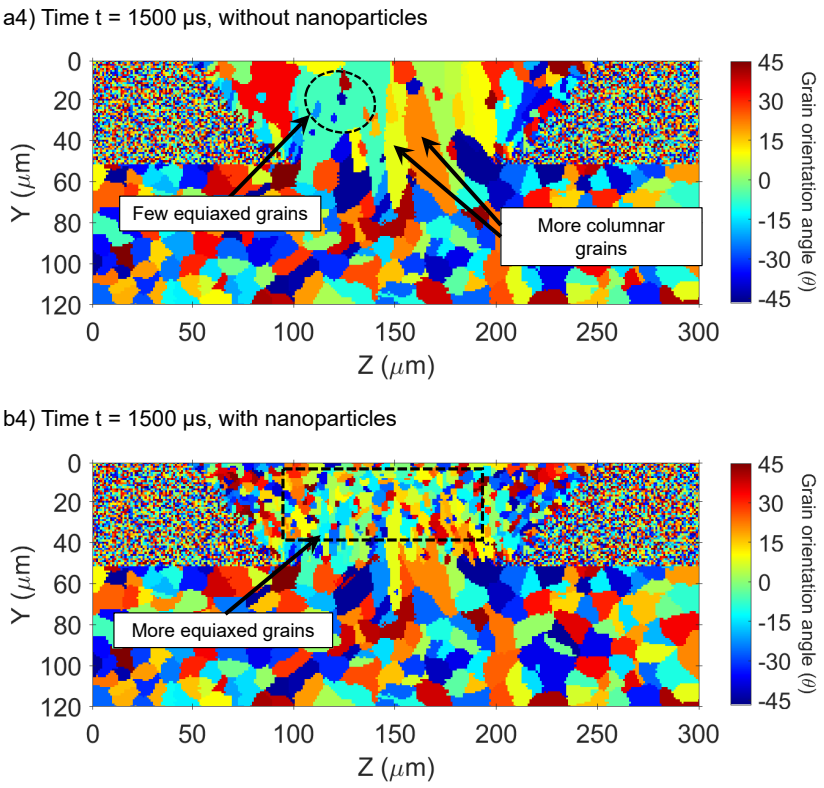


Figure 5.17 continued



In the current CA model, undercooled liquid nucleated new grains if the current undercooling is higher than the critical undercooling of the randomly selected nucleating cells. The bulk nucleation model is detailed earlier in the "Nucleation Modeling" section of chapter 4. In Fig. 5.17 (a2), since nanoparticles are not incorporated in this case, the probability of bulk nucleation is very low, yielding no bulk nucleation at 1300 μs. Conversely, in the case where nanoparticles act as bulk nucleation sources, new grains nucleate in the undercooled liquid, as shown in Fig. 5.17 (b2). The figure further illustrates that these new grains formed ahead of the columnar grains inhibit the columnar growth during solidification.

The thickness of the mushy zone increases significantly as the solidification front moves closer to the molten pool surface. A lower temperature gradient associated with a higher cooling

rate yields a large undercooled liquid region. This large undercooled liquid region is suitable for forming new grains ahead of the columnar grains. As a result, bulk nucleation forms small equiaxed grains at 1400 μs in Fig. 5.17 (a3). This bulk nucleation phenomenon is significant in the case considering nanoparticle distribution, as shown in Fig. 5.17 (b3). The grains nucleated by adding nanoparticles have random orientations, promoting the formation of a fine equiaxed region. At 1500 μs, after the entire region is solidified, the number of equiaxed grains is significantly higher for the case with nanoparticles, as shown in Fig. (b4). However, Fig. 5.17 (a4) shows a few equiaxed grains in the microstructure, as grain nucleation was significantly low. The formation of fine equiaxed regions in the microstructure increases the tensile strength of the products manufactured by selective laser melting (SLM) [49]. The columnar grains directed to the local temperature gradient direction show anisotropic mechanical behaviour in the fabricated part. However, fine equiaxed regions reduce anisotropy in the mechanical properties of the manufactured product by inhibiting columnar grain growth [7]. Therefore, the formation of fine equiaxed regions is desired in the SLM process, and adding nanoparticles can facilitate growth for equiaxed grains, as observed in Fig. 5.17. Grain sizes for these two cases were measured by the mean lineal intercept method described in ASTM E-1382 standard [84] and tabulated in Table 5.4. Due to increased nucleation by the nanoparticles, the average grain diameter decreased in the transverse plane by 40%.

Table 5.4. Average Grain diameter comparison for 150 W laser power, 500 mm/s scanning speed, preheated at 100°C.

Case	Without considering nanoparticles (μm)	Considering nanoparticles (μm)	Decrease in average grain diameter
Average grain diameter	12.1	7.3	40%

Using the current CA model, the microstructure was simulated at the transverse planes at x = 550 μm and 650 μm for 150 W laser power moving at 500 mm/s scanning speed. Figure 5.18 (a1, a2) shows the microstructure simulated at x = 550 μm and (b1,b2) shows the microstructure simulated at x = 650 μm. A black curve shows the final molten pool boundary marking the melted and solidified region in these figures. The same microstructural features can be observed qualitatively for the simulated microstructure irrespective of the plane in these figures. Both the simulated microstructures' images without the nanoparticles show that the columnar grains are oriented to the local temperature gradient. Columnar grains are predominant in the solidified regions, though small equiaxed grains can be seen. The location and orientation of the bulk nucleated grains are randomly selected, which imparts some local differences in the predicted microstructure at two different planes. This is also evident from Fig. 5.18 (a2, b2) that overall features at two different planes are the same, though some local difference exists due to the probabilistic nature of the CA simulation. Epitaxial growth is observed at the beginning of the solidification at the molten pool boundary in both cases. More epitaxial growth is observed at the molten pool boundary with the powder bed region. Since the powder grain size is small in the powder bed region, more partially melted powder grains are in contact with the molten pool boundary. Consequently, they result in more epitaxial growth of grains during solidification. As the solidification progresses, the thickness of the mushy zone increases due to a lower thermal gradient. The thick mushy zone yields bulk nucleation of the cells holding nanoparticles inside it. Therefore, the upper part is dominated by randomly oriented equiaxed grains for the predicted microstructure in both transverse planes.

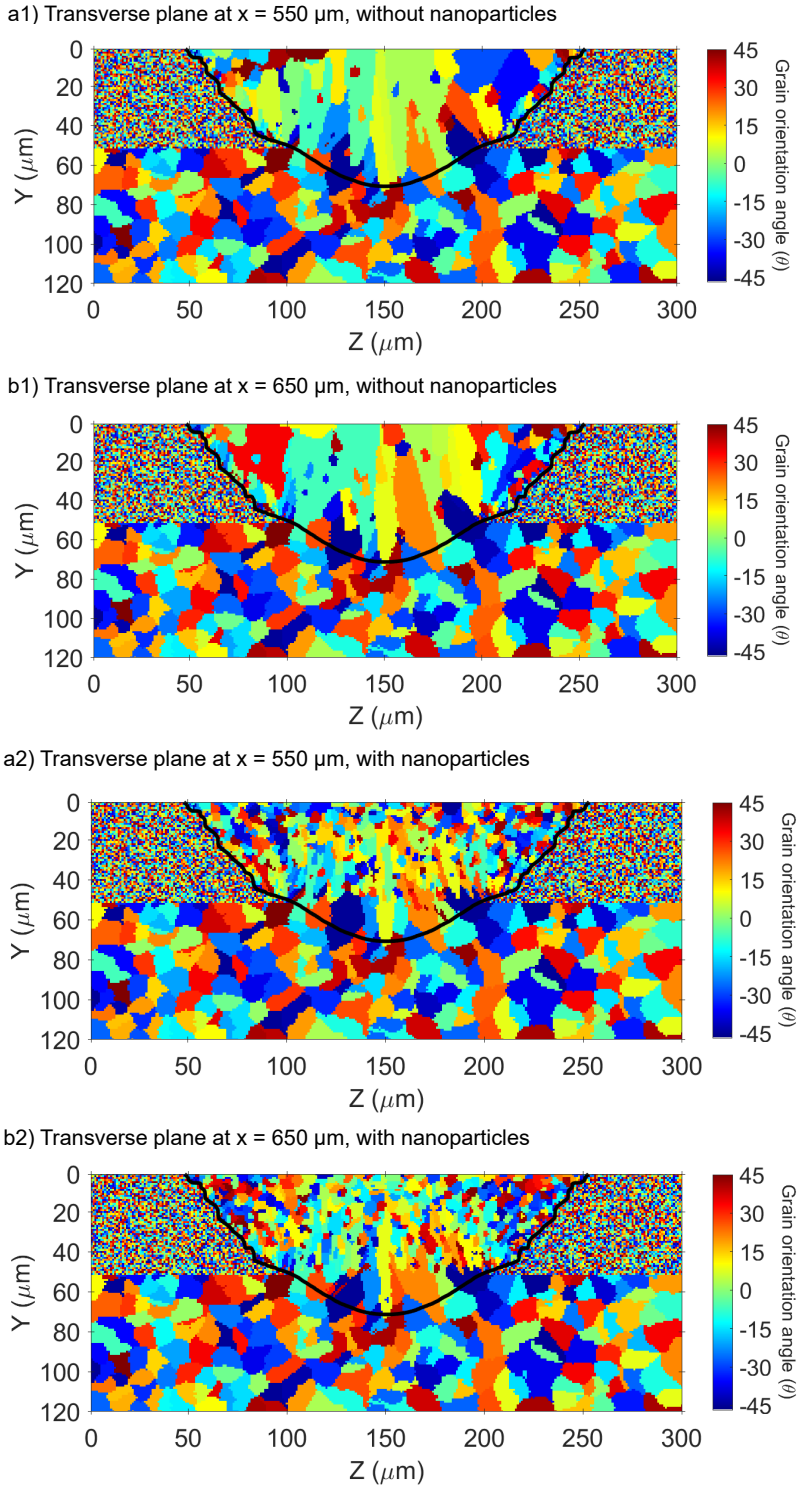


Figure 5.18. Microstructures simulated by the current CA model at two different planes: (a1-a2) simulated microstructures at transverse plane x = 550 μm and (b1-b2) simulated microstructures at transverse plane x = 650 μm.

Effect of Laser Scanning Speed

Temperature and Velocity Distribution

In the selective laser melting process, the temperature distribution was affected by the heat exerted by the moving laser heat source and the heat transfer by the previous laser-activated region. Figure 5.19 shows the histories of the maximum temperature on the top surface of the powder bed and the temperature of P1 and P2 for different laser scanning speeds. In the figure, the laser

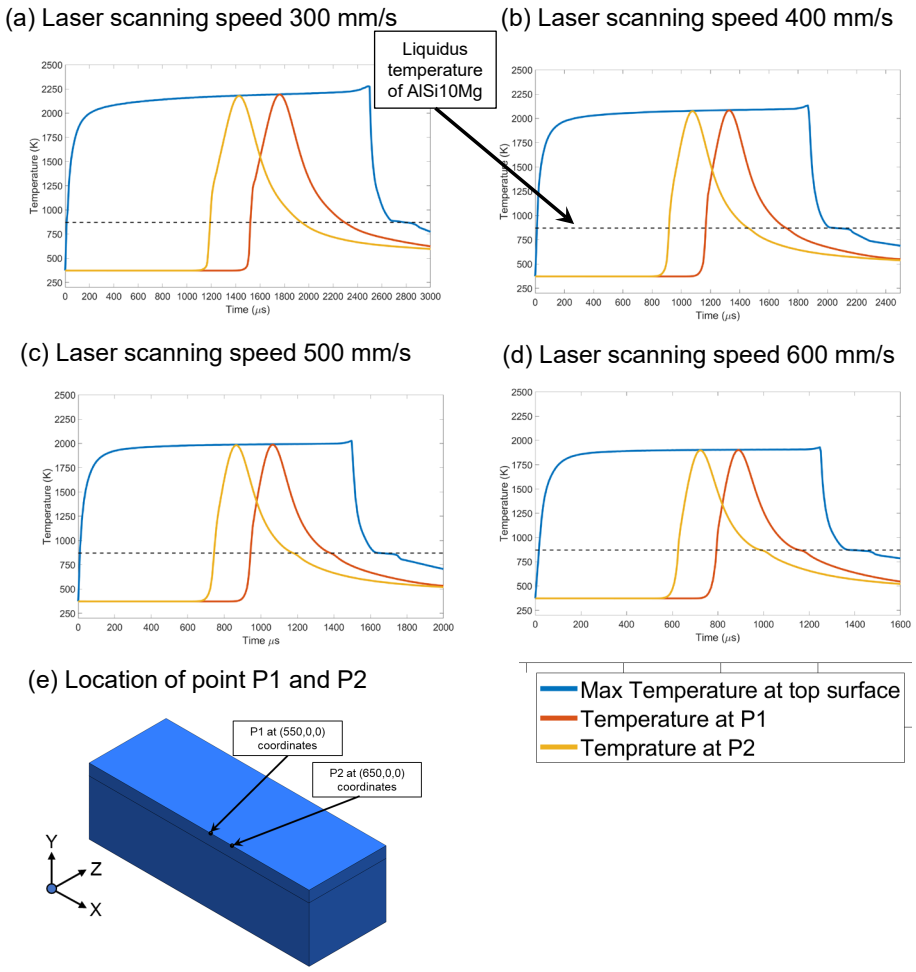


Figure 5.19. Variation of temperature histories of the maximum temperature and representative P1 and P2 points on the top surface: (a) 300 mm/s laser scanning speed, (b) 400 mm/s laser scanning speed, (c) 500 mm/s laser scanning speed, (d) 600 mm/s laser scanning speed, (e) location of representative points P1 and P2.

scanning speed is increased from 300 mm/s to 600 mm/s in 100 mm/s increment. The laser power is kept constant at 150 W, and the powder bed and substrate are preheated to 373 K for all these cases. The figures illustrate that the maximum temperature quickly rises from the preheating temperature of 373 K to a maximum stable temperature for all these cases. At higher scanning speeds, the active time of the laser in a fixed position reduces. As a result, the net amount of heat input by the laser decreases with increasing laser scanning speed. This results in a lower maximum temperature at the top surface. For example, the maximum temperature reaches a stable maximum temperature of 2200 K for a laser scanning speed of 300 mm/s, as shown in Fig. 5.19 (a). In contrast, the maximum temperature drops to 1900 K for a higher scanning speed of 600 mm/s, shown in Fig. 5.19 (d). The peak temperatures of points P1 and P2 also decrease with the increase of laser scanning speed, as depicted in Figs. 5.19 (a-d).

As shown in Fig. 5.20, the temperature distribution and the resulting molten pool dimensions are affected by the change in laser scanning speed. At 300 mm/s scanning speed, a wider and deeper high temperature region is observed around the laser spot center. The high temperature region is depicted in dark red in the figures and indicates a temperature higher than 2000 K. The volume of the high temperature region decreases at 400 mm/s, and at laser scanning speed higher than that dark red colored zone disappears. Instead, a lighter red color zone, indicating a temperature range of 1835 to 2000 K, can be observed as the high temperature region for laser scanning speeds of 500 mm/s and 600 mm/s, as shown in Figs. 5.20 (c1-c2, d1-d2). When the region's temperature reaches beyond the temperature of the liquidus temperature line, a melted region is created. The molten pool region is defined by the region bounded by the liquidus temperature line in Figs. 5.20 (a1-a2).

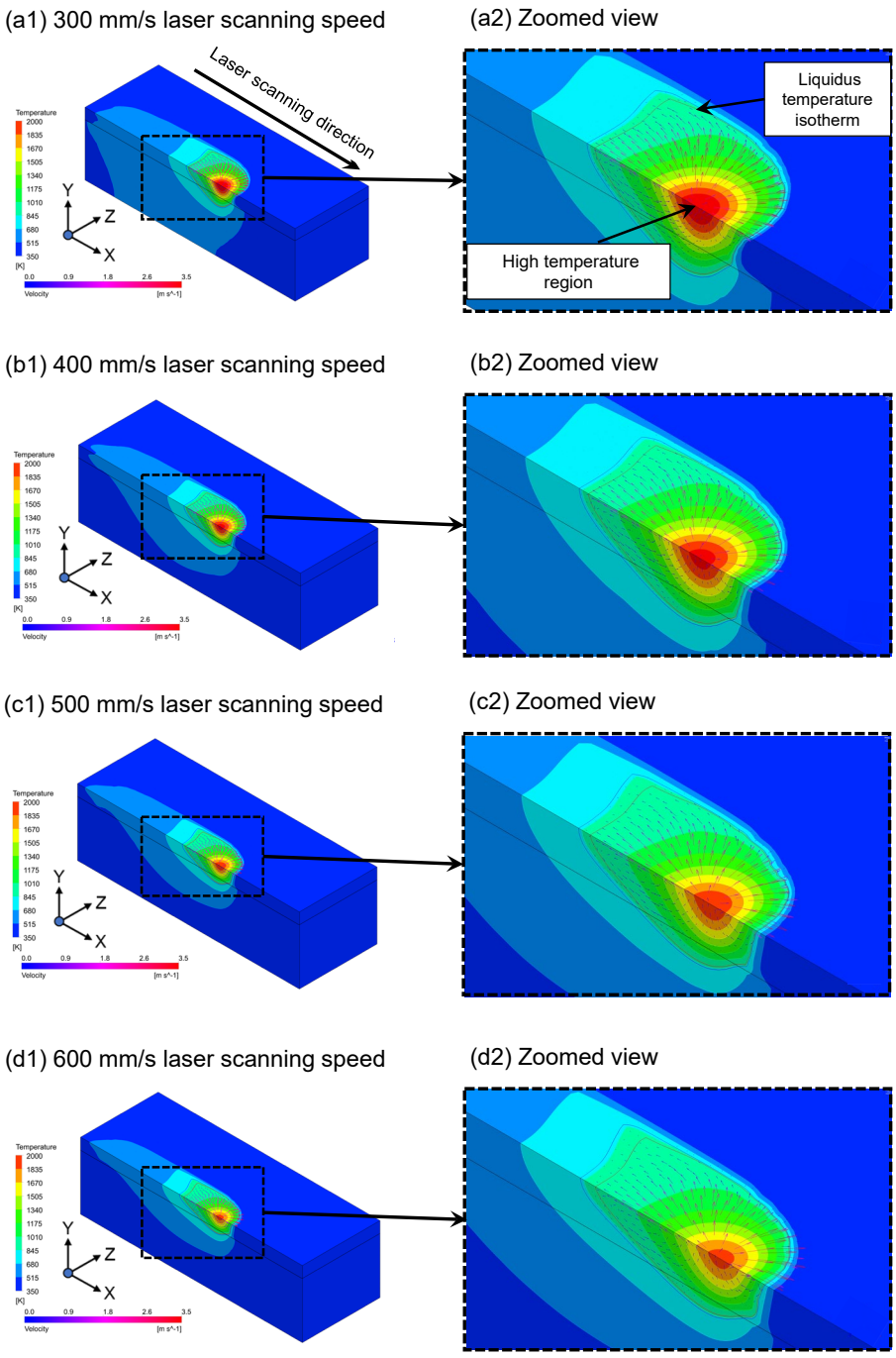


Figure 5.20. Temperature and velocity distribution due to variation of laser scanning speed: (a) 300 mm/s laser scanning speed, (b) 400 mm/s laser scanning speed, (c) 500 mm/s laser scanning speed, (d) 600 mm/s laser scanning speed.

A radially outward flow is observed from the center of the highest temperature region to the molten pool boundary for these cases due to Marangoni convection at the top surface. As described earlier, in Fig. 5.8, the molten pool velocity was very low at the center of the highest temperature region because of a lower temperature gradient. In addition, the molten pool velocity was also low because of increased viscous effects at the molten pool boundary. However, the magnitudes of velocity vectors increased and then decreased in the intermediate region between the center of the highest temperature region towards the molten pool boundary. The relative strength of the flow field due to varying laser scan speed depends on the Marangoni convection on the top surface of the liquid molten pool. Therefore, the Marangoni number associated with the molten pool was calculated using Eq. 2.19. and compared with the variation of laser scanning speed. The change in Marangoni number for the variation of laser scanning speed is shown in Fig. 5.21. The plot illustrates that the Marangoni number is significantly high at 634 at a scanning speed of 300 mm/s. In contrast, the Marangoni number is low at 328 for a scanning speed of 600 mm/s. Marangoni number of the flow field is proportional to the maximum temperature and inversely proportional to the viscosity of the fluid. In the current CFD model, the viscosity of the liquid metal was calculated based on the temperature of the fluid using Eq. 2.17. At a higher temperature, the viscosity of the liquid metal decreased. Due to a higher maximum temperature and lower viscosity of the liquid metal, the Marangoni number is very high for 300 mm/s laser scanning speed. A higher Marangoni number indicates that the Marangoni convection at the top surface is higher. As a result, the velocity of the liquid metal in the intermediate region of the molten pool is high for 300 mm/s laser scanning speed and is shown in Fig. 5.20 (a1-a2). The higher magnitudes of the velocity vector are represented by the longer arrows and darker red color in the figure.

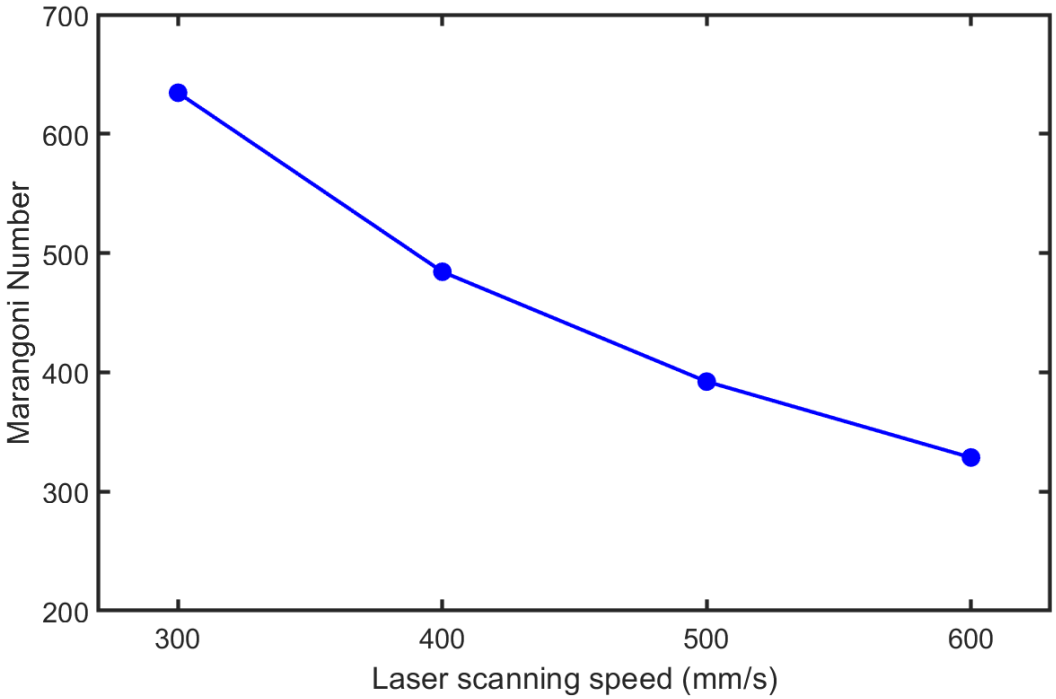


Figure 5.21. Variation of Marangoni number with the change of laser scanning speed.

Figure 5.22 shows the resulting molten pool dimensions created by the laser heat source moving at different scanning speeds. The width, depth, and height of the molten pool were defined earlier in this chapter. The dimensions of the molten pool are affected by the amount of heat absorbed by the powder bed and the associated Marangoni convection. The powder bed absorbs more heat along its depth at a lower scanning speed than at higher laser scanning speeds. At a lower scanning speed, strong Marangoni convection convects more heat from the center of the high-temperature region to its sides. Therefore, the width and depth of the molten pool increase significantly with the decrease of laser scanning speed and are shown in Fig. 5.22. However, the length of the molten pool does not vary much while increasing laser scanning speed from 300 mm/s to 600 mm/s. This is because the region behind the molten pool tail is already solidified and

has very high thermal conductivity, as described earlier in Fig. 5.3. As a result, the tail region of the molten pool boundary quickly solidifies by conducting heat to the rear solidified region. This phenomenon results in a constant length for the molten pools generated for the varying laser scanning speeds.

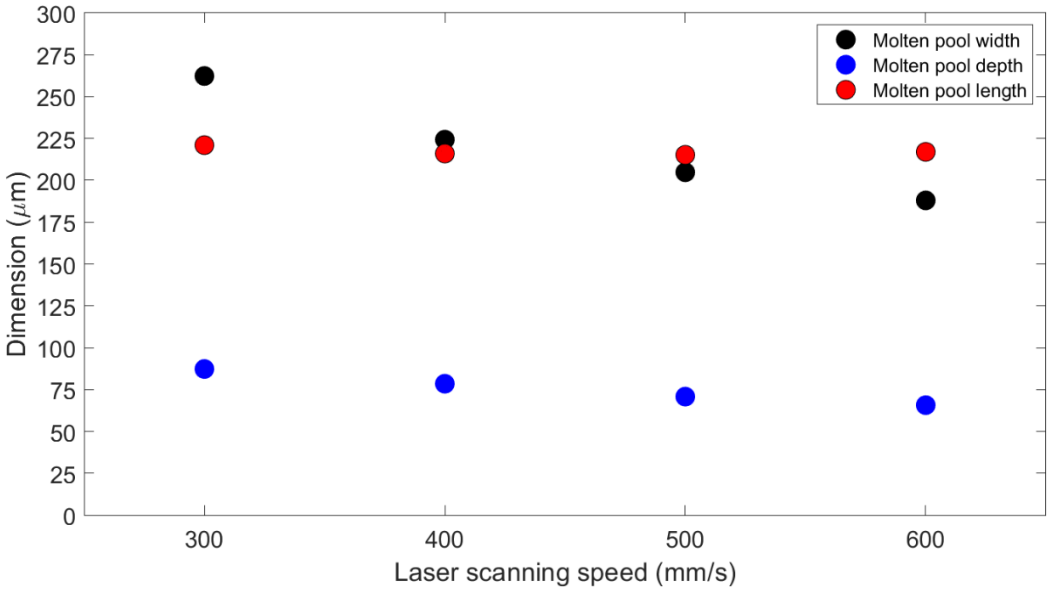


Figure 5.22. Variation of molten pool dimensions with the change of laser scanning speed.

Nanoparticles Distribution at the transverse plane

Nanoparticle distribution in a transverse plane is primarily controlled by the instantaneous change of tangential velocity field during solidification, which was illustrated earlier in Fig 5.13. As shown earlier in Fig. 5.13 (b5-b6), when the transverse plane was located behind the high temperature region, an anti-clockwise rotating flow parallel to the symmetric plane acted on the transverse plane. This flow pattern created a strong backward flow at the top of the transverse plane and a weak forward flow in the lower region of the molten pool. The backward flow drove

new nanoparticles into the plane, while the forward flow pushed the nanoparticles out of the transverse plane. In addition, a negligible flow zone was observed between the forward and the backward flow in the middle of the transverse plane. Another recirculation zone parallel to the transverse plane accompanied this rotating flow. Their combined effect was represented by the tangential velocity field along the transverse plane in Fig. 5.13 (c5-c6). The figure showed that nanoparticles were driven along the velocity vectors of the recirculation zone. In addition, the nanoparticles were pushed out of the center of the recirculation zone by centrifugal force acting on them. As the solidification of the transverse plane continued, the tangential velocity vector field in the transverse plane changed from the last time and was shown in Fig. 5.13 (c7-c8). The figure showed that in the upper region, velocity vectors were directed to the left, which pushed the nanoparticles to the left edge of the molten pool boundary. A downward flow velocity was observed in the transverse plane along the molten pool boundary, which pushed the nanoparticles downwards from the top. The magnitude of the downward flow was higher in the lower left and the lower middle region along the molten pool boundary. Here, the middle region is referred to as the region near the symmetric plane. In the upper middle region, a very small downward flow was observed along the transverse plane. Nanoparticles followed these velocity vectors of the transverse plane until the upward moving solidification front restricted its movement. The final distribution of the nanoparticles can be explained from this general physics, accompanied by comparing the relative strength of the flow field at different laser scanning speeds. Figure 5.23 shows the nanoparticle distribution for varying laser scanning speeds at a transverse plane of x = 650 μm. The laser power was kept constant at 150 W laser power, and the entire domain was preheated to 373 K. Figure 5.23 (a1-a2) shows the final nanoparticle distribution in the solidified

region for a laser scanning speed of 300 mm/s. As illustrated in the figures, a large particle voided region is observed in region “A”. This was caused by a wider recirculation zone parallel to the transverse plane during the solidification of the transverse plane. The nanoparticles were pushed out of the center of the recirculation zone and were driven along the velocity vectors. Marangoni convection was higher at this laser scanning speed because of the higher Marangoni number shown in Fig. 5.21. As a result, the velocity vectors in the recirculation zone were very strong and pushed the nanoparticles further to the edge of the molten pool. As shown in Fig. 5.23 (a2) A local nanoparticle-dense region can be seen in region “B”. The velocity flow is minimal in that region and hence formed this nanoparticle-dense region. The molten pool depth was high for this laser scanning speed which is shown in Fig 5.22. As discussed earlier that during solidification, downward velocity vectors along the molten pool boundary were strong. The nanoparticles were also pushed downwards towards the molten pool depth. Therefore, some particles are located below the powder bed line and indicated by region “C” in Fig. 5.23 (a2). In the same figure, a small voided region is observed in region “D”. The downward directed flow from region “B” was very small during the final stages of solidification. Thereby, this downward flow could not fill up the void in region “D” with nanoparticles before the upward moving solidification front restricted the movement of the flow field.

Figure 5.23 (b1-b2) shows the final nanoparticle distributions for the laser scanning speed of 400 mm/s. A small particle voided region “E” can be seen in Fig. 5.23 (a1-a2). Since the Marangoni convection was weaker for this scanning speed, the strength of the recirculation zone was relatively weaker compared to the previous case. As a result, a smaller particle voided region was created when particles were pushed out of the center of the recirculation zone by the

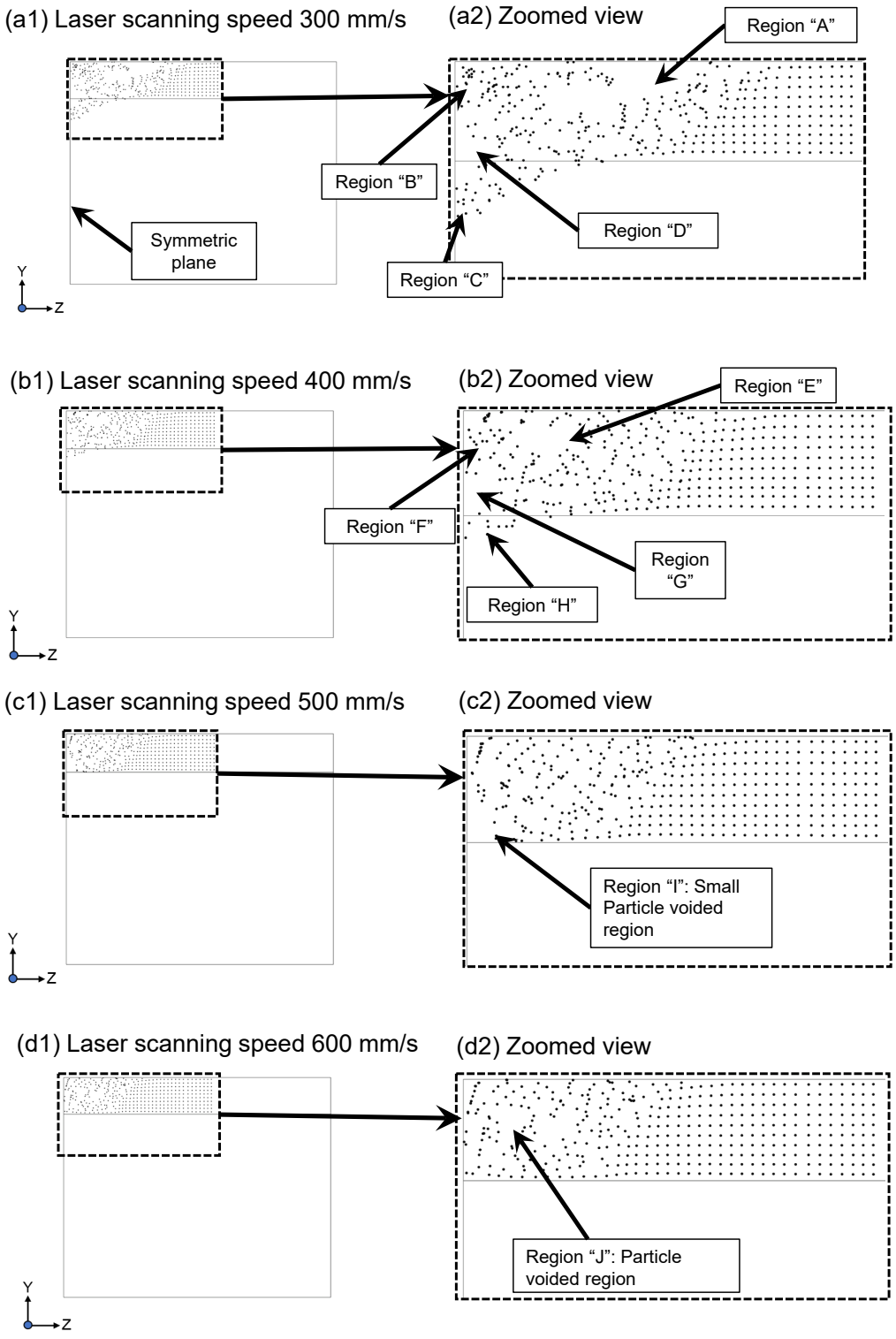


Figure 5.23. Final nanoparticle distribution in solidified region due variation of laser scanning speed: (a1-a2) 300 mm/s laser scanning speed, (b1-b2) 400 mm/s laser scanning speed, (c1-c2) 500 mm/s laser scanning speed, (d1-d2) 600 mm/s laser scanning speed.

centrifugal force. A particle dense region is observed in region “F” in Fig. (b2) because of a low molten pool velocity in that region. The low downward directed flow can not push enough nanoparticles from the top to fill up the voided region below it before the region solidifies. Therefore, a small voided region is observed in region “F”. In addition, very few particles are below the powder bed line indicated by region “H”. This is because of lower molten pool depth below the powder bed line and lower downward push along the molten pool boundary. It can be observed that the particle void regions are smaller for 400 mm/s than the particle void regions seen for 300 mm/s in Fig. 5.23 (a2). It can be inferred that the void regions are reduced at lower Marangoni convection.

Figures 5.23 (c1-c2) and (d1-d2) show the nanoparticle distribution at the transverse plane at x = 650 μm for the laser scanning speeds of 500 mm/s and 600 mms/s, respectively. For higher laser scanning speeds of 500 mm/s and 600 mm/s, as the Marangoni convection is weakened, the particle voided region at the top part of the transverse plane has disappeared. A local uniform nanoparticle distribution was observed in the solidified regions for these cases. Though a small particle voided region was observed in region “I” in Fig. (c2) and region “J” in Fig. (d2). This is because of the higher solidification rate solidifies those regions from the bottom faster before nanoparticles are pushed from the top.

Microstructure Evolution

Microstructure evolution in a transverse was predicted using the Cellular Automata model described in chapter 4 for varying laser scanning speeds. The laser power was kept constant at 150 W, and the entire domain was preheated to 373 K for this parametric study. These cases are the same for which the nanoparticles distributions at a transverse plane are shown in the previous

section. The calculated temperature and local temperature gradient variables for the transverse plane were imported into the 2D Cellular Automata (CA) model. Two different types of microstructures were simulated for each transverse plane:

1) Considering the bulk nucleation effects of the nanoparticles in the 2D CA domain

2) Without considering the bulk nucleation effects of the nanoparticles.

For the first type of microstructure simulation, the final nanoparticle distribution along the selected 2D transverse plane was incorporated into the model. The final nanoparticle distribution was calculated from the computational fluid dynamics (CFD) model. The final distribution of the nanoparticles was not incorporated into the CA domain for the second type of simulated microstructures. The effects of the local distribution of nanoparticles in the first type of simulated microstructures were compared with the second type both qualitatively and quantitatively in this parametric study. The same initial microstructure was used in this parametric study which was depicted earlier in Fig. 5.16 (b). Figures 5.24 (a-d) show the second type of simulated microstructures mentioned earlier for varying laser scan speeds from 300 mm/s to 600 mm/s. The color bar shows the grain orientations with the y-axis, ranging from -45° to 45°. The black curve shown in the figure marks the final melt pool boundary. The region above the black curve was melted by the moving laser heat source and resolidified when it moved away. As can be seen from the figures, large columnar grains predominated the microstructures irrespective of the laser scanning speeds. These columnar grains grow from the final melt pool boundary during solidification by the epitaxial growth. The epitaxial growth occurred from the partially melted grains at the molten pool boundary, and its mechanism was illustrated earlier in Fig. 5.17 (a1). Since powder grains are smaller than the grains in the substrate region, more powder grains are in

contact with the molten pool boundary. Hence, more epitaxial growth is observed at the boundary of the final molten region and the powder bed surface. The grains formed by epitaxial growth grew upwards along the direction of the local temperature gradient. This grain growth process is defined by the competitive growth mechanism and is described in the "Nucleation and Grain Growth" section in Chapter 4. Longer columnar grains are observed in Fig. 5.24 (a) for the case of 300 mm/s laser scanning speed since the molten pool depth is larger. Fig. 5.24 (b-d) shows that the length of the columnar grains becomes smaller with the increase in scanning speed because of a smaller molten pool depth. For these cases, a few small-sized grains can be observed mainly in the region near the top surface. These small sized grains are almost equally distributed on all sides. Therefore, they are called equiaxed grains. As described earlier in this chapter, equiaxed grains are formed by the bulk nucleation mechanism. This mechanism was modeled with a probabilistic algorithm in the current CA model. Therefore, the locations of sizes of the equiaxed grains did not follow a well-defined structure. However, some observations were made by visually comparing the simulated microstructure images for different laser scanning speeds. At a lower laser scanning speed of 300 mm/s, the equiaxed grains are slightly elongated to the top surface. As the laser scanning speed increases, the equiaxed grains become slightly smaller. Figure 5.24 (d) shows the equiaxed grains formed at a higher scanning speed of 600 mm/s. These small equiaxed grains are elongated along their width.

A significant change in the microstructure was observed when the bulk nucleation effects of final nanoparticle distribution in the Cellular Automata domain were considered. Figures 5.25 (a-d) shows this type of microstructure simulated by the current CA model for varying laser scanning speeds. The positions of the nanoparticles acted as bulk nucleating grains in the CA

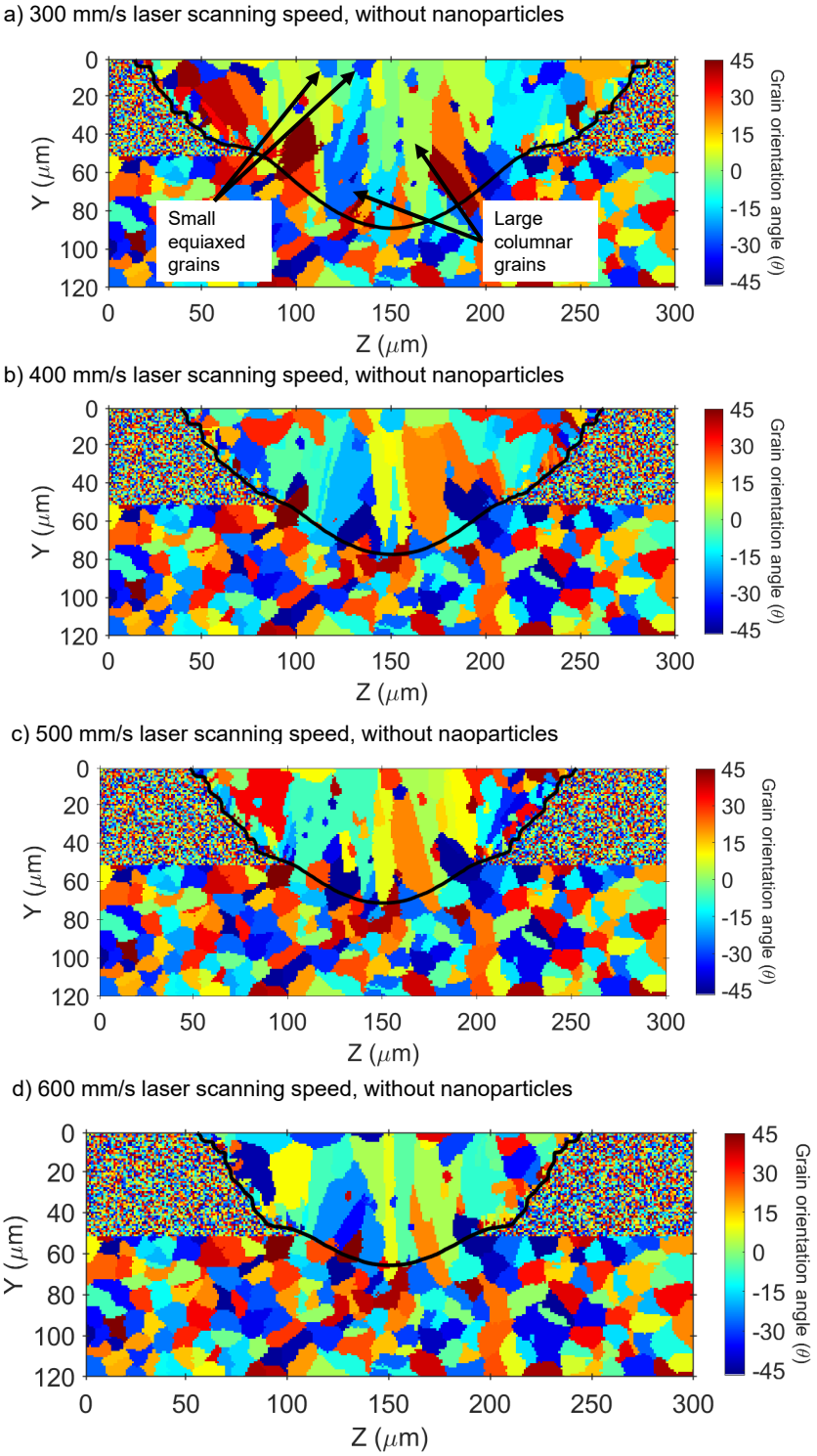


Figure 5.24. Variation of simulated microstructure without considering final nanoparticle distribution with the change in laser scanning speed: (a) laser scanning speed 300 mm/s, (b) laser scanning speed 400 mm/s, (c) laser scanning speed 500 mm/s, (d) laser scanning speed 600 mm/s.

domain. The bulk nucleation mechanism considering the nanoparticles was detailed in chapter 4. From the figures, it can be clearly observed that small equiaxed grains dominated the microstructures. This phenomenon is completely opposite to the microstructure observed in 5.24 (a-d), where columnar grains prevailed. The local distribution of the small equiaxed grains directly corresponds to the nanoparticle distribution computed in the half domain of the CFD model. The final nanoparticle distributions for varying laser speeds, shown in Fig. 5.23, are first mirrored at the symmetry plane and then mapped into the CA domain. The coupling of CFD and CA domain is described in the "Coupling of CFD Model" section in chapter 4. As shown in Figs. 5.23 (a1-a2), nanoparticles were uniformly distributed in region "B" and region "C" for the laser scanning speed of 300 mm/s. As a result, nanoparticles cause bulk nucleation in those regions, forming very small equiaxed grains. They are shown in Figs. 5.25 (a) indicated by region "2" and region "3". Figs. 5.23 (a1-a2) also showed nanoparticle voided regions existed in region "A" and region "D" in its final nanoparticle distribution. Therefore, the grain sizes were locally larger for no bulk nucleation in those regions. They are indicated by region "1" and region "4" in Fig. 5.25 (a). It is shown earlier in Figs. 5.23 (b1-b2, c1-c2, d1-d2) that nanoparticle distribution became more uniform with the increase of laser scanning speeds. Also, it was observed that fewer nanoparticles were located below the powder bed line at higher laser scanning speeds. The melted region below the powder bed line is referred to as the melted substrate region. Therefore, from Figs. 5.25 (b,c,d), the distribution of small equiaxed grains becomes more uniform at the top part of the CA domain at higher scanning speeds. However, the melted region in the substrate has very few equiaxed solid grains. These regions are shown in Figs. 5.25 (b,c,d) marked by regions "5", "6" and "7" respectively. The columnar grains grow from the epitaxial nucleation from the bottom of the final

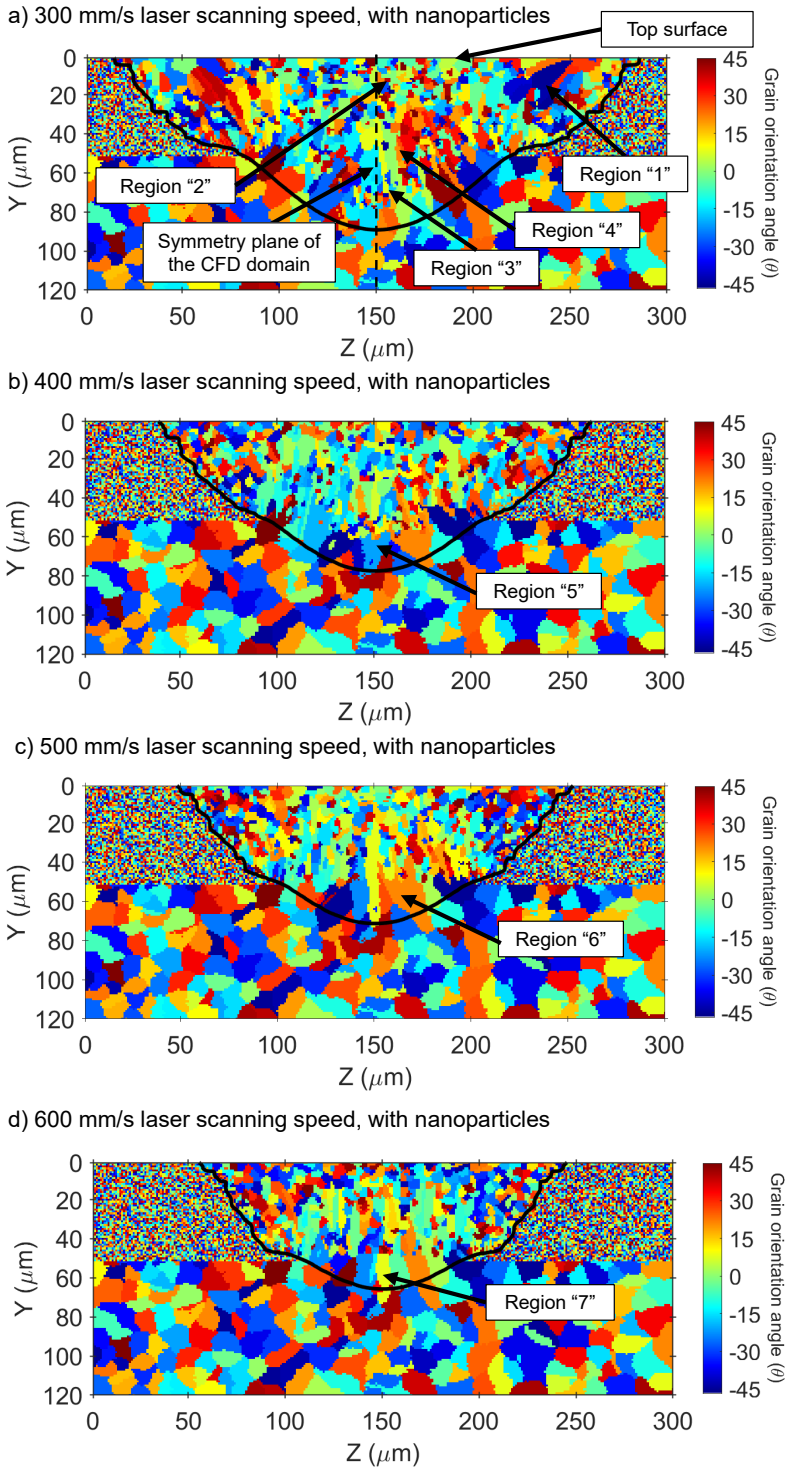


Figure 5.25. Variation of simulated microstructure considering final nanoparticle distribution with the change in laser scanning speed: (a) laser scanning speed 300 mm/s, (b) laser scanning speed 400 mm/s, (c) laser scanning speed 500 mm/s, (d) laser scanning speed 600 mm/s.

molten pool. However, the small equiaxed grains inhibit their growth and reduce the average grain diameter of the microstructure in the 2D transverse plane. The average grain diameter is calculated by the mean lineal intercept method using ASTM-E1382 [84]. A significant decrease in average grain diameter is found when nanoparticles are considered in the microstructures. The average grain diameters of the microstructures, depicted in Figs. 5.24 and 5.25 are listed and compared in Table 5.5.

Table 5.5. Average grain diameter comparison for varying laser scan speed

Laser Scanning Speed (mm/s)	Average grain diameter without considering nanoparticles (μm)	Average grain diameter considering nanoparticles (μm)	Deviation (%)
300	12.95	8	39
400	12.376	7.5	40
500	12.1	7.3	40
600	10.8	7.4	38

As listed above, the average grain diameters, without considering the nanoparticles, are larger for a lower scanning speed. At lower scanning speeds, the dimensions of the melted region are significantly higher. As a result, larger columnar grains can form in this large molten area, increasing its average grain diameter. In addition, for low laser scanning speed, a higher average grain diameter is observed in the simulated microstructures with the bulk nucleation effects of nanoparticles. This is because more particle voided regions are formed at for lower scanning speed, which is filled with larger grains. As laser scanning speed is increased, local nanoparticle distribution becomes more uniform, and those regions are filled with smaller grains. Therefore, the average grain diameter decreases at higher laser scanning speeds when nanoparticles are considered. Interestingly, the percentage decrease in average grain diameter remains almost the

same (38% - 40%) at varying laser scan speeds. The decrease in grain diameter depends on the volume fraction of the nanoparticles and the width and the depth of the molten pool. A higher number of nanoparticles in the transverse plane decrease the average grain diameter by increasing the number of small equiaxed grains. Conversely, higher molten pool dimensions can promote the growth of larger columnar grains from the bottom of the molten pool, increasing the average grain diameter. For the case of varying laser scanning speeds, these two opposite phenomena decrease the average grain diameters almost at the same rate. Therefore, the percentage decrease in grain diameter has a very small difference (38% - 40%) for different laser scanning speeds.

Effect of Laser Power

Temperature and Velocity Distribution

Figure 5.26 shows the histories of the maximum temperature at the top surface and the temperature of representative points P1 and P2 under varying laser power. The laser scanning speed was kept constant at 500 mm/s for these cases. In addition, the entire domain was preheated to 373 K. It can be seen in Figs. 5.26 (a-d) that, as the laser power increases, the maximum temperature at the top surface increases significantly. For example, at a laser power of 125 W, the stable maximum temperature reaches 1729 K rapidly at 200 μs. When the laser power increases to 200 W, the maximum temperature rises to 2585 K. As shown in Figs. 5.26 (a-d), point P1 reaches its maximum temperature value at 870 μs irrespective of the laser power. This is because the laser scanning speed was the same for these cases. However, after reaching the maximum temperature, the point P1 cools down below the liquidus temperature at different times. At a higher laser power, it takes more time to cool down and solidify the region, indicating the cooling rate is lower for higher laser powers.

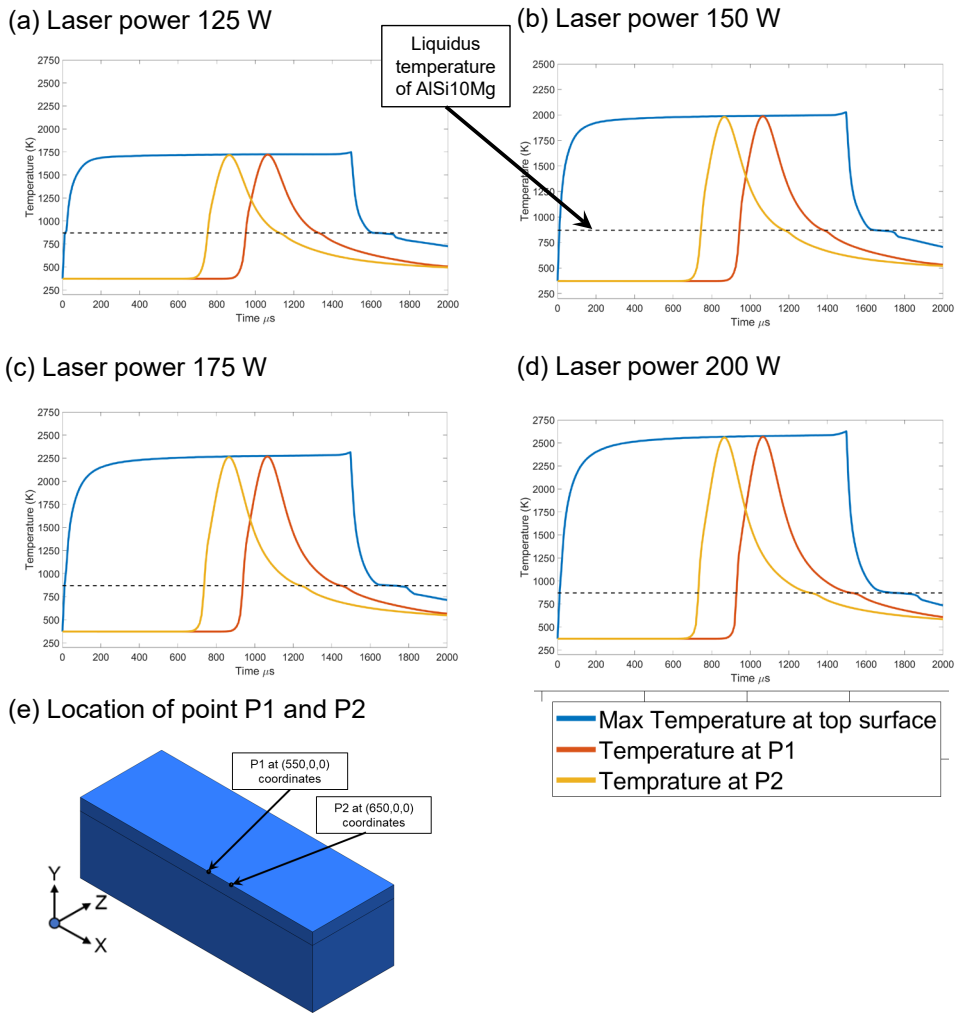


Figure 5.26. Variation of temperature histories of the maximum temperature and representative P1 and P2 points on the top surface: (a) laser power of 125 W, (b) laser power of 150 W, (c) laser power of 175 W, (d) laser power of 200 W and (e) representative points P1 and P2.

Figure 5.27 shows the temperature and velocity distribution for different laser powers when the laser source moves at x = 650 μm on the top surface. The laser is moving at a fixed speed of 500 mm/s with a preheating temperature of 373 K for these cases. The high temperature region increases in volume with the increase of laser power as more heat are absorbed by the top surface.

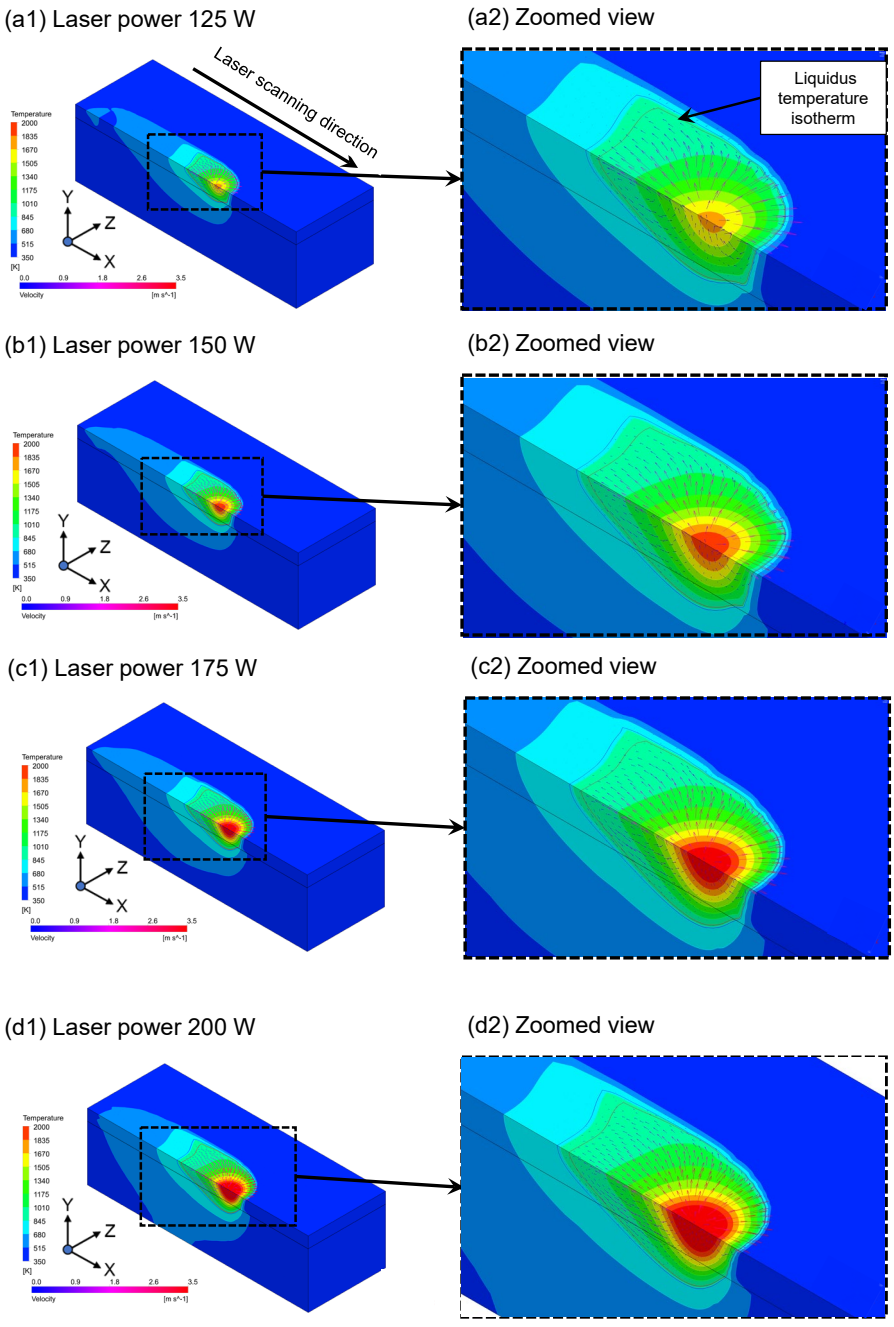


Figure 5.27. Temperature and velocity distribution due to variation of laser power: (a) laser power of 125 W, (b) laser power of 150 W, (c) laser power of 175 W, and (d) laser power of 200 W.

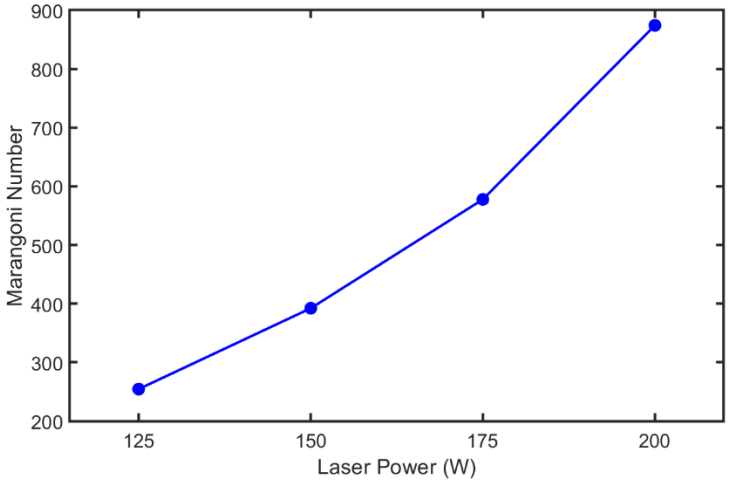


Figure 5.28. Variation of Marangoni number with the change of laser power

The molten pool velocity increases with the increase of Marangoni convection at the top surface. The relative strength of Marangoni convection at different laser power can be compared by calculating the Marangoni number using Eq. 2.19. The change in Marangoni number for different laser powers is shown in Fig. 5.28. At a higher laser power of 200 W, the calculated Marangoni number is 875, while it decreases to 255 at lower power of 125W. Due to a high Marangoni number at higher laser power, a strong radially outward flow is observed at the top surface. As discussed earlier in this chapter, this strong radially outward flow generates strong recirculation zones parallel to the symmetric and the transverse planes.

As shown in Fig. 5.29, the molten pool dimensions are significantly increased with the increase of laser power. It can be observed that the depth, width, and length of the molten pool increase linearly with the increase of laser power. Since the powder bed can absorb more heat at higher laser power, the dimensions of the molten region increase. High Marangoni convection increases the width of the molten pool by convecting from the center to the molten pool boundary

by its radially outward flow. With these two combined effects, the molten pool dimensions are significantly increased with the increase of laser power. Fig. 5.29 shows the change in width, depth, and the length of the molten pool with the change in laser power from 125W to 200 W. It can be observed that the dimensions of the molten pool increase linearly with the increase of laser power.

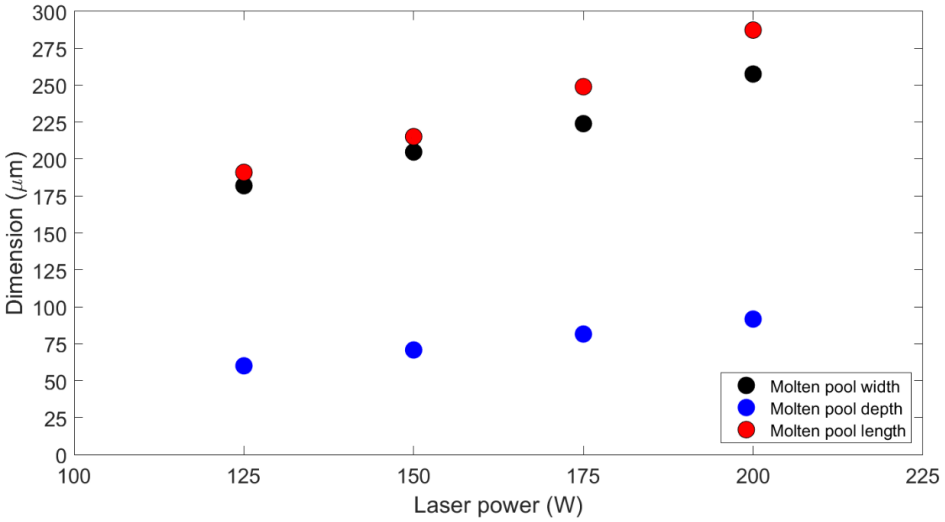


Figure 5.29. Variation of molten pool dimensions with the change in laser power.

Nanoparticle Distribution at a transverse plane

Figure 5.30 shows the final nanoparticle distribution at a 2D transverse plane of 650 µm with the change in laser power. The laser scanning speed was fixed at 500 mm/s, and the entire domain was preheated to 100°C for these cases. Figures 5.30 (a1-a2) and (b1-b2) show the nanoparticle distribution for 125 W and 150 W, respectively. A uniform distribution of nanoparticles is observed in the 2D plane, with some local voided regions for these cases. These local void regions are indicated by region "K" and region "L" in Figs. (a1) and (b1), respectively. The nanoparticle distribution for 175 W laser power is shown in Figs. 5.30 (c1-c2). A larger particle voided region is observed in the region "M" in the transverse plane in these figures.

Similarly, a larger particle voided region is present in the central region for 200 W laser power and is indicated by region “N” in Figs. 5.30 (d1-d2).

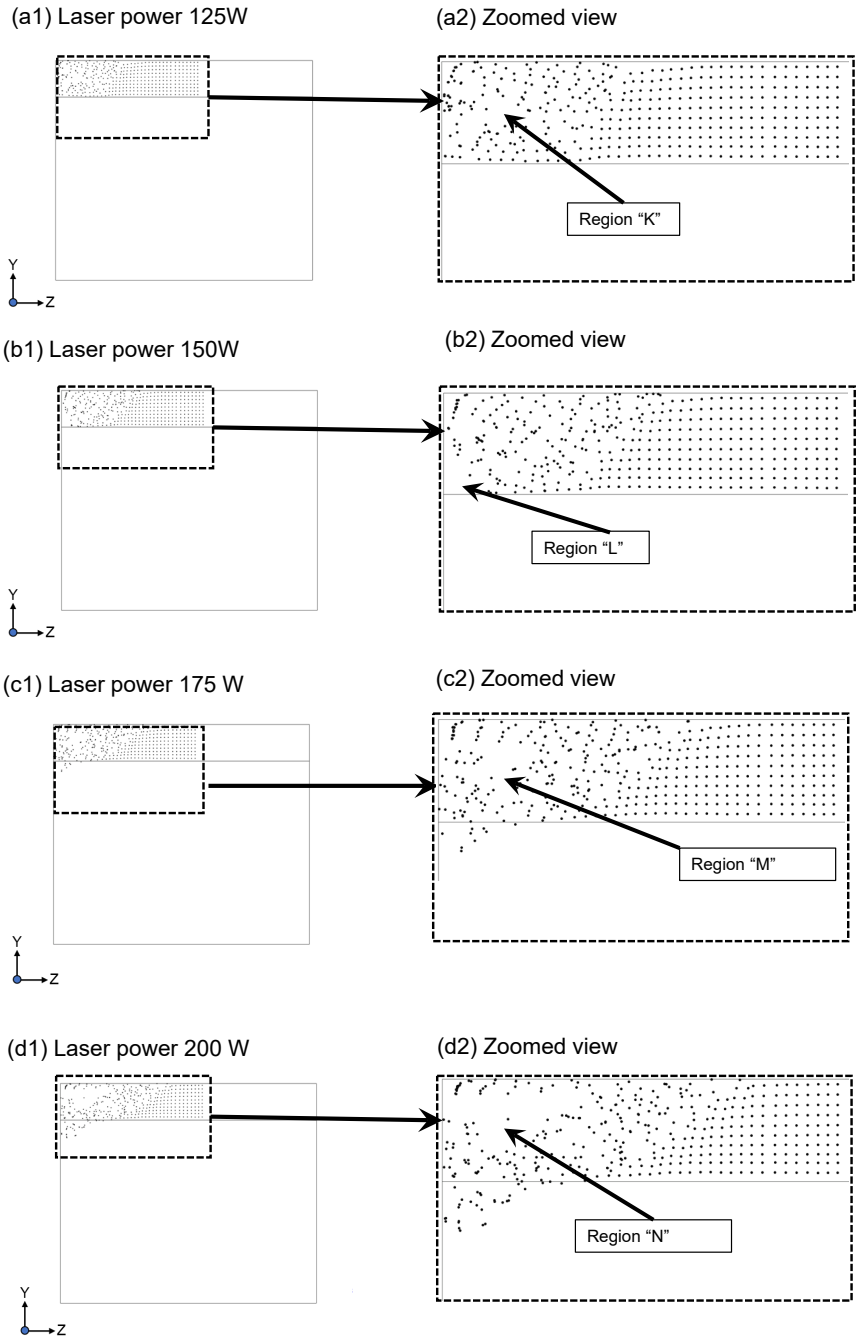


Figure 5.30. Final nanoparticle distribution in solidified region due to variation of laser power: (a1-a2) laser power of 125W, (b1-b2) laser power of 150W, (c1-c2) laser power of 175 W, (d1-d2) laser power of 200W.

As discussed earlier, nanoparticle distribution in the solid region is primarily dictated by the combined effect of two perpendicular recirculation zone. The strength of these recirculation zones is dependent on the strength of the Marangoni convection. Higher Marangoni convection creates a strong recirculation zone parallel to the transverse plane, generating a strong centrifugal force on the nanoparticles. This pushes the nanoparticles out of the center of the recirculation zone. Another recirculation zone acting perpendicular to the symmetry plane pushes the nanoparticles downward from the top plane. This phenomenon was earlier illustrated in 5.13 (c7-c8). Due to strong Marangoni convection, the particle voided regions are observed at regions “M” and “N”, respectively, for laser power of 175 W and 200 W. The particle void region is relatively greater in region “N” because of the higher Marangoni convection for the laser power of 200 W. During solidification, the downward velocity flow from the top was higher at higher laser powers. Therefore, the particles are pushed in the molten substrate region. However, at lower laser powers, i.e., 125 W and 150 W, the downward velocity vectors from the top part of the transverse plane are small. As a result, a higher solidification rate solidifies the regions before nanoparticles can fill up the void space in regions “L” and “M”. Therefore, some local nanoparticle voided region is observed in the final nanoparticle distribution for a lower laser power of 125 W and 150 W.

Microstructure Evolution

Figures 5.31 (a-d) show the microstructures simulated by the present Cellular Automata model for varying laser power without considering the bulk nucleation effects of the nanoparticles. As shown earlier, columnar grains are prevalent in the microstructures when the bulk nucleation effects of the nanoparticles are not considered. The same trend is present in the simulated

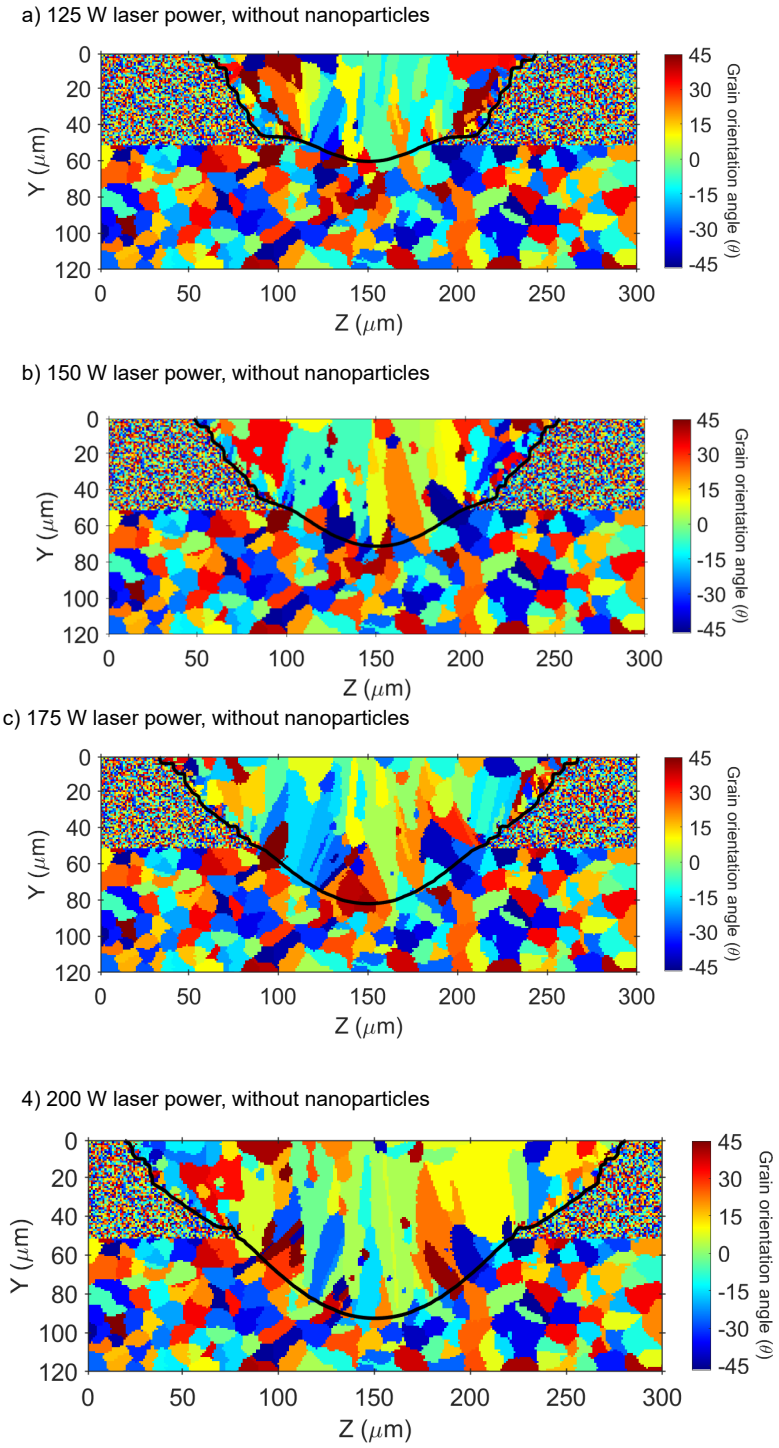


Figure 5.31. Variation of simulated microstructures without considering final nanoparticle distribution with change in laser power: (a) laser power of 125W, (b) laser power of 150W, (c) laser power of 175 W, (d) laser power of 200W.

microstructures at different laser powers. As shown in Fig. 5.31, smaller columnar grains can be observed for a laser power of 125 W since the depth and width of the melted region are small. As the laser power increases, the molten pool dimensions increase and large columnar grains are observed in the resolidified region. In addition, a few small equiaxed regions are observed that are dispersed in the interior of the resolidified microstructure. As shown before in Fig 5.17, these equiaxed grains are mainly present near the top surface. The same observation can be made for the simulated microstructures for different laser powers in Fig. 5.31. The bulk nucleation becomes prominent during solidification when nanoparticle distribution is considered. A large amount of bulk nucleation promoted the growth of fine equiaxed grains, which was shown earlier in Fig. 5.17. Figure 5.32 (a-d) shows the simulated microstructures when the bulk nucleation effects of the nanoparticles are considered. The final distribution of the nanoparticles calculated by the CFD model was incorporated into the current CA domain. The workflow of coupling the CFD results into CA domain is detailed in Chapter 4. The final nanoparticle distribution for each of these cases were shown in Fig. 5.30. In contrast to Fig. 5.31, small equiaxed grains dominated the microstructure, inhibiting the growth of columnar grains. As shown in Fig. 5.32, the local distribution of the nanoparticles promotes small equiaxed regions in the microstructure. However, slightly larger equiaxed grains are observed at the local nanoparticle voided region. For a higher laser power, a large particle voided region was seen in the interior of the solidified regions. For example, a particle voided region “M” was seen in Fig. 5.30 (c2) for 175 W laser power, and for 200 W laser power a particle voided region “N” was seen in Fig. 5.30 (d2) for 200 W laser power. Therefore, those regions have slightly larger grains which are shown in Fig. 5.32 (c) and (d) for 175 W and 200 W laser power, respectively. These regions are indicated by region “8” and region

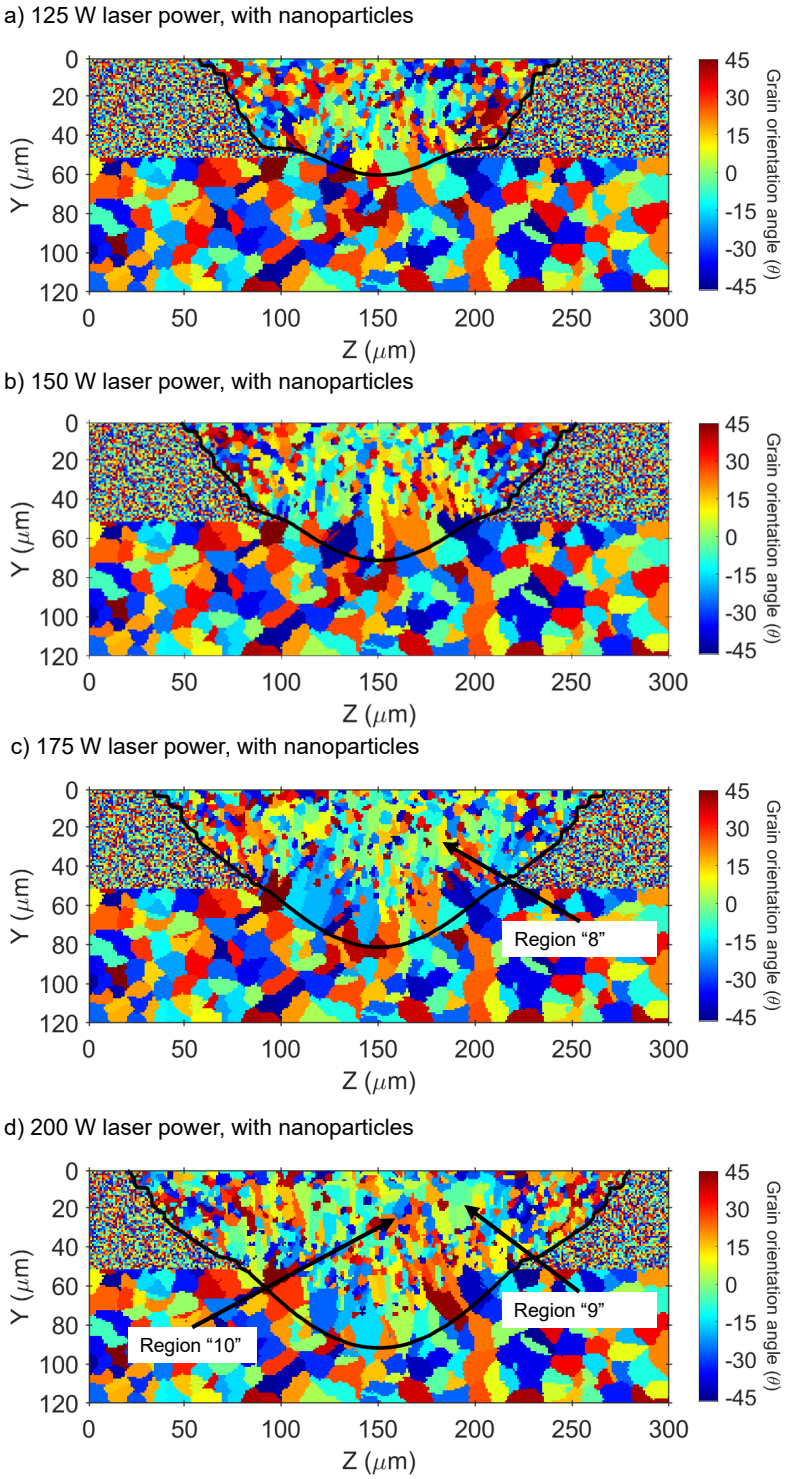


Figure 5.32. Variation of simulated microstructures considering final nanoparticle distribution with change in laser power: (a) laser power of 125W, (b) laser power of 150W, (c) laser power of 175 W, (d) laser power of 200W.

"9" in those figures. Smaller equiaxed grains are observed where particles are more uniformly distributed for higher laser powers. A representative of small equiaxed grain regions is shown in region "10" in Fig. 5.32 (d). As the laser power decreased, the nanoparticle voided region diminished, and small equiaxed grains formed around the positions of the nanoparticles. The effects of bulk nucleation of grains on the average grain diameter can be measured using the mean lineal intercept method [84]. The average grain sizes of the simulated microstructures for varying laser powers are listed in Table 5.6. The average grain diameter was significantly lower when bulk nucleating effects of the nanoparticles were considered. The average grain diameter in the simulated microstructure for higher laser power was significantly reduced by 43% when nanoparticles were considered. The reduction in average grain diameter was lesser for lower laser power.

Table 5.6. Average grain diameter comparison for varying laser power

Laser power (W)	Average grain diameter without considering nanoparticles (μm)	Average grain diameter considering nanoparticles (μm)	Deviation in average diameter (%)
125	9.52	6.6	31
150	12.1	7.2	40
175	12.4	7.4	40
200	13.2	7.8	41

Effect of Preheating Temperature.

Temperature and Velocity Distribution

In the current study, three different preheating temperatures: 300 K, 373 K, and 473 K, were used. As 300 K is the ambient temperature, preheating to this temperature can be referred to as no preheating. For this study, the laser power and scanning speed were fixed to 150 W and 500

mm/s, respectively. Figure 5.33 illustrates the histories of the maximum temperature on the top surface and the temperature of the representative points P1 and P2 for different preheating temperatures. A slight increase is observed in the maximum temperature with the increase in preheating temperature. As shown in the figure, the maximum temperature was 1939 K when

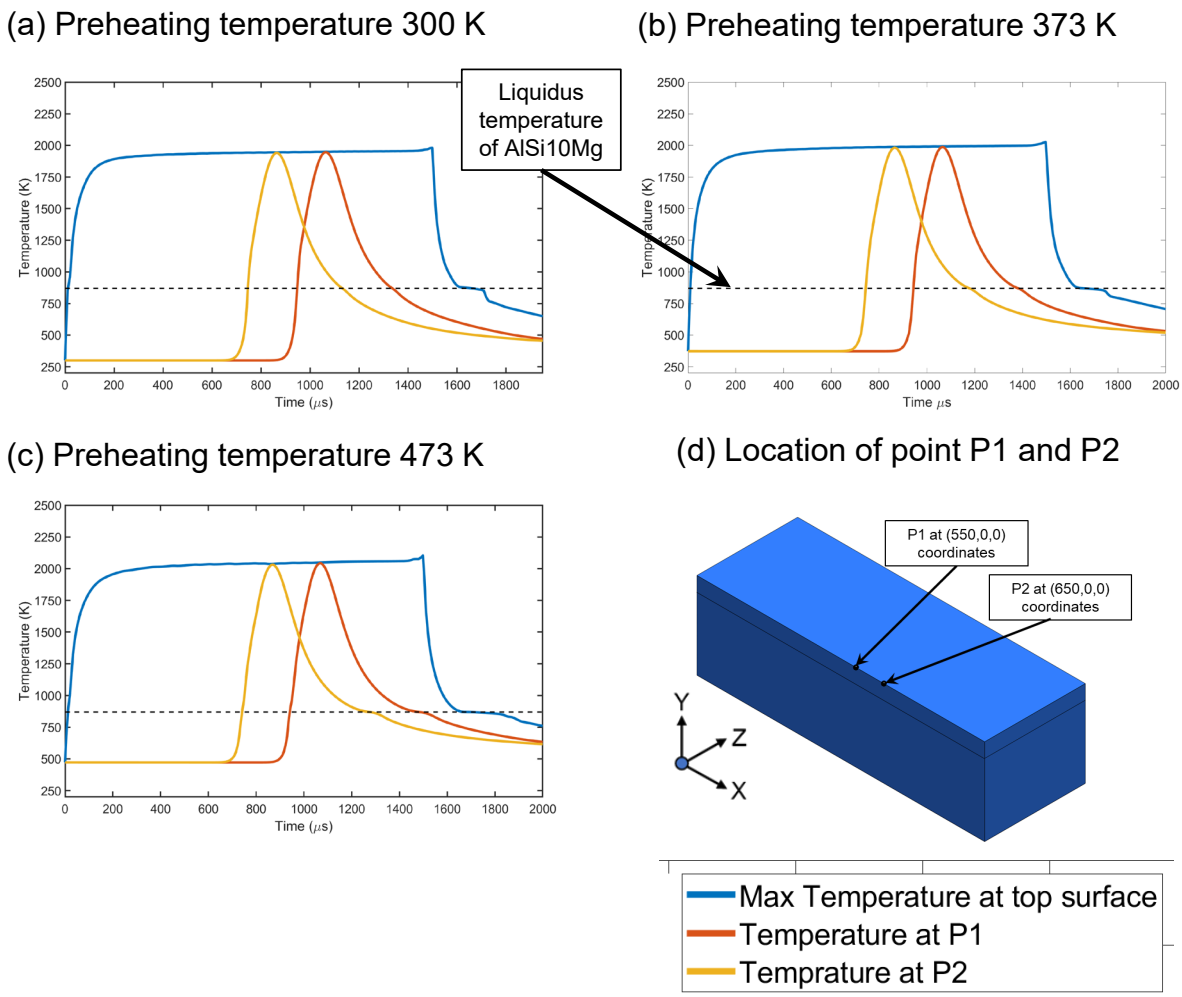


Figure 5.33. Variation of temperature histories of the maximum temperature and representative P1 and P2 points on the top surface: (a) preheating temperature of 300 K, (b) preheating temperature of 373 K, (c) preheating temperature of 473 K, (d) representative points P1 and P2.

preheating temperature was set to 300 K. However, the maximum temperature increased slightly to 2044 K at a preheating temperature of 473 K. As shown in Fig. 5.33, P1 reached its maximum temperature at 875 μs irrespective of the preheating temperature. This is because a fixed laser scanning speed was applied for these different preheating temperatures. However, after reaching the maximum temperature, the temperature of P1 drops below the liquidus temperature at different times. The time to drop below the liquidus temperature of the metal increased at higher preheating temperatures. A similar phenomenon occurred for point P2. This indicates that, with increasing preheating temperature, the cooling rate of the top surface decreases.

Figure 5.34 shows the temperature and velocity distribution at different preheating temperatures. As the maximum temperature does not vary significantly, a similar temperature and velocity profile can be observed inside the liquid molten pool. However, temperature distribution at the trailing edge of the molten pool is different for these preheating temperatures. With the increase of the preheating temperature, the temperature profile is more elongated behind the high temperature region. Hence, a longer molten pool formed at a higher preheating temperature.

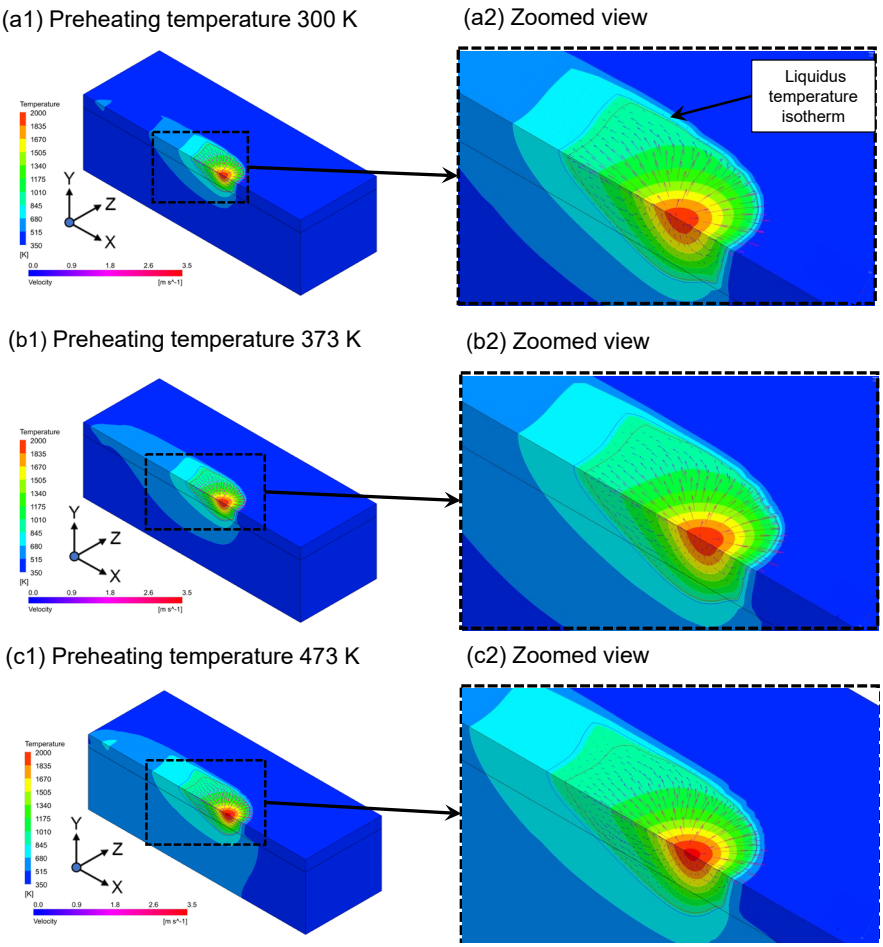


Figure 5.34. Temperature and velocity distribution at time 1050 µs due to variation of preheating temperature: (a1-a2) preheating temperature of 300 K, (b1-b2) preheating temperature of 373 K, (c1-c2) preheating temperature of 473 K.

The width and the depth of the molten pool also increased with increasing preheating temperature. The molten pool dimensions for varying preheating temperatures are shown in Fig. 5.35. At higher preheating temperatures, the metal requires less energy to increase its temperature beyond the liquidus temperature. Therefore, molten pool dimensions increased at higher preheating temperatures.

.

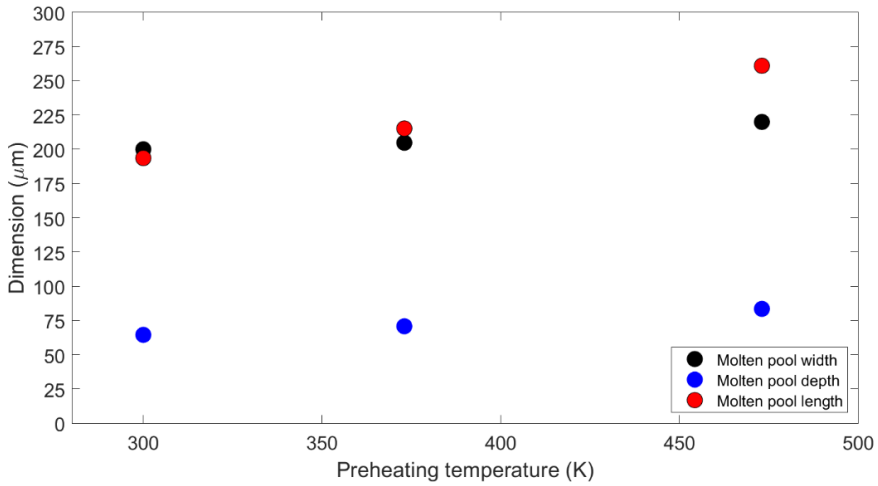


Figure 5.35. Variation of molten pool dimensions due to change in preheating temperature.

Figure 5.36 shows the Marangoni number associated with different preheating temperatures. Marangoni number increased from 365 to 452 when preheating temperature increased from 300 K to 473 K. This suggested that the effect of Marangoni convection varied slightly with the change in preheating temperature.

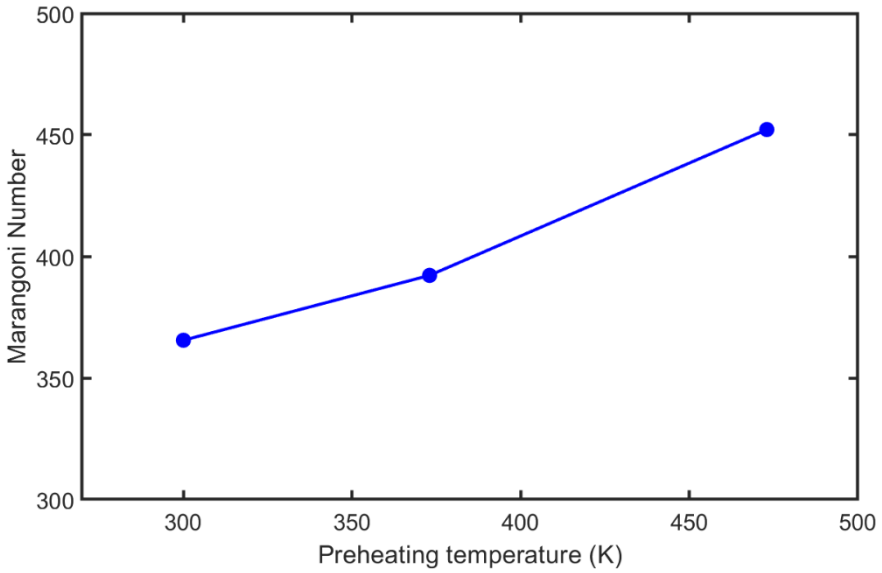


Figure 5.36. Variation in Marangoni number due to change in preheating temperature.

Nanoparticle Distribution on the transverse plane

The difference in nanoparticle distribution in a 2D transverse plane at x = 650 μm due to increasing preheated temperature is shown in Fig. 5.37. Laser power was set to 150 W, and its scanning speed was fixed to 500 mm/s for these cases. A uniform final nanoparticle distribution can be observed in Figs. 5.37 (a1-a2) across the transverse plane when the entire domain is preheated to 300 K. However, a small particle voided region can be seen at region "O" near the symmetric plane. In Figs. 5.37 (b1-b2), a slightly larger particle voided region can be seen at region "P" in the final nanoparticle distribution. The downward flow from the top part of the transverse plane drives nanoparticles downwards from the top inside the molten pool to fill up the voided region. However, the higher speed of the upward moving solidification front restricts the movement of the particles before they can reach the voided space. As a result, particle voided regions are observed at regions "O" and "P" at lower preheating temperatures. Final nanoparticle distribution changes again when the preheating temperature is increased to 473 K and is shown in Figs. 5.37 (c1-c2). A particle voided region is shown in region "Q" in the transverse plane. This particle voided region is created by a relatively strong recirculation zone parallel to the transverse plane. The recirculation zone pushes the nanoparticles from its center by centrifugal force and hence forms this particle-void space.

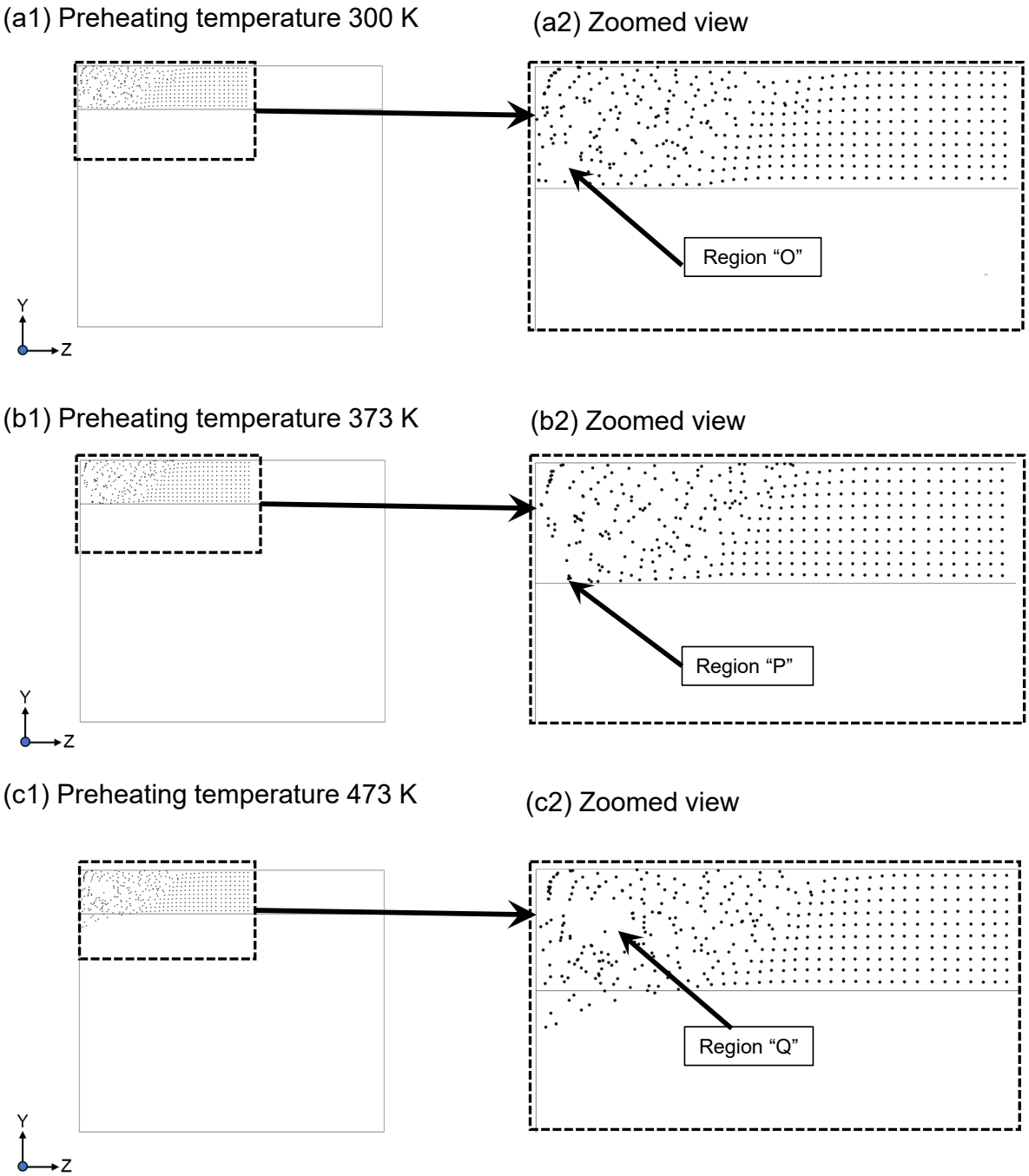


Figure 5.37. Final nanoparticle distribution in the solidified region due to variation of preheating temperature: (a1-a2) 300 K preheating temperature, (b1-b2) 373 K preheating temperature, and (c1-c2) 473 K preheating temperature.

Microstructure evolution

Simulated microstructure in the 2D transverse plane at x = 650 μm for varying preheated temperatures without considering the nanoparticles are shown in Fig. 5.38. Mixed columnar and equiaxed grains can be shown in their microstructures. Columnar grains are predominant in the microstructures, and the length of the columnar grains increases with the increase of preheated temperature. As the density of bulk nucleation is very small, a few equiaxed grains are observed near the top surface. The bulk nucleation density increases when nanoparticles are considered while simulating the microstructures using the current CA model. Figures 5.39 (a-c) show the microstructures considering the bulk nucleation effects of the nanoparticles for varying preheating temperatures. As shown in the earlier parametric studies, when bulk nucleation effects of the nanoparticles are considered, very small equiaxed grains grow if the local nanoparticle distribution is uniform. In addition, grains are slightly larger in the local nanoparticle voided regions. The same pattern is observed in the microstructures in Fig. 5.39. Due to local uniform nanoparticle distribution at lower preheating temperatures, very small equiaxed grains are observed in the upper region of the simulated microstructures. At a higher preheating temperature of 473 K, some large grains are observed in the particle voided region, and they are observed in the region “11” in Fig.

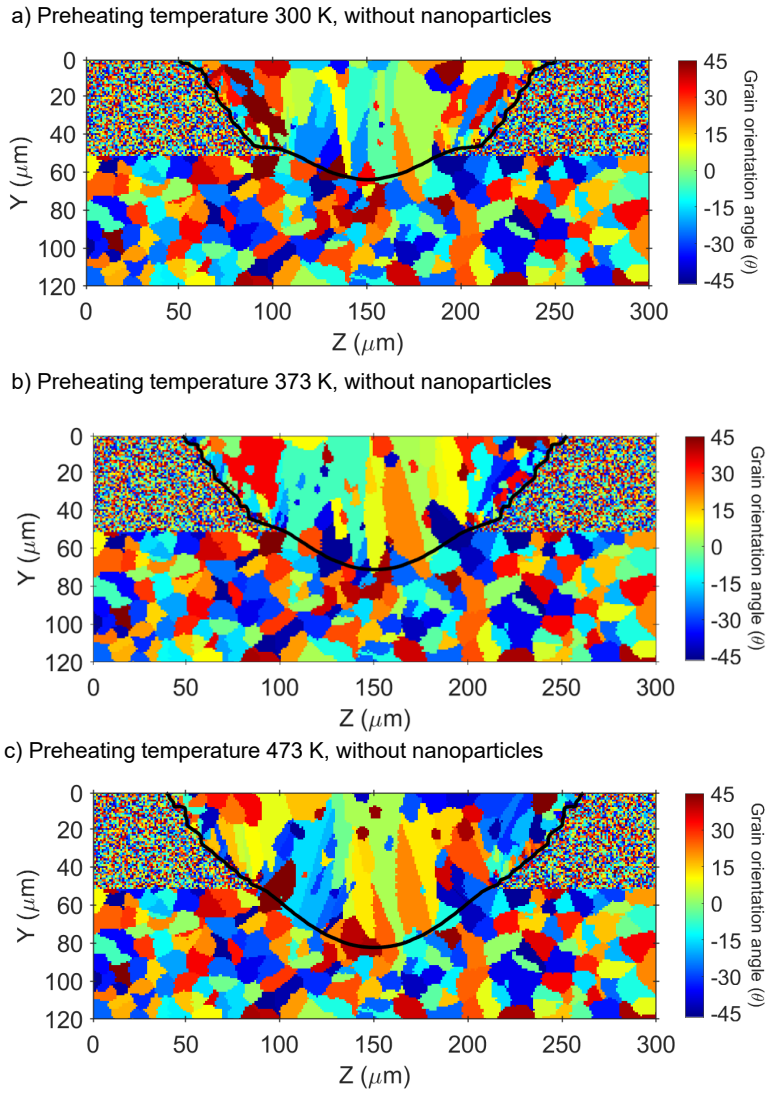


Figure 5.38. Variation of simulated microstructure without considering nanoparticles due to change in preheating temperature: (a) 300 K preheating temperature, (b) 373 K preheating temperature and (c) 473 K preheating temperature.

5.39 (c). The average grain diameters for lower preheating temperatures are slightly smaller than higher preheating temperatures. The average grain diameters of the simulated microstructures for varying preheated are listed in Table 5.7. The average grain diameter was significantly lower when

bulk nucleating effects of the nanoparticles were considered. The average grain diameter is reduced by 33- 40 % when the nanoparticles enhance bulk nucleation during solidification.

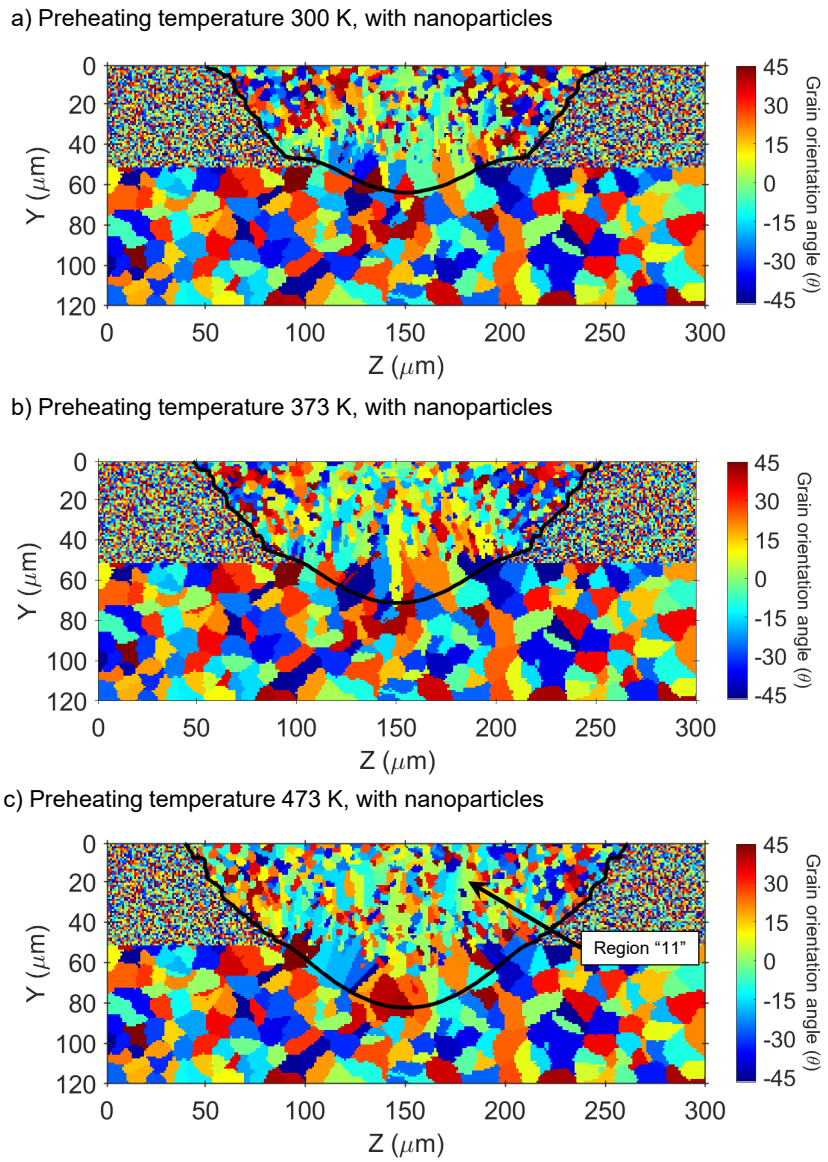


Figure 5.39. Variation of simulated microstructure considering nanoparticles with the change in preheating temperature: (a) 300 K preheating temperature, (b) 373 K preheating temperature and (c) 473 K preheating temperature.

Table 5.7. Average grain diameter comparison for varying preheating temperatures.

Preheating temperature (K)	Average grain diameter without considering nanoparticles (μm)	Average grain diameter considering nanoparticles (μm)	Deviation in average diameter (%)
300	10.3	6.9	33
373	12.1	7.3	40
473	12.5	7.7	39

CHAPTER SIX

CONCLUSIONS AND RECOMMENDATIONS

In the current study, a 3D computational fluid dynamics (CFD) model was coupled with a 2D Cellular Automata (CA) model to analyze the formation of metal nanocomposites during the selective laser melting (SLM) process. A novel modeling approach was used to numerically investigate the transport of reinforced nanoparticles in the molten pool of liquid aluminum in a 2D transverse plane from the 3D CFD model. In addition, the effects of the nanoparticle distribution on microstructure formation during solidification were investigated in the current CA model with a new coupling method with the CFD model. The CFD model calculated heat and fluid flow characteristics and nanoparticle transport, while the CA model simulated the microstructure evolution during the SLM process. In addition, the CFD model incorporated the following thermo-physical processes that are inherent in an SLM process: i) moving laser heat source, ii) phase change from powder state to metal state, iii) melting and solidification of metallic materials, iv) Marangoni and buoyancy convection and v) nanoparticle tracking.

In the current study, the numerical results from the CFD and CA model were validated against experimentally published data for the molten pool dimensions and the average grain diameter. After determining the validity of the model, a detailed parametric analysis was performed to study the effects of various parameters: i) laser power, ii) laser scanning speed, and iii) preheating temperature. The following conclusions can be drawn based on the present numerical study:

1. A moving laser heat source created a very high temperature around the laser spot center which melted the powder and underlying substrate. However, the effective

thermal conductivity of the powder bed was very low than the thermal conductivity of the solid and liquid metal. As a result, accumulated heat diffused more evenly in the solid region compared to the unmelted powder region. This resulted in an uneven temperature gradient field inside the molten pool and along its boundary.

2. The liquid metal in the molten pool was driven by the Marangoni convection resulting from the temperature gradient at the top surface. A clockwise and an anti-clockwise recirculating flow pattern was observed parallel to the symmetric plane. Another recirculation zone parallel to the transverse planes accompanied these recirculation zones. The combined effect of these recirculation zones strongly influenced the molten pool fluid flow. The nanoparticles reinforced in the liquid aluminum alloy were primarily transported along the velocity vectors of these recirculation zones.
3. Large columnar grains with a few equiaxed grains near the top surface were observed in the simulated microstructures when nanoparticles were not considered. These equiaxed grains were formed by bulk nucleation when an undercooled liquid region was present ahead of the solidification front. Nanoparticles increased bulk nucleation density in the undercooled liquid to promote the growth of equiaxed grains during solidification. As a result, small, randomly oriented equiaxed grains were more prominent in the simulated microstructure when nanoparticles were considered in the CA model. The average grain diameter was reduced by 30-40% when bulk nucleation effects of the nanoparticles were considered. Reducing

average grain size can improve tensile strength and isotropic mechanical behavior in the product fabricated by selective laser melting.

4. The energy absorbed by the powder bed increased when laser scanning speed was decreased. Therefore, the maximum temperature obtained at the top surface increased with the decrease in laser scanning speeds. Similarly, the molten pool volume increased at lower scanning speeds. In addition, the Marangoni number increased at lower scanning speeds, indicating higher Marangoni convection. This resulted in a strong recirculation zone along the transverse plane. The recirculation zone pushed nanoparticles from its center by centrifugal force and created a local particle void region. This particle voided region near the top surface was more prominent at lower laser scanning speeds. The nanoparticles were more uniformly distributed along the transverse plane at a higher scanning speed compared to the lower scanning speeds. A downward flow was observed in the transverse plane in the final solidification stages, which pushed the nanoparticles from the top to the lower parts of the molten pool. However, an upward moving solidification front from the bottom of the molten pool restricted the fluid flow. This dynamic interaction of the solidification front and molten pool flow created some local nanoparticle dense and void regions. Small randomly oriented equiaxed grains were observed in the simulated microstructure, where particles were uniformly distributed. In contrast, the grain sizes were slightly larger in local particle voided regions.

5. The effects of laser power were substantial on the maximum temperature of the powder bed surface. The increase in laser power at a fixed laser scanning speed and preheating temperature increased maximum temperature and the resulting molten pool volume significantly. The rise in the Marangoni number caused an intense Marangoni convection on the top surface of the molten pool. This resulted in a strong recirculation zone tangential to the transverse plane, driving nanoparticles from its center. Therefore, a particle voided region formed in the transverse plane at higher laser power. The nanoparticles were also pushed further to the bottom at higher laser power by strong downward flow along the molten pool boundary. Nevertheless, the final nanoparticle became uniform at lower laser power, where the effects of Marangoni convection were low. As expected, the microstructure simulated by the present CA model showed a direct relationship between the local grain sizes and the nanoparticle distribution. Local grain sizes were very small, where nanoparticles were uniformly distributed. Conversely, local grain sizes were slightly larger at higher laser power.
6. Increase in preheating temperature showed a significant increase in the molten pool dimensions at a fixed laser power and scanning speed. The powder bed and the solid region required less energy to form a molten pool at a higher preheated temperature. Compared to other parameters, the increase in maximum temperature was less with increased preheating temperatures. The Marangoni convection was low even at higher molten pool dimensions. This phenomenon was contrary to the previous observations, where Marangoni convection was found high at higher

molten pool dimensions. This resulted in a fewer particle voided region at higher molten pool dimensions, imparting more uniform nanoparticle distribution in a transverse plane.

Recommendations for future works on modeling the SLM process are as follows:

1. The deformation of the free surface of the molten pool could be explored in further studies regarding numerical modeling of the SLM process. Proper modeling of free surface deformation could explain the formation of non-uniform surfaces on the top of the solidified layer. In addition, how nanoparticles would interact with the deforming surface could be an important topic of research.
2. The particle transport could be incorporated with a powder scale modeling approach. This could provide useful insights regarding nanoparticle deposition in the powder bed and the final solidified region.
3. The effect of the volume fraction of the reinforced nanoparticles on particle transport in the metal matrix should be explored. The interaction between the nanoparticles could be incorporated to analyze the agglomeration of nanoparticles. The agglomeration of nanoparticles is the most common cause of defects in metal matrix nanocomposites. Hence its formation and mitigation should be concentrated in future studies.
4. A 3D microstructure model should be incorporated with a CFD model to analyze the microstructure evolution during this process. The interaction of nanoparticles in the undercooled liquid metal should be explored by proper material kinetics and incorporated into the microstructure model.

5. As shown in Table 5.5, the average grain diameter decreases at the same rate when bulk nucleating effects of the nanoparticles are considered while varying the laser scanning speeds. However, the percentage decreases in average grain diameters are different for varying laser powers and the preheating temperatures and are shown in Tables 5.6 and 5.7. A detailed study can be conducted to investigate the effects of the process parameters in decreasing the average diameter when nanoparticles are considered. This study can provide useful insights into finding the optimum SLM process parameters where the decrease in average grain diameters is more impactful.
6. The Cellular Automata (CA) microstructure model can simulate different microstructures for the same set of SLM process parameters. Therefore, for a single set of SLM process parameters, several microstructure simulations should be conducted. The average grain diameters measured from those predicted microstructures can be used to provide a mean value and the standard deviations of the average grain size. A lower standard deviation means the average grain diameter is uniform. Conversely, a wider standard deviation indicates that the average grain diameter is non-uniformly distributed in the predicted microstructure. Thus, this statistical analysis can be useful in understanding the uniformity of average grain diameter at different laser process parameters.
7. The SLM process fabricates products involving multiple side-by-side laser scanning tracks and multiple build layers on top of the solidified regions. The effects of multiple scan tracks and multiple build layers on nanoparticle distribution

and microstructure formation could be the subject of further research. Thus, the formation of a full-scale product can be assessed considering the effects of multiple laser scans and multiple layers.

REFERENCES CITED

[1] Emelogu, A., Marufuzzaman, M., Thompson, S. M., Shamsaei, N., and Bian, L., 2016, "Additive Manufacturing of Biomedical Implants: A Feasibility Assessment via Supply-Chain Cost Analysis," Additive Manufacturing, **11**, pp. 97–113.

[2] Thompson, M. K., Moroni, G., Vaneker, T., Fadel, G., Campbell, R. I., Gibson, I., Bernard, A., Schulz, J., Graf, P., Ahuja, B., and Martina, F., 2016, "Design for Additive Manufacturing: Trends, Opportunities, Considerations, and Constraints," CIRP Annals, **65**(2), pp. 737–760.

[3] Jensen, D., Taufiq Elahi, A. N. M., Ghashami, M., and Park, K., 2021, "Submicrometer-Gap Thermionic Power Generation Based on Comprehensive Modeling of Charge and Thermal Transport," Physical Review Applied, **15**(2), p. 024062.

[4] Aversa, A., Moshiri, M., Librera, E., Hadi, M., Marchese, G., Manfredi, D., Lorusso, M., Calignano, F., Biamino, S., Lombardi, M., and Pavese, M., 2018, "Single Scan Track Analyses on Aluminium Based Powders," Journal of Materials Processing Technology, **255**, pp. 17–25.

[5] AlMangour, B., Grzesiak, D., Cheng, J., and Ertas, Y., 2018, "Thermal Behavior of the Molten Pool, Microstructural Evolution, and Tribological Performance during Selective Laser Melting of TiC/316L Stainless Steel Nanocomposites: Experimental and Simulation Methods," Journal of Materials Processing Technology, **257**, pp. 288–301.

[6] Yuan, P., and Gu, D., 2015, "Molten Pool Behaviour and Its Physical Mechanism during Selective Laser Melting of TiC/AlSi10Mg Nanocomposites: Simulation and Experiments," Journal of Physics D: Applied Physics, **48**(3), p. 035303.

[7] Xiao, Y. K., Bian, Z. Y., Wu, Y., Ji, G., Li, Y. Q., Li, M. J., Lian, Q., Chen, Z., Addad, A., and Wang, H. W., 2019, "Effect of Nano-TiB2 Particles on the Anisotropy in an AlSi10Mg Alloy Processed by Selective Laser Melting," Journal of Alloys and Compounds, **798**, pp. 644–655.

[8] Gu, D., and Yuan, P., 2015, "Thermal Evolution Behavior and Fluid Dynamics during Laser Additive Manufacturing of Al-Based Nanocomposites: Underlying Role of Reinforcement Weight Fraction," Journal of Applied Physics, **118**(23), p. 233109.

[9] Gandin, Ch.-A., and Rappaz, M., 1994, "A Coupled Finite Element-Cellular Automaton Model for the Prediction of Dendritic Grain Structures in Solidification Processes," Acta Metallurgica et Materialia, **42**(7), pp. 2233–2246.

[10] Gandin, Ch.-A., and Rappaz, M., 1997, "A 3D Cellular Automaton Algorithm for the Prediction of Dendritic Grain Growth," Acta Materialia, **45**(5), pp. 2187–2195.

[11] Zhang, Y., and Zhang, J., 2019, "Modeling of Solidification Microstructure Evolution in Laser Powder Bed Fusion Fabricated 316L Stainless Steel Using Combined Computational Fluid Dynamics and Cellular Automata," Additive Manufacturing, **28**, pp. 750–765.

[12] Ao, X., Xia, H., Liu, J., and He, Q., 2020, "Simulations of Microstructure Coupling with Moving Molten Pool by Selective Laser Melting Using a Cellular Automaton," Materials & Design, **185**, p. 108230.

[13] Gerstgrasser, M., Jakob, R., Pandya, K. S., Stirnimann, J., and Wegener, K., 2021, "CA Single Track Microstructure Simulation of Nickel Base Alloy CM247LC and Stainless Steel S316L, Including Experimental Validation of S316L," Materials & Design, **199**, p. 109395.

[14] Ansari Dezfoli, A. R., Lo, Y.-L., and Raza, M. M., 2021, "Prediction of Epitaxial Grain Growth in Single-Track Laser Melting of IN718 Using Integrated Finite Element and Cellular Automaton Approach," Materials, **14**(18), p. 5202.

[15] Akram, J., Chalavadi, P., Pal, D., and Stucker, B., 2018, "Understanding Grain Evolution in Additive Manufacturing through Modeling," Additive Manufacturing, **21**, pp. 255–268.

[16] Mukherjee, T., Wei, H. L., De, A., and DebRoy, T., 2018, "Heat and Fluid Flow in Additive Manufacturing—Part I: Modeling of Powder Bed Fusion," Computational Materials Science, **150**, pp. 304–313.

[17] Jamshidinia, M., Kong, F., and Kovacevic, R., 2013, "Numerical Modeling of Heat Distribution in the Electron Beam Melting® of Ti-6Al-4V," Journal of Manufacturing Science and Engineering, **135**(6).

[18] Karayagiz, K., Elwany, A., Tapia, G., Franco, B., Johnson, L., Ma, J., Karaman, I., and Arróyave, R., 2019, "Numerical and Experimental Analysis of Heat Distribution in the Laser Powder Bed Fusion of Ti-6Al-4V," IISE Transactions, **51**(2), pp. 136–152.

[19] Mukherjee, T., Wei, H. L., De, A., and DebRoy, T., 2018, "Heat and Fluid Flow in Additive Manufacturing – Part II: Powder Bed Fusion of Stainless Steel, and Titanium, Nickel and Aluminum Base Alloys," Computational Materials Science, **150**, pp. 369–380.

[20] Foroozmehr, A., Badrossamay, M., Foroozmehr, E., and Golabi, S., 2016, "Finite Element Simulation of Selective Laser Melting Process Considering Optical Penetration Depth of Laser in Powder Bed," Materials & Design, **89**, pp. 255–263.

[21] Khairallah, S. A., Anderson, A. T., Rubenchik, A., and King, W. E., 2016, "Laser Powder-Bed Fusion Additive Manufacturing: Physics of Complex Melt Flow and Formation Mechanisms of Pores, Spatter, and Denudation Zones," Acta Materialia, **108**, pp. 36–45.

[22] Mishra, A. K., and Kumar, A., 2019, "Numerical and Experimental Analysis of the Effect of Volumetric Energy Absorption in Powder Layer on Thermal-Fluidic Transport in Selective Laser Melting of Ti6Al4V," Optics & Laser Technology, **111**, pp. 227–239.

[23] Liu, S., Zhu, H., Peng, G., Yin, J., and Zeng, X., 2018, "Microstructure Prediction of Selective Laser Melting AlSi10Mg Using Finite Element Analysis," Materials & Design, **142**, pp. 319–328.

[24] Mahmood, M. A., Popescu, A. C., and Mihailescu, I. N., 2020, "Metal Matrix Composites Synthesized by Laser-Melting Deposition: A Review," Materials, **13**(11), p. 2593.

[25] Read, N., Wang, W., Essa, K., and Attallah, M. M., 2015, "Selective Laser Melting of AlSi10Mg Alloy: Process Optimisation and Mechanical Properties Development," Materials & Design (1980-2015), **65**, pp. 417–424.

[26] Prashanth, K. G., Scudino, S., Klauss, H. J., Surreddi, K. B., Löber, L., Wang, Z., Chaubey, A. K., Kühn, U., and Eckert, J., 2014, "Microstructure and Mechanical Properties of Al–12Si Produced by Selective Laser Melting: Effect of Heat Treatment," Materials Science and Engineering: A, **590**, pp. 153–160.

[27] Aversa, A., Marchese, G., Saboori, A., Bassini, E., Manfredi, D., Biamino, S., Ugues, D., Fino, P., and Lombardi, M., 2019, "New Aluminum Alloys Specifically Designed for Laser Powder Bed Fusion: A Review," Materials, **12**(7), p. 1007.

[28] Xi, L., Gu, D., Guo, S., Wang, R., Ding, K., and Prashanth, K. G., 2020, "Grain Refinement in Laser Manufactured Al-Based Composites with TiB2 Ceramic," Journal of Materials Research and Technology, **9**(3), pp. 2611–2622.

[29] Gu, D., Wang, H., Dai, D., Yuan, P., Meiners, W., and Poprawe, R., 2015, "Rapid Fabrication of Al-Based Bulk-Form Nanocomposites with Novel Reinforcement and Enhanced Performance by Selective Laser Melting," Scripta Materialia, **96**(C), pp. 25–28.

[30] Montero Sistiaga, M. L., Mertens, R., Vrancken, B., Wang, X., van Hooreweder, B., Kruth, J. P., and van Humbeeck, J., 2016, "Changing the Alloy Composition of Al7075 for Better Processability by Selective Laser Melting," Journal of Materials Processing Technology, **238**, pp. 437–445.

[31] Manvatkar, V., De, A., and DebRoy, T., 2014, "Heat Transfer and Material Flow during Laser Assisted Multi-Layer Additive Manufacturing," Journal of Applied Physics, **116**(12), p. 124905.

[32] Yadroitsev, I., Gusarov, A., Yadroitsava, I., and Smurov, I., 2010, "Single Track Formation in Selective Laser Melting of Metal Powders," Journal of Materials Processing Technology, **210**(12), pp. 1624–1631.

[33] Gu, D., and Shen, Y., 2009, "Balling Phenomena in Direct Laser Sintering of Stainless Steel Powder: Metallurgical Mechanisms and Control Methods," Materials & Design, **30**(8), pp. 2903–2910.

[34] Dai, D., and Gu, D., 2016, "Influence of Thermodynamics within Molten Pool on Migration and Distribution State of Reinforcement during Selective Laser Melting of AlN/AlSi10Mg Composites," International Journal of Machine Tools and Manufacture, **100**, pp. 14–24.

[35] Rahman, K. M., Ruhul Amin, M., and Mian, A., 2019, "A Numerical Study of Diffusion of Nanoparticles in a Viscous Medium During Solidification," Journal of Thermal Science and Engineering Applications, **11**(1).

[36] Sahoo, S., and Chou, K., 2016, "Phase-Field Simulation of Microstructure Evolution of Ti–6Al–4V in Electron Beam Additive Manufacturing Process," Additive Manufacturing, **9**, pp. 14–24.

[37] Mohebbi, M. S., and Ploshikhin, V., 2020, "Implementation of Nucleation in Cellular Automaton Simulation of Microstructural Evolution during Additive Manufacturing of Al Alloys," Additive Manufacturing, **36**, p. 101726.

[38] Mishra, S., and DebRoy, T., 2004, "Grain Topology in Ti–6Al–4V Welds—Monte Carlo Simulation and Experiments," Journal of Physics D: Applied Physics, **37**(15), pp. 2191–2196.

[39] Tan, J. H. K., Sing, S. L., and Yeong, W. Y., 2020, "Microstructure Modelling for Metallic Additive Manufacturing: A Review," Virtual and Physical Prototyping, **15**(1), pp. 87–105.

[40] Rappaz, M., and Gandin, Ch.-A., 1993, "Probabilistic Modelling of Microstructure Formation in Solidification Processes," Acta Metallurgica et Materialia, **41**(2), pp. 345–360.

[41] Standard, A., 2012, "E112," Standard test methods for determining average grain size.

[42] Zinovieva, O., Zinoviev, A., and Ploshikhin, V., 2018, "Three-Dimensional Modeling of the Microstructure Evolution during Metal Additive Manufacturing," Computational Materials Science, **141**, pp. 207–220.

[43] Paul, S., Liu, J., Strayer, S. T., Zhao, Y., Sridar, S., Klecka, M. A., Xiong, W., and To, A. C., 2020, "A Discrete Dendrite Dynamics Model for Epitaxial Columnar Grain Growth in Metal Additive Manufacturing with Application to Inconel," Additive Manufacturing, **36**, p. 101611.

[44] Thijs, L., Kempen, K., Kruth, J.-P., and van Humbeeck, J., 2013, "Fine-Structured Aluminium Products with Controllable Texture by Selective Laser Melting of Pre-Alloyed AlSi10Mg Powder," Acta Materialia, **61**(5), pp. 1809–1819.

[45] Yang, M., Wang, L., and Yan, W., 2021, "Phase-Field Modeling of Grain Evolutions in Additive Manufacturing from Nucleation, Growth, to Coarsening," Computational Materials, **7**(1), p. 56.

[46] Couturier, G., Doherty, R., Maurice, C., and Fortunier, R., 2005, "3D Finite Element Simulation of the Inhibition of Normal Grain Growth by Particles," Acta Materialia, **53**(4), pp. 977–989.

[47] Yang, M., Wang, L., and Yan, W., 2021, "Phase-Field Modeling of Grain Evolution in Additive Manufacturing with Addition of Reinforcing Particles," Additive Manufacturing, **47**, p. 102286.

[48] Gu, D., 2015, *Laser Additive Manufacturing of High-Performance Materials*, Springer Berlin Heidelberg, Berlin, Heidelberg.

[49] Martin, J. H., Yahata, B. D., Hundley, J. M., Mayer, J. A., Schaedler, T. A., and Pollock, T. M., 2017, "3D Printing of High-Strength Aluminium Alloys," Nature, **549**(7672), pp. 365–369.

[50] Ravera, F., Santini, E., Loglio, G., Ferrari, M., and Liggieri, L., 2006, "Effect of Nanoparticles on the Interfacial Properties of Liquid/Liquid and Liquid/Air Surface Layers," The Journal of Physical Chemistry B, **110**(39), pp. 19543–19551.

[51] Thomas, B. G., Yuan, Q., Mahmood, S., Liu, R., and Chaudhary, R., 2014, "Transport and Entrapment of Particles in Steel Continuous Casting," Metallurgical and Materials Transactions B, **45**(1), pp. 22–35.

[52] Serraj, Rachid., 1986, *Theory and Applications of Cellular Automata*, World Scientific Publishing Company, Singapore :

[53] Fluent, A., 2011, "ANSYS Fluent User's Guide, Release 14.0," PA: ANSYS Fluent.

[54] Cao, L., and Yuan, X., 2019, "Study on the Numerical Simulation of the SLM Molten Pool Dynamic Behavior of a Nickel-Based Superalloy on the Workpiece Scale," Materials, **12**(14), p. 2272.

[55] Pei, W., Zhengying, W., Zhen, C., Junfeng, L., Shuzhe, Z., and Jun, D., 2017, "Numerical Simulation and Parametric Analysis of Selective Laser Melting Process of AlSi10Mg Powder," Applied Physics A, **123**(8), p. 540.

[56] Mills, K. C., 2002, *Recommended Values of Thermophysical Properties for Selected Commercial Alloys*, Woodhead Publishing.

[57] Munro, R., 2000, "Material Properties of Titanium Diboride," Journal of Research of the National Institute of Standards and Technology, **105**, p. 709.

[58] Mukherjee, T., Manvatkar, V., De, A., and DebRoy, T., 2017, "Dimensionless Numbers in Additive Manufacturing," Journal of Applied Physics, **121**(6), p. 064904.

[59] Lee, Y., Nordin, M., Babu, S., and Farson, D., 2014, "Influence of Fluid Convection on Weld Pool Formation in Laser Cladding," Weld J, **93**, pp. 292s–300s.

[60] Mishra, S., Lienert, T. J., Johnson, M. Q., and DebRoy, T., 2008, "An Experimental and Theoretical Study of Gas Tungsten Arc Welding of Stainless Steel Plates with Different Sulfur Concentrations," Acta Materialia, **56**(9), pp. 2133–2146.

[61] Ramachandran, N., Gupta, J. P., and Jaluria, Y., 1982, "Thermal and Fluid Flow Effects during Solidification in a Rectangular Enclosure," International Journal of Heat and Mass Transfer, **25**(2), pp. 187–194.

[62] Gadgil, A., and Gobin, D., 1984, "Analysis of Two-Dimensional Melting in Rectangular Enclosures in Presence of Convection," Journal of Heat Transfer, **106**(1), pp. 20–26.

[63] Brent, A. D., Voller, V. R., and Reid, K. J., 1988, "Enthalpy-Porosity Technique For Modeling Convection-Diffusion Phase Change: Application To The Melting of A Pure Metal," Numerical Heat Transfer, **13**(3), pp. 297–318.

[64] Pal, D., and Joshi, Y. K., 2001, "Melting in a Side Heated Tall Enclosure by a Uniformly Dissipating Heat Source," International Journal of Heat and Mass Transfer, **44**(2), pp. 375–387.

[65] He, Q., Xia, H., Liu, J., Ao, X., and Lin, S., 2020, "Modeling and Numerical Studies of Selective Laser Melting: Multiphase Flow, Solidification and Heat Transfer," Materials & Design, **196**, p. 109115.

[66] Swaminathan, C. R., and Voller, V. R., 1992, "A General Enthalpy Method for Modeling Solidification Processes," Metallurgical Transactions B, **23**(5), pp. 651–664.

[67] Ounis, H. M., Ahmadi, G., and McLaughlin, J. B., 1991, "Brownian Diffusion of Submicrometer Particles in the Viscous Sublayer."

[68] Hinds, W. C., 1999, *Aerosol Technology : Properties, Behavior, and Measurement of Airborne Particles*, Wiley, New York.

[69] Saffman, P. G., 1965, "The Lift on a Small Sphere in a Slow Shear Flow," Journal of Fluid Mechanics, **22**(2), pp. 385–400.

[70] Li, A., and Ahmadi, G., 1992, "Dispersion and Deposition of Spherical Particles from Point Sources in a Turbulent Channel Flow," Aerosol Science and Technology, **16**(4), pp. 209–226.

[71] Liu, J., and To, A. C., 2017, "Quantitative Texture Prediction of Epitaxial Columnar Grains in Additive Manufacturing Using Selective Laser Melting," Additive Manufacturing, **16**, pp. 58–64.

[72] Rhie, C. M., and Chow, W. L., 1983, "Numerical Study of the Turbulent Flow Past an Airfoil with Trailing Edge Separation," AIAA Journal, **21**(11), pp. 1525–1532.

[73] Chorin, A. J., 1968, "Numerical Solution of the Navier-Stokes Equations," Mathematics of Computation, **22**(104), pp. 745–762.

[74] Bagheri, G. H., Salmanzadeh, M., Golkarfard, V., and Ahmadi, G., 2012, "Simulation of Solid Particles Behavior in a Heated Cavity at High Rayleigh Numbers," Aerosol Science and Technology, **46**(12), pp. 1382–1391.

[75] Shahabad, S. I., Zhang, Z., Keshavarzkermani, A., Ali, U., Mahmoodkhani, Y., Esmaeilizadeh, R., Bonakdar, A., and Toyserkani, E., 2020, "Heat Source Model

Calibration for Thermal Analysis of Laser Powder-Bed Fusion," The International Journal of Advanced Manufacturing Technology, **106**(7–8), pp. 3367–3379.

[76] Gandin, Ch.-A., Charbon, Ch., and Rappaz, M., 1995, "Stochastic Modelling of Solidification Grain Structures.," ISIJ International, **35**(6), pp. 651–657.

[77] Zhang, J., Li, W., Yan, L., and Liou, F., 2018, "A Two-Dimensional Simulation of Grain Structure Growth within the Substrate and the Fusion Zone during Direct Metal Deposition," Comptes Rendus Mécanique, **346**(11), pp. 1072–1086.

[78] Guillemot, G., Gandin, Ch.-A., and Bellet, M., 2007, "Interaction between Single Grain Solidification and Macrosegregation: Application of a Cellular Automaton—Finite Element Model," Journal of Crystal Growth, **303**(1), pp. 58–68.

[79] MATLAB, 2018, *9.7.0.1190202 (R2019b)*, The MathWorks Inc., Natick, Massachusetts.

[80] Tang, M., Pistorius, P. C., Narra, S., and Beuth, J. L., 2016, "Rapid Solidification: Selective Laser Melting of AlSi10Mg," JOM, **68**(3), pp. 960–966.

[81] Takata, N., Kodaira, H., Sekizawa, K., Suzuki, A., and Kobashi, M., 2017, "Change in Microstructure of Selectively Laser Melted AlSi10Mg Alloy with Heat Treatments," Materials Science and Engineering: A, **704**, pp. 218–228.

[82] Rai, A., Markl, M., and Körner, C., 2016, "A Coupled Cellular Automaton–Lattice Boltzmann Model for Grain Structure Simulation during Additive Manufacturing," Computational Materials Science, **124**, pp. 37–48.

[83] Baumard, A., Ayrault, D., Fandeur, O., Bordreuil, C., and Deschaux-Beaume, F., 2021, "Numerical Prediction of Grain Structure Formation during Laser Powder Bed Fusion of 316 L Stainless Steel," Materials & Design, **199**, p. 109434.

[84] ASTM, 2002, "Standard E 1382, 1997: Standard Test Methods for Determining Average Grain Size Using Semiautomatic and Automatic Image Analysis."

[85] Brechet, Y., Embury, J. D., Tao, S., and Luo, L., 1991, "Damage Initiation in Metal Matrix Composites," Acta metallurgica et materialia, **39**(8), pp. 1781–1786.

[86] Köhnen, P., Létang, M., Voshage, M., Schleifenbaum, J. H., and Haase, C., 2019, "Understanding the Process-Microstructure Correlations for Tailoring the Mechanical Properties of L-PBF Produced Austenitic Advanced High Strength Steel," Additive Manufacturing, **30**, p. 100914.

[87] Li, L., and Liou, F., 2021, “Numerical Investigation of Thermo-Mechanical Field during Selective Laser Melting Process with Experimental Validation,” Metals (Basel), **11**(7), p. 1003.